

UILU-ENG 89-3601

Report No. 147

BIAXIAL-TENSION FATIGUE OF INCONEL 718

by

Daniel L. Morrow

Materials and Design Division  
Department of Mechanical and Industrial Engineering

A Report of the

MATERIALS ENGINEERING - MECHANICAL BEHAVIOR

College of Engineering, University of Illinois at Urbana-Champaign

February 1989

## BIAXIAL-TENSION FATIGUE OF INCONEL 718

Daniel Lowell Morrow, Ph.D.  
Department of Mechanical and Industrial Engineering  
University of Illinois at Urbana-Champaign, 1988

### ABSTRACT

Many components used in the power generation and aircraft industries are subjected to severe multiaxial stresses. Some components, such as turbine discs, operate in stress quadrants I and III where their principal stresses are of the same sign. Little experimental work has been done to evaluate material fatigue characteristics for these loadings. This research characterized the multiaxial fatigue behavior of Inconel 718 in stress quadrants I and III.

Predictions of cracking behavior and fatigue life were based on multiaxial fatigue parameters generated from tension-torsion data and compared to experimental results. Observations of crack formation from replicas and post-failure sectioning of the specimens helped identify the appropriate damage parameters for this material.

All of the tests resulted in failure cracks that initiated and grew in shear. Roughly 90 percent of the fatigue life was spent initiating and growing these shear cracks to a surface length of 1.0 mm. Transition from shear to tensile crack growth occurred late in life if at all.

Fatigue life predictive capabilities of the five multiaxial fatigue theories considered improved as terms were added that affected shear crack initiation and growth. The poorest correlation for the biaxial-tension and biaxial mean stress tests came from the maximum principal strain theory, where the average life prediction was nonconservative by a factor of 26 and test results fell within a scatterband of a factor of  $\pm 4$  in life. The best

correlation resulted from the Fatemi and Socie theory, where over 90 percent of the data from all stress quadrants correlated within a scatterband of a factor of  $\pm 2.5$  in life.

Cracking behavior for Inconel 718 was dominated by shear crack growth for tension, torsion, and biaxial-tension loadings. The Fatemi and Socie theory demonstrated a sensitivity to shear crack initiation and growth and best described shear nucleation and shear crack growth for Inconel 718.

## ACKNOWLEDGMENTS

This study was conducted in the Materials Engineering Research Laboratory of the University of Illinois at Urbana-Champaign and was supported by Allison Gas Turbine Co., Indianapolis, Indiana, and by NASA Grant NAG3-465.

Professor D. F. Socie, mentor and thesis advisor, is gratefully acknowledged for his advice, encouragement, and his many generous contributions to my personal and professional development throughout my academic career. Special thanks are extended to Dr. P. Kurath for his assistance with the experiments, our many stimulating discussions, and his unflagging and friendly support. Professors F. A. Leckie, H. Sehitoglu, J. Stubbins, and J. Morrow are gratefully acknowledged for their patience and sage guidance.

The special efforts of many skilled craftsmen were instrumental in this research and are greatly appreciated, in particular those of Kent Elam and the T&AM machinists for their expert instrument, specimen, and widget manufacturing skills, and Gary Ashby for his expertise in preparing the cracking pictures for publication.

A special thanks is offered to Kate, Carl, Annie, Joe and Sally for their love and encouragement.

## TABLE OF CONTENTS

	Page
LIST OF FIGURES.....	ix
LIST OF SYMBOLS.....	xii
1.0 INTRODUCTION.....	1
1.1 <u>Background and Review of Previous Work on Inconel 718</u> .....	3
1.2 <u>Review of Previous Biaxial-Tension Research</u> .....	6
1.3 <u>Summary of Previous Research</u> .....	11
1.4 <u>Purpose and Scope</u> .....	12
2.0 EXPERIMENTAL PROGRAM.....	14
2.1 <u>Material</u> .....	14
2.2 <u>Testing Facility</u> .....	14
2.3 <u>Controls</u> .....	15
2.4 <u>Specimen Selection</u> .....	15
2.5 <u>Test Program</u> .....	17
3.0 ANALYSIS.....	19
3.1 <u>St. Venant's Maximum Principal Strain Theory</u> .....	19
3.2 <u>Tresca's Maximum Shear Strain Theory</u> .....	20
3.3 <u>Brown and Miller's Normal Strain Modified Maximum Shear Strain Theory</u> .....	21
3.4 <u>Socie's Mean Stress Modified Maximum Shear Strain Theory</u> ...	22
3.5 <u>Fatemi and Socie's Maximum Normal Stress Modified Maximum Shear Strain Theory</u> .....	22
4.0 STRESS-STRAIN ANALYSIS.....	24
4.1 <u>Cyclic Stresses and Strains</u> .....	24
4.2 <u>Residual Stresses Due to Yielding on the First Reversal</u> ....	25
4.3 <u>Stress-Strain for Biaxial Mean Stress Tests</u> .....	27
5.0 RESULTS AND OBSERVATIONS.....	29
5.1 <u>Cracking Observations</u> .....	29
5.1.1 <u>Equal-Biaxial Tests, Completely Reversed</u> .....	29
5.1.2 <u>Biaxial-Tension Tests, Released Tension</u> .....	33
5.1.3 <u>Biaxial Mean Stress Tests</u> .....	36
5.1.4 <u>Summary of Cracking Observations</u> .....	38
5.2 <u>Life Predictions</u> .....	38
5.2.1 <u>Summary of Life Predictions</u> .....	40

6.0 DISCUSSION.....	41
6.1 <u>Evaluation of Fatigue Theory</u> .....	42
6.2 <u>Critical Comparisons of Fatigue Behavior in All</u> <u>Stress Quadrants</u> .....	44
6.3 <u>Research Limitations</u> .....	46
6.4 <u>Summary of Discussion</u> .....	47
7.0 CONCLUSIONS.....	48
TABLES.....	49
FIGURES.....	52
REFERENCES.....	102
APPENDIX A OVERVIEW OF TEST SYSTEM.....	105
APPENDIX B TEST CONTROL CONDITIONS.....	110
APPENDIX C SURFACE CRACK MEASUREMENTS.....	113
VITA.....	119

## LIST OF FIGURES

		Page
Figure 1.	a) Thin-walled tube; b-e) possible loadings in two-dimensional stress space.....	52
Figure 2.	a) Surface elements in uniaxial tension, shear, and biaxial tension; b) Mohr's stress circles; c) resulting maximum principal shear planes.....	53
Figure 3.	Biaxial strain paths.....	54
Figure 4.	Etched microstructure.....	55
Figure 5.	Schematic of test system controls.....	56
Figure 6.	Single reduced specimen dimensions.....	57
Figure 7.	Stress distribution from Finite Element Method for single reduced specimen.....	58
Figure 8.	Double reduced specimen dimensions.....	59
Figure 9.	Stress distribution from Finite Element Method for double reduced specimen.....	60
Figure 10.	Plastic zone definition for an elastic-plastic tube.....	61
Figure 11.	$\sigma_{\theta}$ residual stresses from single overload.....	62
Figure 12.	$\sigma_z$ residual stresses from single overload.....	63
Figure 13.	Test details and Mohr's circles for INDM01 on outer surface..	64
Figure 14.	Cracking details for INDM01.....	65
Figure 15.	Test details and Mohr's circles for INDM05 on outer surface..	66
Figure 16.	Cracking details for INDM05.....	67
Figure 17.	Test details and Mohr's circles for INDM03 on outer surface..	68
Figure 18.	Cracking details for INDM03, Failure crack.....	69
Figure 19.	Cracking details for INDM03, Non-failure crack.....	70
Figure 20.	Cracking details for INDM03, Non-failure crack etched.....	71
Figure 21.	Test details and Mohr's circles for INDM07 on inner surface..	72
Figure 22.	Cracking details for INDM07.....	73

Figure 23.	Diametral stress-strain loop, setup cycle for INDM07.....	74
Figure 24.	Test details and Mohr's circles for INDM08 on inner surface..	75
Figure 25.	Cracking details for INDM08.....	76
Figure 26.	Test details and Mohr's circles for IN01 on inner surface....	77
Figure 27.	Test details and Mohr's circles for IN02 on inner surface....	78
Figure 28.	Failure cracks for IN01 and IN02.....	79
Figure 29.	Test details and Mohr's circles for INDM06 on inner surface..	80
Figure 30.	Cracking details for INDM06.....	81
Figure 31.	Mohr's circles for biaxial mean stress tests on outer surface	82
Figure 32.	Test details and Mohr's circles for INA4 on outer surface....	83
Figure 33.	Test details and Mohr's circles for INA17 on outer surface...	84
Figure 34.	Cracking details for INA4.....	85
Figure 35.	Cracking details for INA17.....	86
Figure 36.	Test details and Mohr's circles for INA5 on outer surface....	87
Figure 37.	Test details and Mohr's circles for INA13 on outer surface...	88
Figure 38.	Cracking details for INA5.....	89
Figure 39.	Cracking details for INA13.....	90
Figure 40.	Test details and Mohr's circles for INA12 on outer surface...	91
Figure 41.	Test details and Mohr's circles for INA23 on outer surface...	92
Figure 42.	Cracking details for INA12.....	93
Figure 43.	Cracking details for INA23.....	94
Figure 44.	Life predictions for biaxial-tension data, maximum principal strain theory.....	95
Figure 45.	Life predictions for biaxial-tension data, maximum shear strain (Tresca's) theory.....	96
Figure 46.	Life predictions for biaxial-tension data, Brown and Miller theory.....	97



Figure 47.	Life predictions for biaxial-tension data, Socie's mean stress modified Brown and Miller theory.....	98
Figure 48.	Life predictions for biaxial-tension data, Fatemi and Socie theory.....	99
Figure 49.	Fatigue damage maps with cracking behavior for torsion, tension, and biaxial-tension loadings.....	100
Figure 50.	Correlation of Inconel 718 tests from all stress quadrants using Fatemi and Socie's theory.....	101
Figure A1.	Schematic drawing of the load frame.....	107
Figure A2.	Sectioned view of the pressure vessel and its contents.....	108
Figure A3.	Schematic drawing of sectioned mandril and specimen.....	109
Figure B1.	Schematic of control system for strain controlled tests.....	112

## LIST OF SYMBOLS

b	Fatigue strength exponent
c	Fatigue ductility exponent
E	Young's modulus
$F_z$	Axial load
G	Shear modulus
$N_{1.0}$	Cycles to initiate a 1 mm crack
$N_f$	Cycles to failure
$P_c$	Critical pressure, onset of plastic deformation
$P_i, P_o$	Inside pressure, outside pressure
$R_\epsilon$	Strain ratio, $\epsilon_{i\min}/\epsilon_{i\max}$
$R_\sigma$	Stress ratio, $\sigma_{i\min}/\sigma_{i\max}$
$r_i, r_o$	Inside, outside radius of tube
t	Specimen thickness
$\hat{\gamma}$	Maximum shear strain amplitude
$\gamma_f$	Shear fatigue ductility coefficient
$\hat{\gamma}_p$	Maximum plastic shear strain amplitude
$\epsilon_1, \epsilon_2, \epsilon_3$	Principal strains
$\epsilon_f$	Fatigue ductility coefficient
$\hat{\epsilon}_n$	Strain amplitude normal to maximum shear plane
$\hat{\epsilon}_{np}$	Plastic strain amplitude normal to maximum shear plane
$\epsilon_z, \epsilon_\theta, \epsilon_r$	Axial, tangential, radial strain
$\nu$	Poisson's ratio
$\nu_{\text{eff}}$	Effective Poisson's ratio
$\sigma_1, \sigma_2, \sigma_3$	Principal stresses
$\sigma_f$	Fatigue strength coefficient

$\sigma_n^{\max}$	Maximum normal stress on maximum shear plane
$\hat{\sigma}_{no}$	Mean normal stress on maximum shear plane
$\sigma_y(0.2\%)$	0.2 Percent offset yield stress
$\sigma_z, \sigma_\theta, \sigma_r$	Axial, tangential, radial stress
$\tau_f$	Shear fatigue strength coefficient
$\tau_r, \tau_\theta$	Maximum principal shear planes
$\phi_\epsilon$	Biaxial strain ratio, $\epsilon_2/\epsilon_1$
$\phi_\sigma$	Biaxial stress ratio, $\sigma_2/\sigma_1$

## 1.0 INTRODUCTION

Many components used in the power generation and aircraft industries are subjected to severe multiaxial stresses. The demand for higher engine efficiencies has resulted in increased operating temperatures. In critical applications--for example, in the design of turbine discs--these higher temperatures necessitate the use of high strength, creep-resistant superalloys that exhibit nominally elastic behavior even at short lives. Major loading cycles, such as ground-air-ground cycles for aircraft engines and start-stop cycles for standby power generators, result in fatigue lives for these materials of approximately  $10^3$  to  $10^5$  cycles.

Some components, such as turbine discs, operate in stress quadrants I and III where their principal stresses are of the same sign. The fatigue analysis of these components requires the implementation of a multiaxial fatigue theory validated in stress quadrants I and III for the material in question.

Thin-walled tubes are often used for multiaxial fatigue research because their principal stresses and strains are easily controlled. Figure 1a shows a schematic of a thin-walled tube and a representative surface element. Cylindrical coordinates are used where the z-axis is aligned with the specimen axis. Loading conditions may consist of axial tension or compression, torsion, internal pressure, and external pressure. Figures 1b through 1e show possible combinations of the above loadings on a two-dimensional stress space. In Figure 1b, the ordinate represents axial loadings, while the line at 45 degrees through quadrants II and IV represents pure shear loadings. The shaded area between these two quadrants corresponds to all possible combinations of axial and torsional loadings. If the material is assumed to be isotropic, then the unshaded areas in quadrants II and IV can be defined by symmetry with the

shaded areas. Only one-fourth of the two-dimensional stress space can be investigated directly with combinations of axial and torsional loading. Quadrants II and IV are the easiest to investigate and are therefore the focus of most multiaxial fatigue research. Internal pressure and axial tension loadings are required to enter stress quadrant I. In fact, the entire right-half plane can be investigated with internal pressure and axial tension or compression (Fig. 1c). Using external pressure and axial compression, the entire left-half plane, including quadrant III, can be investigated (Fig. 1d). Loading into quadrants I and III is required for completely reversed fatigue tests with both principal stresses of the same sign. External pressure, internal pressure, and axial tension or compression meet these requirements, as shown in Figure 1e.

Figure 2a shows surface elements from a thin-walled tube under uniaxial, shear, and equal-biaxial stresses. The Mohr's circles of stress and strain (Fig. 2b) illustrate that, while all three loading cases may have the same maximum shear stress, the planes of maximum principal shear are quite different for each case (Fig. 2c). For uniaxial loading, the  $\tau_r$ -planes and the  $\tau_\theta$ -planes are planes of maximum principal shear. The  $\tau_\theta$ -planes are oriented at 45 degrees from the surface and result in intrusion and extrusion of persistent slip bands with no grain boundary resistance to slip at the free surface. The  $\tau_r$ -planes are at 45 degrees to the z-axis but are contained within the specimen. Any slip that occurs in the  $\tau_r$ -planes must continually encounter grain boundary resistance. Therefore, the  $\tau_r$ -planes have a greater resistance to dislocation movement than do the  $\tau_\theta$ -planes.

Pure shear loading results in  $\tau_r$ -planes of maximum principal shear, while biaxial-tension loading results in  $\tau_\theta$ -planes of maximum principal shear.

These differences in planes of maximum principal shear introduce uncertainty into the prediction of fatigue life using axial and torsional fatigue data for biaxial-tension loading conditions.

Ideally, the important parameters for the prediction of damage and fatigue life would be generated from a less complex state of stress, such as torsion or uniaxial tension.

### 1.1 Background and Review of Previous Work on Inconel 718

In the early 1980s, Socie, et al. [1-7] began research to characterize the multiaxial fatigue behavior of Inconel 718. Thin-walled tube specimens were cut from a forged ring of Inconel. Axial tests of standard fatigue specimens taken from the axial and tangential directions of the forged ring indicated that anisotropic effects were negligible. Fifteen different strain paths were investigated with fatigue lives ranging from 500 to  $10^6$  cycles. Detailed crack monitoring was performed using surface replicating techniques.

Waill [2] performed tests using strain paths A through F (Fig. 3). These paths comprised strain controlled axial, torsional, and combined loadings for the strain ratios of  $R_\epsilon = -1$  (paths A, B, and C) and  $R_\epsilon = 0$  (paths D, E, and F). She noticed the formation of slip bands on the surface of the specimen, some of which darkened and widened, and that cracks appeared in these darkened regions. Waill concluded that cracks initiated on planes of maximum shear for all three loading cases tested. Crack growth continued on these planes for torsional and axial-torsional loading cases, changing in later life to planes of maximum principal strain for the axial loading cases. Waill observed the highest crack densities for torsional loading, the lowest densities for axial, and densities between these for the combined axial-torsional loading.

Beer [3] sectioned the specimens tested by Waill and found that the crack-  
ing mode and crack shape were nearly identical for tension and torsion for  
crack lengths of less than 1 mm.

The fact that all three loading cases for Inconel 718 (axial, torsional,  
and combined axial-torsional) initiated and grew cracks in shear up to 1 mm  
suggested to Socie, et al. [1] that a shear strain based fatigue theory was  
required. Mean stresses affected fatigue life and determined which shear  
plane would first initiate cracks; therefore a mean stress term was also  
necessary. Socie combined a modified Kandil, Brown, and Miller [8] shear  
strain parameter with the Coffin-Manson equation as follows:

$$\hat{\gamma}_p + \hat{\epsilon}_{np} + \hat{\sigma}_{no}/E = 1.75\epsilon_f(2N_{1.0})^c \quad (1)$$

where  $\hat{\gamma}_p$  is the maximum plastic shear strain amplitude,  $\hat{\epsilon}_{np}$  is the cyclic  
plastic strain amplitude normal to the  $\hat{\gamma}$  plane,  $\hat{\sigma}_{no}$  is the mean stress across  
the  $\hat{\gamma}_p$  plane, E is Young's modulus,  $\epsilon_f$  and c are the fatigue ductility coef-  
ficient and exponent, and  $N_{1.0}$  is the number of cycles required to form a 1 mm  
surface crack.

Socie and Shield [4] conducted additional tension-torsion tests (paths G  
through J in Fig. 3) to verify and quantify the effects of mean stress. They  
found that all failure cracks followed the maximum shear plane with the  
largest mean normal stress and that mode of failure was not affected by the  
presence of mean stresses. Mean stress effects were seen even when large  
plastic strains were present. Socie and Shield concluded that any approach  
that ignores mean stresses, such as the equivalent strain approach, would be  
useful only for completely reversed, constant amplitude data or where mean

stresses are unimportant. They also noted that most of the fatigue life was dominated by crack growth and that a crack growth approach might better characterize this material. Also, models that included a hydrostatic mean stress term would not be expected to correlate the Inconel 718 data since there is no distinction between stresses normal to or parallel to the plane of cracking. In fact, any approach that averages the stresses and therefore does not distinguish between stresses normal to and parallel to the plane of cracking will fail to correlate the Inconel 718 data. Socie and Shield determined the coefficients for the normal plastic strain and normal mean stress terms in Equation 1 and combined these with a torsional equivalent to the Coffin-Manson equation as follows:

$$\hat{\gamma}_p + 1.5\hat{\epsilon}_{11p} + 1.5\hat{\sigma}_{no}/E = \gamma'_f(2N_{1.0})^c \quad (2)$$

The left side of this equation is the same as in Equation 1, except that the shear fatigue ductility coefficient here is  $\gamma'_f$  and the exponent is  $c$ . This model was later changed to correlate total strain torsional data as follows [7]:

$$\hat{\gamma} + \hat{\epsilon}_n + \hat{\sigma}_{no}/E = \gamma'_f(2N_{1.0})^c + \frac{\tau'_f}{G}(2N_{1.0})^b \quad (3)$$

where  $\hat{\gamma}$  is the maximum shear strain amplitude,  $\hat{\epsilon}_n$  is the normal strain amplitude on the plane of maximum shear strain amplitude, and  $\hat{\sigma}_{no}$  is the mean normal stress on the plane of maximum shear strain amplitude. The right side of this equation is the total shear strain-life relation,  $\tau'_f$  is the shear



fatigue strength coefficient,  $b$  is the shear fatigue strength exponent,  $G$  is the shear modulus, and  $N_{1.0}$  is the number of cycles to form a 1 mm crack.

Koch [5] conducted nonproportional and out-of-phase tension-torsion tests (Fig. 3, paths K through O) to further identify the nonshear terms in Equation 3. Koch concluded, as had previous researchers, that cracks initiated and grew on planes of maximum shear strain amplitude and that fatigue lives were dominated by crack growth. He observed that nonshear terms identified the preferred direction of crack propagation for strain paths where there were differences between these terms for the two  $\hat{\gamma}$  planes. Koch correlated, to within a factor of two, all the data generated to date using constant amplitude, fully reversed, torsional data to generate material constants for Equation 3. He also noted that the proposed three term parameter (Eq. 3) was consistently nonconservative for out-of-phase strain paths with large plastic strains.

All previous research on this material has been confined to stress quadrants II and IV in biaxial stress space. In these stress quadrants and for lives ranging from 500 to  $10^6$  cycles, cracks initiate and propagate on planes of maximum shear. A shear-based parameter should best correlate the data. A brief review of the differences between tension-torsion and biaxial-tension observed by researchers for other materials follows.

## 1.2 Review of Previous Biaxial-Tension Research

Biaxial-tension fatigue has been approached via three distinct methodologies: high cycle fatigue, using stress-based fatigue theories; low cycle fatigue, using strain-based fatigue theories; and crack growth. These approaches represent different life regimes and, possibly, different failure

mechanisms. The somewhat arbitrary definitions of crack initiation proposed by various researchers may cause the initiation and small crack propagation approach of low cycle fatigue to overlap the long crack propagation approach. Thorough reviews of specimen designs, loading apparatus, and damage evaluation techniques are available in the literature [9-14]. A few representative works will be discussed here.

Most early researchers involved in high cycle fatigue found stress-based fatigue criteria to be most appropriate to multiaxial fatigue analysis, since cyclic plastic strains are orders of magnitude smaller than elastic strains at long life. These stress-based criteria are extensions of static yield theories such as the maximum normal stress, maximum shear stress, and so on, and are primarily limited to high cycle fatigue analysis [11].

The work of Blass and Findley [15] in biaxial-tension fatigue on an AISI 4340 thick-walled steel tube ( $t = 5.3$  mm) shows essentially no difference between fatigue life for equal-biaxial loading ( $\phi_\sigma = 1$ ) and near uniaxial loading ( $\phi_\sigma = 0$ ) for a life slightly greater than  $10^5$  cycles. They presented data as greatest principal shear stress versus log life.

Bundy and Marin [16], studying the biaxial fatigue strength of 14S-T4 aluminum thin-walled tubes ( $t = 1.3$  mm) with lives of  $10^4$  to  $10^7$  cycles, also indicated that fatigue characteristics are similar at long life for equal-biaxial and uniaxial loading cases. These data were presented as log maximum principal stress versus log cycles to failure and revealed the same slope and intercept for both the uniaxial and equal-biaxial stress-life curves.

Researchers in low cycle fatigue have used strain-based parameters to present their data. Many low cycle fatigue criteria are extensions of strain-based yield theories such as maximum normal strain, maximum shear strain, and

so on. There are additional complexities in this analysis--for example, the determination, either analytically or experimentally, of the path dependent, cyclic plastic deformation. Cyclic deformation must be understood in order to formulate the correct stress-strain response, which can then be evaluated by a given failure criterion.

Pascoe and de Villiers [17] tested mild steel and QT35 steel, using cruciform specimens with a gage section thickness of 1 mm. Three strain ratios were tested and resulted in shear loading ( $\phi_\epsilon = -1$ ), near uniaxial loading ( $\phi_\epsilon = 0$ ), and equal-biaxial loading ( $\phi_\epsilon = 1$ ). Their choice of strain levels resulted in fatigue lives of  $10^2$  to  $10^4$  cycles. These tests were performed in load control with cyclic limits determined early in the life by strain gages located in the gage section. Data were presented as log maximum principal strain range versus log life. Equal-biaxial loading reduced the allowable strain range by 50 percent at  $10^3$  cycles, compared to the uniaxial loading case. The greatest reduction occurred at the largest strain excursion.

Havard, et al. [18,19,20] tested normalized 1018 steel thin-walled tubes ( $t = 1.1$  mm and  $t = 0.5$  mm). Six biaxial stress ratios ( $\sigma_z/\sigma_\theta$ ), ranging from +3.89 to -3.63, were achieved by varying specimen geometry and nominal loading. Gage section extensometry was used to monitor diametral and axial strain. In this work, two specimen geometries were required to achieve the range of stress ratios tested. Experimental fatigue lives ranged from  $2 \times 10^3$  to  $10^5$  cycles, and data were presented as log maximum principal strain range versus log life. A comparison of the uniaxial with equal-biaxial data in the form of principal total strain range at  $10^3$  cycles indicated that the biaxial loading case reduced the allowable strain range 70 percent from that of the uniaxial case. Originally, a modified maximum shear stress criterion was

proposed to evaluate the data [18,19] that correlated the fatigue lives within a factor of 5. The damage model was later changed to an octahedral, shear strain criterion modified by the hydrostatic stress [20].

Andrews and Ellison [21,22] tested RR58 aluminum alloy thin-walled tubes with a gage section thickness of 1.0 mm. Improved gage section extensometry, specimen design, and control systems allowed surface strain ratio control over the entire range of biaxiality. Fatigue data for lives of  $10^2$  to  $6 \times 10^3$  cycles were presented as log maximum principal strain amplitude versus log life. In this research, the biaxial strain ratio of  $\phi_\epsilon = +1$  was associated with the most damage. Here, maximum principal strain amplitude for a life of  $10^3$  cycles was 40 percent less than in the uniaxial loading case. Andrews and Ellison proposed a von Mises equivalent strain function as the failure criterion, which was then modified by allowing an effective Poisson's ratio,  $\nu_{\text{eff}}$ , to vary between elastic and fully plastic values. The value of  $\nu_{\text{eff}}$  was dependent on strain range.

Lohr and Ellison [23,24] tested 1Cr-Mo-V steel thin-walled tubes with a gage section thickness of 1.0 mm. Significant improvements on Andrews' [21] test facility resulted in increased range and accuracy of strain measurement and control capabilities. In Lohr and Ellison's research, specimen fatigue lives ranged from 500 to  $10^4$  cycles, and data were presented as log maximum principal strain amplitude versus log life. The biaxial strain ratio of  $\phi_\epsilon = +1$  was again shown to be the most damaging; the principal strain amplitude for a life of  $10^3$  cycles was 44 percent less than the uniaxial strain amplitude for the same life. A simplified theory of multiaxial low cycle fatigue failure was proposed that was similar to Brown and Miller's [13] maximum shear strain critical plane theory with an important exception: maximum shear and

normal strains on planes into the surface were always assumed to dictate crack growth through the specimen thickness and thereby to control the fatigue life. For biaxial-tension loading, the two theories are identical, although differences exist concerning principal stress or strain quadrants II and IV.

Lefebvre, et al. [25] tested thin-walled tubes made of A-516 low alloy steel with a gage length thickness of 0.75 mm and 0.5 mm for negative and positive strain ratios, respectively. Seven biaxial strain ratios ( $\epsilon_\theta/\epsilon_z$ ), from -1.25 to +1.0, were investigated under fully reversed strain control ( $R_\epsilon = -1$ ). Data for fatigue lives ranging from 300 to  $10^5$  cycles were presented as log stress or strain amplitude versus log life. Again, the  $\phi_\epsilon = +1$  biaxial strain ratio was the most damaging; total principal strain amplitude for a life of  $10^3$  cycles was 77 percent lower than the axial case.

Investigations of fatigue crack propagation under biaxial loading are commonly performed on cruciform specimens under stress control. This configuration allows the observation of the crack on both specimen surfaces. Stresses and strains near the crack tip are readily calculated using the finite element method. Fracture mechanics concepts can be used to quantify damage and estimate fatigue lives for components.

Charvat and Garrett [26] tested mild steel cruciform specimens with a center section thickness of 6 mm and a 14 mm center starter notch. They investigated three biaxial stress ratios,  $\phi_\sigma = +1, 0,$  and  $-1$  at load ratio  $R_\sigma = 0$ , and found that  $\phi_\sigma = -1$  (compressive transverse stresses, or stresses parallel to the crack) accelerated crack growth, whereas  $\phi_\sigma = +1$  (equal-biaxial-tension) slowed crack growth with respect to the uniaxial crack growth rate. These conclusions were strengthened by changeover tests in which the stress ratio was changed during the tests and the subsequent crack growth rate

observed. Charvat and Garrett designed a test system that eliminated both bending induced by cross-axis loading and anisotropy due to the presence of the crack.

Hoshide, et al. [27] tested structural low carbon steel cruciform specimens with a center section thickness of 2 mm and a 1 mm center starter notch. Three biaxial stress ratios,  $\phi_\sigma = +1, 0,$  and  $-1,$  were tested at load ratios of  $R_\sigma = 0$  and  $-1.$  Maximum stresses were the same for all tests and resulted in the  $R_\sigma = -1$  tests having shorter lives than the  $R_\sigma = 0$  tests. The  $R_\sigma = -1$  tests revealed the same effect of biaxiality on crack growth rate as observed by Charvat and Garrett, namely,  $\phi_\sigma = -1$  accelerated crack growth while  $\phi_\sigma = 1$  retarded crack growth relative to the uniaxial case.

Brown and Miller [28] tested AISI 316 stainless steel cruciform specimens with a center section thickness of 4 mm and a 4 mm center starter notch. The biaxial stress ratios investigated were  $\phi_\sigma = +1, 0,$  and  $-1.$  Except for threshold tests, all tests were conducted at a load ratio of  $R_\sigma = -1$  to avoid ratcheting. Results over a wide range of loads agreed with earlier findings that the shear loading case,  $\phi_\sigma = -1,$  increased crack growth rates while the  $\phi_\sigma = +1$  loading slowed growth rates relative to the uniaxial case.

### 1.3 Summary of Previous Research

Much multiaxial fatigue research has been conducted on Inconel 718 in stress quadrants II and IV. This research indicates that, for lives of 500 to  $10^6$  cycles, cracks initiate and initially grow on planes of maximum shear strain amplitude. A three parameter model (Eq. 3) proposed by Socie can predict cracking direction and fatigue life for cracks of up to 1 mm for all paths tested in quadrants II and IV.

The review of multiaxial fatigue research performed on other materials in stress quadrants I and III reveals no consistency in fatigue behavior between quadrants II and IV and quadrants I and III.

#### 1.4 Purpose and Scope

Fatigue tests performed in quadrants I and III are complex and expensive, so little experimental work has been done to evaluate material fatigue characteristics for these loadings. The purpose of this research was to characterize the multiaxial fatigue behavior of Inconel 718 in stress quadrants I and III. Multiaxial fatigue parameters derived from other states of stress might then be evaluated for quadrants I and III stress states.

Fatigue damage is assumed to be observable from the surface in the form of microcrack formation and growth. Direct observation of surface damage and microcracking, using surface replicating techniques in combination with post-failure sectioning to determine through thickness crack direction, assists in evaluating various fatigue theories. Five fatigue theories are evaluated on their ability to predict both life and cracking directions. Theories that can predict life but not cracking direction have not properly identified the active damage mechanisms, and confidence in the predictive capabilities of such theories when moving from one stress state to another would be low. Additional research has been conducted to investigate the effects of mean stresses imposed on the material in directions other than the principal loading direction. The effects of biaxial mean stresses on cracking behavior and fatigue life for this material can be used to determine the ability of various multiaxial fatigue models to account for biaxial mean stresses. Mean stresses not aligned with the cyclic loading may better represent multiaxial

mean stresses that occur from large, deformation forming operations such as swaging or stamping. Mean stresses from forming operations may not be in the same direction as the principal loading of the component. Multiaxial fatigue models must be able to account for mean stresses that occur in any direction.

The ultimate goal of this and any other fatigue research is to identify the damage parameters required to accurately predict cracking behavior and fatigue life.



## 2.0 EXPERIMENTAL PROGRAM

### 2.1 Material

Inconel 718, a precipitation-hardened, nickel-based superalloy was used for this investigation. It is a complex alloy with a  $\text{Ni}_3\text{CrFe}$  fcc matrix strengthened by fcc  $\text{Ni}_3(\text{Al},\text{Ti})$   $\gamma'$  and by orthorhombic  $\text{Ni}_3\text{Nb}$   $\gamma''$  precipitates. The chemical composition in weight percent and the heat treatment are given in Table 1.

Thin-walled tube specimens were machined from longitudinal sections taken from a forged ring manufactured to Aerospace Material Specification 5663. The specimens were rough machined and then stress relieved at  $600^\circ\text{C}$  for 12 hours to prevent distortion during final machining. The microstructural details of grain size and orientation were determined by sectioning and etching a specimen in an inverted glycergia etchant. Grain diameters ranged from 0.01 mm to 0.2 mm and appeared to have no preferred orientation, as seen in Figure 4.

### 2.2 Testing Facility

A new multiaxial testing system was developed jointly by MTS Systems Corporation and the University of Illinois at Urbana-Champaign. This system can load a tube specimen in any stress or strain quadrant through the application of tension or compression, torsion, and internal and external pressure.

The system is rated as follows:

Tension load	=	445 KN (100 kip)
Compression load	=	1112 KN (250 kip)
Internal pressure	=	138 MPa (20 ksi)
External pressure	=	138 MPa (20 ksi)
Torsion	=	5650 KN-mm (50 in-kip)

Dow 550 silicone oil is used for internal and external pressure application.

An MTS model 632.858-11 extensometer, modified to measure axial, torsional, and diametral displacements at pressures to 138 MPa, allowed direct gage section strain control tests. It is linear in all three degrees of freedom to within  $\pm 1/2$  percent over the full range. Further details on the test system can be found in Appendix A.

### 2.3 Controls

A schematic of the test cell and control system is shown in Figure 5. The axial and tangential parameters are controlled on two levels, an inner loop and an outer loop. The inner control loop consists of several MTS 448 controllers in closed loop control of the desired parameter, while the outer control loop is maintained by a dedicated, single board control computer that generates command levels for the inner loop, samples system response, modifies the command levels to ensure that the system reaches the required end levels, and stores data during the test for later analysis. Appendix B provides a detailed description of control conditions for each test.

### 2.4 Specimen Selection

To preserve the polycrystalline behavior of this material, the wall thickness of the tube was 10 or more grain diameters ( $\approx 1$  mm). Loading capabilities of the internal-external pressure system, combined with the required 1 mm wall thickness, prescribed a specimen diameter of approximately 25 mm to achieve desired stress levels. Failure cracks 1 to 2 mm in length resulted from the choice of this geometry and corresponded to the growth of a crack through the wall thickness. The low fracture toughness of this high strength material and

the high stress levels caused critical crack sizes to be slightly larger than the failure crack sizes of the tubular specimen.

Two specimen geometries were used in this research. The specimen designed for use in the biaxial-mean stress tests was a thin-walled tube with a 25 mm bore and a gage section outside diameter of 29.5 mm (Fig. 6). The finite element method was used to study stress-strain responses of the tube specimens and to help identify critical stress-strain locations. Modeling of the  $\phi_\sigma = 0.93$  biaxial loading condition was accomplished using elastic, eight-noded, axisymmetric-isoparametric elements arranged as shown in Figure 7. Symmetry of loading and specimen geometry allowed only half the specimen to be modeled. In this work, hoop stresses due to pressure loading were nearly constant in the gage section. The axial stress resulting from either axial loading or internal pressure was constant within the gage section and exhibited a slight peak ( $\approx 5$  percent increase) at the transition from the gage section to the shoulder due to bending induced by the shoulder material. Andrews [21] noted a similar phenomenon for this specimen type. The stress response indicated by the finite element model may be employed to assess fatigue damage for failures noted at this location.

For the equal-biaxial tests a double reduced, thin-walled tube with a 25 mm bore and a center section outside diameter of 27.94 mm was used (Fig. 8). The principal difference between this and the previously described specimen was the additional reduction in the center section to an outside diameter of 27.9 mm. The same finite element method was applied to this geometry to determine stress-strain response in the double reduced section and is shown in Figure 9. Figure 9 shows the stress response for biaxial-tension normalized by the maximum stress, and biaxial-compression normalized by the minimum stress.

Pressures and axial loading were determined from elastic thick-walled tube calculations for use in the finite element model. This loading should have resulted in a biaxial stress ratio of +1 on the outer surface if there were no bending induced stresses. The tangential stress gradient was due to thick-walled tube constraints, while the axial stress gradient was caused from bending. These stress gradients produced an outer surface biaxial stress ratio of 0.97.

The specimens were gripped by precision machine collets, eliminating the need to thread the specimens while maintaining excellent alignment. A mandril decoupled the axial stresses and strains from the tangential stresses and strains, allowing more direct control of the principal stresses or strains.

#### 2.5 Test Program

Baseline fatigue data were available for this material [1-5] for uniaxial tests on smooth specimens and for axial, torsional, and combined tests on tube specimens. The baseline data ranged from lives of  $10^3$  to  $10^6$  cycles and included observations of crack formation during testing, which were used to determine damage parameters for Inconel 718 under various multiaxial loading conditions in stress quadrants II and IV. Table 2 lists the material properties of IN718 from the baseline data.

Six biaxial mean stress tests were performed on single reduced, thin-walled tubes (Fig. 6). Mean stress on the maximum shear plane was controlled by maintaining the tangential stress constant at a value of 276 MPa or 517 MPa. The axial cyclic stress or strain loading was completely reversed. This testing technique applied the mean stress in a direction different from the cyclic loading direction. The tests were stopped intermittently so that

acetate replicas of the surface could be taken. Post-failure fracture surface observations on the scanning electron microscope were also performed. Tests were terminated when a specimen cracked through the thickness and lost internal pressure. Test conditions and resulting lives for the biaxial mean stress tests are shown in Table 3a.

Eight biaxial-tension tests were performed, six using specimens shown in Figure 8 and two using specimens shown in Figure 6. Table 3b shows the test conditions and resulting lives for the biaxial-tension tests. The ratio of principal biaxial stress or strain was approximately +1 on the outer surface. Three of these tests were completely reversed ( $R_\sigma$  or  $R_\epsilon = -1$ ), and five were released tension tests ( $R_\sigma$  or  $R_\epsilon = 0$ ). Test levels were selected to achieve three decades of life ( $10^3$  to  $10^6$ ), and the test matrix in Table 3b shows the outer surface test levels and their resulting lives. The test levels of the two  $R_\sigma = 0$  tests, IN01 and IN02, were selected to result in  $\phi_\sigma = +1$  and  $R_\sigma = 0$  on the inner surface.

Surfaces were extensively replicated during all tests except IN01 and IN02. During the replication procedure, tests were temporarily stopped, the pressure system was drained, the specimen was cleaned, and acetate replicas were taken. Post-failure sectioning to identify through thickness cracking directions was also performed. All tests were terminated when loss of internal pressure occurred.

### 3.0 ANALYSIS

A multiaxial fatigue theory must be able to identify correctly the damage parameters for a given material and loading condition. Traditionally, a theory is tested by how well it can correlate the life of a material at different stress states and load levels. Critical plane approaches, such as that introduced by Brown and Miller, go one step further and predict specific damage planes. The presence of damage on these critical planes is manifested physically by cracking.

Five fatigue theories are considered in this analysis: the maximum principal strain theory (St. Venant); the maximum shear strain theory (Tresca); the maximum shear strain modified by the normal strain theory (Brown and Miller); the maximum shear strain modified by the normal strain and the mean normal stress on the maximum shear plane theory (Socie); and the maximum shear strain modified by the maximum stress normal to the shear plane theory (Fatemi and Socie [29]). Each of these theories is able to identify a critical plane for crack initiation. An interpretation is made of the expected cracking behavior based on the damage parameters for each theory.

#### 3.1 St. Venant's Maximum Principal Strain Theory

The maximum principal strain multiaxial fatigue theory is the extension of a static yield theory. The resulting multiaxial strain-life relationship can be derived directly from the familiar uniaxial strain-life relationship.

For multiaxial loading conditions, maximum principal strain amplitude is the only important indicator of damage. To correlate multiaxial fatigue data, the maximum principal strain amplitude can be equated to the uniaxial strain-life equation as follows:

$$\Delta\epsilon_1/2 = \epsilon'_f(2N_f)^c + \frac{\sigma'_f}{E}(2N_f)^b . \quad (4)$$

This direct comparison of maximum principal strain amplitude to the uniaxial strain-life equation is justified because the uniaxial strain amplitude is, in fact, the maximum principal strain amplitude for a cylindrical bar under uniaxial loading conditions. This theory predicts that cracking will be concentrated on planes perpendicular to the maximum principal strain amplitude direction. For a tube under equal-biaxial loading, with its principal strains aligned in the  $\theta$  and  $z$  directions (as in Fig. 2a), the critical planes pass through the surface and are in the same orientation as the  $\tau_r$ -planes in Figure 2c. If an ideal equal-biaxial state of stress exists, then the direction of cracking on the surface has no meaning since, for any rotation about the  $r$ -axis, the same equal-biaxial stress state will exist. The verification of this or any other theory used to predict biaxial-tension fatigue will require examination of the through thickness crack direction.

### 3.2 Tresca's Maximum Shear Strain Theory

The maximum shear strain multiaxial fatigue theory is an extension of the Tresca static yield theory and presumes that the maximum shear strain amplitude is the dominant damage parameter. Halford and Morrow [30] substituted plastic shear strains for the normal strains in the plastic strain-life equation. More recently Leese and Morrow [31] related total maximum shear strain amplitude to the torsional strain-life equation as follows:

$$\hat{\gamma} = \gamma'_f(2N_f)^c + \frac{\tau'_f}{G}(2N_f)^b . \quad (5)$$

This fatigue theory predicts that fatigue damage will be concentrated on the planes of maximum shear strain amplitude. For a tube under equal-biaxial tension, this corresponds to the  $\tau_{\theta}$ -planes illustrated in Figure 2c. Again, the surface cracking direction for this loading is expected to be random.

### 3.3 Brown and Miller's Normal Strain Modified Maximum Shear Strain Theory

Brown and Miller [13] introduced a multiaxial fatigue theory that was based on the physical interpretation of fatigue crack growth. This theory assumes that maximum shear strain is the primary cause of fatigue damage but also adds the tensile strain normal to the plane of maximum shear as a modifying factor. Originally, this theory was presented as:

$$\frac{\epsilon_1 - \epsilon_3}{2} = f \left[ \frac{\epsilon_1 + \epsilon_3}{2} \right] , \quad (6)$$

which represents constant life contours on a graph of maximum shear strain amplitude versus the normal strain amplitude to this shear plane. Kandil, Brown, and Miller [8] later modified this and proposed the following form of Equation 6:

$$\hat{\gamma}^{\alpha} + S \hat{\epsilon}_n^{\alpha} = \text{constant} ; \quad (7)$$

where  $\alpha$  and  $S$  are constants,  $\hat{\gamma}$  is the maximum shear strain amplitude, and  $\hat{\epsilon}_n$  is the amplitude of the normal strain to the maximum shear plane. If  $\alpha$  and  $S$  are taken as unity, then Equation 7 can be directly related to the torsional strain-life equation as follows:



$$\hat{\gamma} + \hat{\epsilon}_n = \gamma'_f(2N_f)^c + \frac{\tau'_f}{G}(2N_f)^b \quad (8)$$

The theory predicts damage will be concentrated on the planes that have the largest combination of maximum shear strain and normal strain amplitudes.

#### 3.4 Socie's Mean Stress Modified Maximum Shear Strain Theory

The mean stress modified maximum shear strain theory and its development were described in detail in the section on background and review of previous work. Equation 3 relates torsional strain-life to this mean stress modified shear strain parameter. The theory predicts that damage will be concentrated on the maximum shear plane with the largest normal mean stress.

#### 3.5 Fatemi and Socie's Maximum Normal Stress Modified Maximum Shear Strain Theory

Fatemi and Socie [29] proposed a critical plane theory for multiaxial fatigue damage to account for out-of-phase cyclic hardening. This theory assumes that shear strains must be present before any fatigue damage can occur but modifies this shear strain with the maximum normal stress during the cycle being considered. The theory was proposed as follows:

$$\hat{\gamma}(1 + \eta\sigma_n^{\max}/\sigma_y) = \text{constant} \quad , \quad (9)$$

where  $\eta$  is a constant determined from baseline axial and torsional data, and  $\sigma_n^{\max}/\sigma_y$  is the maximum normal stress during the cycle, normalized by the yield stress. If  $\eta$  is taken as unity, then this theory can be related to the torsional strain-life equation as follows:

$$\hat{\gamma}(1 + \sigma_n^{\max}/\sigma_y) = \gamma_f'(2N_f)^c + \frac{\tau_f'}{C}(2N_f)^b . \quad (10)$$

This theory predicts that damage will concentrate on the shear plane with the highest value of the Fatemi-Socie damage parameter (Eq. 9). For a tube under biaxial tension this would correspond to the  $\tau_\theta$ -planes shown in Figure 2c.

All of the fatigue theories discussed here, with the exception of the maximum principal strain theory, predict that through thickness cracking will occur on the  $\tau_\theta$ -planes for biaxial-tension. The life predicting capabilities of these models will be assessed and further tested by biaxial mean stress tests.

## 4.0 STRESS-STRAIN ANALYSIS

### 4.1 Cyclic Stresses and Strains

Before any fatigue theory can be evaluated, a stress-strain analysis must be performed to determine all of the principal stresses and strains at the location of interest. All biaxial-tension tests were cyclically elastic, allowing stress and strain amplitudes to be computed from Lamé's elastic solution [32]:

$$\sigma_r = \frac{r_i^2 p_i - r_o^2 p_o}{r_o^2 - r_i^2} - \frac{(p_i - p_o) r_i^2 r_o^2}{(r_o^2 - r_i^2) r^2} , \quad (11)$$

and

$$\sigma_\theta = \frac{r_i^2 p_i - r_o^2 p_o}{r_o^2 - r_i^2} + \frac{(p_i - p_o) r_i^2 r_o^2}{(r_o^2 - r_i^2) r^2} . \quad (12)$$

where  $r_i$ ,  $r_o$ ,  $p_i$ , and  $p_o$  represent the inside radius, outside radius, internal pressure, and external pressure respectively.

The use of a mandril eliminates internal pressure induced axial stress, so the axial stress is calculated as follows:

$$\sigma_z = P_z / (\pi(r_o^2 - r_i^2)) . \quad (13)$$

The elastic strains may be computed using the theory of elasticity [32]:

$$\epsilon_z = [\sigma_z - \nu(\sigma_\theta + \sigma_r)]/E , \quad (14)$$

$$\epsilon_\theta = [\sigma_\theta - \nu(\sigma_z + \sigma_r)]/E , \quad (15)$$

$$\epsilon_r = [\sigma_r - \nu(\sigma_\theta + \sigma_z)]/E . \quad (16)$$

Additional corrections for bending are made using the elastic finite element analysis previously described for each geometry.

#### 4.2 Residual Stresses Due to Yielding on the First Reversal

Initial yielding of the tube, as in some  $R_\epsilon = 0$  tests, affects mean stress values but does not affect the subsequent values of the alternating stress range, assuming that the geometry of the tube was not changed significantly by yielding [33].

An estimate of the residual stresses on the inner surface resulting from initial yielding can be made using the loading conditions observed in the first reversal. One method of calculating the stress redistribution was performed by Chakrabarty [34] as follows. Assume a Tresca yield condition where  $\sigma_z$  is an intermediate principal stress and does not enter into the calculation. For biaxial-tension with  $\sigma_\theta = \sigma_z$  this yield condition still holds since  $\sigma_r \leq \sigma_z \leq \sigma_\theta$ . When internal pressure exceeds a critical level, the inside of the tube begins to deform plastically. This plastic region spreads outward, with the elastic-plastic boundary occurring at radius  $c$  (Fig. 10). The elastic region can still be described using Lamé's equations with new boundary conditions of  $\sigma_r = 0$  at  $r = r_o$  and noting that the yield condition exists at  $r = c$ . The elastic radial and tangential stress distribution can be written as follows:

$$\sigma_r = - \frac{\sigma_y c^2}{2r_o^2} \left( \frac{r_o^2}{r^2} - 1 \right) , \quad (17)$$

$$\sigma_{\theta} = \frac{\sigma_y c^2}{2r_o^2} \left( \frac{r_o^2}{r^2} + 1 \right) , \quad (18)$$

for  $c \leq r \leq r_o$ . Again, under the assumption that  $\sigma_z$  is an intermediate principal stress everywhere in the plastic region and that the material is nonhardening, the radial and tangential stresses are given by

$$\sigma_r = -\frac{\sigma_y}{2} \left( 1 - \frac{c^2}{r_o^2} + \ln \frac{c^2}{r^2} \right) , \quad (19)$$

$$\sigma_{\theta} = \frac{\sigma_y}{2} \left( 1 - \frac{c^2}{r_o^2} + \ln \frac{c^2}{r^2} \right) , \quad (20)$$

for  $r_i \leq r \leq c$ .  $\sigma_r$  and  $\sigma_{\theta}$  are independent of the end conditions. The internal pressure required to generate the plastic zone for  $r_i \leq r \leq c$  is given by

$$p_i = \frac{\sigma_y}{2} \left( 1 - \frac{c^2}{r_o^2} + \ln \frac{c^2}{r_i^2} \right) . \quad (21)$$

If this tube is then unloaded by removing the internal pressure, elastic unloading will occur. The residual stresses can be computed by subtracting the purely elastic solution from the elastic-plastic solution with the following results:

$$\sigma_r = -\frac{\sigma_y}{2} \left( \frac{c^2}{r_i^2} - \frac{p}{p_c} \right) \left( \frac{r_i^2}{r^2} - \frac{r_i^2}{r_o^2} \right) , \quad (22)$$

$$\sigma_{\theta} = \frac{\sigma_y}{2} \left( \frac{c^2}{r_i^2} - \frac{p}{p_o} \right) \left( \frac{r_i^2}{r^2} + \frac{r_i^2}{r_o^2} \right) , \quad (23)$$

for the elastic region  $c \leq r \leq r_o$ , and

$$\sigma_r = -\frac{\sigma_y}{2} \left[ \frac{p}{p_c} \left( 1 - \frac{r_i^2}{r^2} \right) - \ln \frac{r^2}{r_i^2} \right] , \quad (24)$$

$$\sigma_\theta = -\frac{\sigma_y}{2} \left[ \frac{p}{p_c} \left( 1 + \frac{r_i^2}{r^2} \right) - \left( 2 + \ln \frac{r^2}{r_i^2} \right) \right] , \quad (25)$$

for the plastic region  $r_i \leq r \leq c$ . The  $\sigma_\theta$  residual stress distribution after elastic unloading is shown in Figure 11 for the double reduced specimen. For a fully plastic loading cycle the  $\sigma_\theta$  residual stress is shown to be approximately linear at a value of  $-0.1\sigma_y$  on the inside surface and  $+0.09\sigma_y$  on the outside surface. Since the material was assumed to be nonhardening, this will be the highest residual state allowed for this geometry. Upon unloading from a fully plastic cycle, an axial residual stress will also result, with values of  $+0.027\sigma_y$  on the outer surface and  $-0.03\sigma_y$  on the inside surface. Ten possible  $\sigma_z$  residual stress distributions, ranging from fully elastic to fully plastic tangential expansion, are shown in Figure 12.

The residual stress analysis just developed was used to estimate the stress redistribution for the  $R_e = 0$  biaxial-tension tests where specimens incurred plastic deformation during the first load reversal.

#### 4.3 Stress-Strain for Biaxial Mean Stress Tests

Lame's equations were used to calculate stresses for the elastic biaxial mean stress tests. For tests that exhibited reversed plasticity in the axial direction, the elastic and plastic values of strain in the axial direction were taken from the stress-strain loops. Elastic stress-strain values for the tangential and radial directions were calculated from the elastic Lamé's

solution. Plastic strains were calculated, assuming constancy of volume ( $\nu = 0.5$ ), with the following equation:

$$\epsilon_z^p = -\frac{\nu}{1-\nu}(\epsilon_r^p + \epsilon_\theta^p) ; \quad (26)$$

if  $\epsilon_\theta^p$  is assumed to equal  $\epsilon_r^p$ , since plastic strain is in the z direction, then

$$\epsilon_\theta^p = \epsilon_r^p = -\epsilon_z^p/2 . \quad (27)$$

The elastic and plastic strains are then combined to determine the total strain values in the tangential and radial directions.

## 5.0 RESULTS AND OBSERVATIONS


### 5.1 Crack Observations

Surface initiation and growth of cracks as well as through thickness growth direction were observed for the biaxial-tension tests. If the state of stress on a specimen's outer surface is truly equal-biaxial, then the maximum shear plane will intersect the surface at 45 degrees and can take any orientation on the specimen surface. For this reason there should be no definite crack orientation on the surface. The relative percent of the fatigue life spent initiating versus growing a crack can easily be determined from surface crack replicas when the cracks initiate on the outer surface. An estimate of the amount of crack growth in Mode II (shear dominated) versus Mode I (maximum principal stress dominated) can be made by combining the through thickness crack direction observations with the surface length observations, assuming that the shape of the crack is elliptical and of the same aspect ratio as the failure crack. Crack observations will be described for the biaxial-tension  $R_\sigma = -1$  tests and then for the  $R_\sigma = 0$  and  $R_\epsilon = 0$  tests.

#### 5.1.1 Equal-Biaxial Tests, Completely Reversed

Three  $R_\sigma = -1$  tests were performed ranging in life from less than  $4 \times 10^3$  to  $1.3 \times 10^5$  cycles. The shortest life test, INDM01, lasted 3739 cycles. The Mohr's circles of stress and strain and the test details are shown in Figure 13. Surface cracking and the etched through thickness pictures are shown in Figure 14. This was a nominally elastic test begun in strain control using gages in the anticipated failure location. To ensure against a strain gage failure ruining the test, the test was switched to load and pressure control after approximately 200 cycles. Crack initiation occurred between 1000 and





2000 cycles with regions of intense slip throughout the test section becoming apparent by cycle 2000. These regions did not appear to be preferentially aligned to the specimen. The region of intense slip shown in Figure 14 (N = 2000) is contained within a single grain. The failure surface became severely cracked, and the specimen failed by the linking of smaller cracks to form the failure crack. Strain gages were removed with a solvent, and the surface morphology under the gages appeared the same as material, adjacent to the failure crack, that had been exposed to the hydraulic fluid. Though inconclusive, this finding suggests that the effects of hydrowedging are minimal. The through thickness crack direction is shown in Figure 14; the specimen shown here was sectioned longitudinally, polished, and etched to reveal general microstructure. The crack appears to have initiated and grown to failure on the maximum shear plane. While shear cracks can be seen on both the inner and outer surfaces, crack density on the outside is considerably higher than on the inside, indicating that the failure crack was initiated from the outside surface. The assumption that the failure region is still polycrystalline is correct since this region contains 30 to 50 grains through its thickness.

The intermediate life  $R_{\sigma} = -1$  test was INDM05, which lasted 58,084 cycles. The Mohr's circles of stress and strain and the details for this test are given in Figure 15. Surface cracks and through thickness crack details are shown in Figure 16. The circular photos inset in Figure 16 are through thickness cracking profiles of the failure crack, and arrows point to the location along the failure crack where the specimen was cut. This was an elastic load-pressure controlled test. The first sign of cracking was seen at approximately 20,000 cycles (34 percent of the failure life). Subsequent surface cracks wander in all directions--even, in some cases, in a nearly

circular path. Through thickness crack directions at the center and end of the crack are inset in Figure 16. The crack initiated from the outer surface, as can be seen by the through thickness crack near the end of the failure crack. Initiating on a maximum shear plane, the failure crack plane zigzagged to a depth of about one-quarter of the specimen thickness (approximately 0.35 mm). The through thickness cracking then appeared to follow a direction normal to the maximum principal stress with an occasional jog on a maximum shear plane.

An estimate of the surface crack length when the through crack direction changed from Mode II growth to Mode I can be made if the crack shape is known, so the crack shape was estimated by measuring the surface length to crack depth ratios of several shear cracks at various degrees of penetration. Aspect ratios were found to vary from 0.46 to 0.36. Using this range of aspect ratios, the surface crack length corresponding to the transition from Mode II to Mode I crack growth would be between 0.76 mm to 0.97 mm. Another estimate of surface crack length can be made using curve fitted crack profiles by Beer [3] for another state of stress. This results in an aspect ratio of approximately 0.33, which would correspond to a surface crack length of roughly 1 mm. For this test 95 percent of the fatigue life was spent initiating and growing shear cracks.

The longest life  $R_{\sigma} = -1$  test was INDM03, which lasted 126,628 cycles. Mohr's circles of stress and strain and details of this test are shown in Figure 17. This was an elastic load-pressure controlled test that ended with two cracks greater than 1 mm in length. The failure crack for this test (Fig. 18) was less than 1 mm long at 95 percent of the fatigue life, while a second crack (Fig. 19) was approximately 1.5 mm long and first appeared at 38,000

cycles (approximately 30 percent of life). The failure crack formed by the rapid linking of many smaller cracks. Again, the surface cracks appeared to have no particular orientation. Figure 18 shows the through thickness crack profile at the center and near the end of the failure crack. Shear growth near the center of the crack appeared to continue roughly halfway through the thickness, corresponding to a surface crack length of approximately 2 mm, and shear crack initiation and growth constituted 95 percent of the fatigue life for this test. Near the end of the test, the cracking mode changed from Mode II to Mode I.

The second crack is shown in Figure 19. This crack was evident very early in the test and had an entirely different orientation from the failure crack. Surface cracking had no preferred orientation and, in some cases, grew in a nearly circular path. The crack was etched to reveal general microstructure and to determine if the holes visible on the surface were grains that were extruded during the fatigue process. Figure 20 shows the sectioned and etched crack. Here it can be seen that the crack was almost 90 percent of the way through the specimen and needed only to propagate through a few grains to become a failure crack. The shear growth region of this crack, like that of the failure crack, was approximately halfway through the thickness but had many shear cracks joining in the through thickness direction. Again, the mode of crack growth appeared to change from Mode II to Mode I when the surface crack length reached approximately 2 mm. This also indicated that approximately 95 percent of the fatigue life was spent initiating and growing these shear cracks.

### 5.1.2 Biaxial-Tension Tests, Released Tension

One  $R_\epsilon = 0$  and four  $R_\sigma = 0$  tests were performed and resulted in lives ranging from  $2 \times 10^4$  to  $1.4 \times 10^5$  cycles. In all of these tests, shear cracks initiated from the inside surface. Though some cracks did form early in life on the outer surface, the failure cracks were not visible on the outer surface until the test ended, and since the failure cracks were not observable from the replicas, only a rough estimate of the fraction of fatigue life spent initiating and growing shear cracks is possible based on surface crack measurements. The released tension through thickness crack profiles resembled those of the completely reversed tests in that the shear growth penetrated one-fifth to one-half the wall thickness before changing to Mode I type crack growth. There did appear to be a favored shear plane that caused all the released tension failure cracks to be aligned with the z-axis. This is not surprising, since test levels were chosen so that the outer surface would be in equal-biaxial tension. When the outer surface is in an equal-biaxial state of stress, the inner surface has a higher tangential loading than axial loading; failure cracks are thus driven in the axial direction.

The shortest life  $R_\epsilon = 0$  test was INDM07, lasting 20,262 cycles. The Mohr's circles of stress and strain for the inner surface and the test details are shown in Figure 21; Figure 22 shows surface and through thickness crack pictures. Initially, the specimen was equal-biaxially strained to 0.0044 and then unloaded; axial and diametral strains were cycled elastically from 0 to 0.0042 on the outer surface. This slight overstrain prevented the ratcheting of the specimen. Figure 23 shows surface measured tangential stress-strain response for the setup cycle and subsequent elastic cycles. The setup cycle established a slight tensile residual stress at the outer surface while the

inner surface became compressive, resulting in a residual stress gradient. Estimates were made of the residual stresses, assuming that the tube went completely plastic during the setup cycle, and of the radial and tangential stresses using Equations 24 and 25 with the pressure set equal to the fully plastic pressure. Tangential residual stresses were estimated to be -110 MPa on the inner surface and 106 MPa on the outer surface. Axial residual stresses, calculated using Hooke's law, were estimated to be -31 MPa on the inner surface and 28 MPa on the outer surface. Residual stresses on the inner surface have been included in the values shown in the Mohr's circles in Figure 21. Compressive residual stresses on the inner surface did not affect the elastic cyclic conditions whereby the inner surface underwent a greater cyclic stress-strain range than the outer surface.

A close inspection of the through thickness crack for INDM07 in Figure 22 revealed a crack from the outer surface that penetrated approximately one-third the wall thickness. The failure crack that initiated on the inner surface linked with this smaller crack from the outer surface.

The first observable surface cracks appeared at approximately 30 percent of the specimen's life. Since the failure crack initiated at the inside surface it was assumed that at any time during the test the crack lengths would be greater on the inside than the outside surface. It should have required fewer cycles to initiate a crack on the inner surface than the outer surface. If the first outer surface cracks appeared at 30 percent of the fatigue life, then the percent of the fatigue life spent initiating a crack on the inner surface must have been less than 30 percent. Also, the number of cycles spent initiating and growing shear cracks would be slightly overestimated if derived from observations of the outer surface. Based on outer surface measurements

this test is estimated to have spent 95 percent of the fatigue life nucleating and growing shear cracks, implying that the Mode I crack growth occupied an insignificant portion of the fatigue life.

The intermediate life  $R_{\sigma} = 0$  test was INDM08, lasting 25,656 cycles. The Mohr's circles of stress and strain for the inner surface as well as the test details are shown in Figure 24. Surface and through thickness crack details are shown in Figure 25. This test was planned to be all elastic, but a very small amount of plastic strain (less than 100 microstrain) occurred on the first cycle. Estimates of the resulting residual stress on the inner surface were made using the analysis derived earlier with a tangential residual stress of 93Mpa and an axial residual stress of -30Mpa. Load and pressure were used as the control parameters for this test. Again, surface cracks were very difficult to find; most of the cracking occurred from the inside toward the outside surface. A look at the through thickness cracking showed a shear growth region from the inner surface to approximately one-fourth the wall thickness, at which point the crack growth changed to a Mode I type. The orientation of the failure crack, with minor deviations, was aligned with the z-axis. The first visible surface cracks appeared at approximately 10 percent of the fatigue life. Greater than 80 percent of the specimen's total life was required to initiate and grow a 1.0 mm crack.

Two additional tests performed by Commer [35] were controlled to give a 0 to 1034 Mpa stress range on the inner surface. These tests, designated IN01 and IN02, used the single reduced specimen shown in Figure 6 and lasted 30,790 and 35,910 cycles, respectively. The Mohr's circles of stress and strain for the inner surface are shown in Figures 26 and 27, and failure crack details are shown in Figure 28.

The longest life  $R_{\sigma} = 0$  test was INDM06, which lasted 142,836 cycles. The test details and the Mohr's circles of stress and strain on the inner surface are shown in Figure 29. Crack details are shown in Figure 30. This was an elastic, load-pressure controlled test. The first sign of cracking occurred at 28 percent of the fatigue life, with 87 percent of the fatigue life spent initiating and growing a 1.0 mm crack. The failure crack was aligned with the z-axis and initiated from the inner surface. Through crack details in Figure 30 reveal shear growth to roughly one-fifth the specimen through thickness, followed by Mode I growth through the remainder of the thickness.

#### 5.1.3 Biaxial Mean Stress Tests

Biaxial mean stress tests were performed to test further the ability of the various fatigue theories to account for mean stresses. It was assumed here that the maximum shear plane would be the plane of initiation. Mean stress on the maximum shear plane was controlled by allowing the resolved hoop stress to equal the required mean stress while the axial stress or strain was cycled. This technique applied the mean stress normal to the cyclic loading direction. The Mohr's circles of stress and strain are shown in Figure 31 for an elastic biaxial mean stress test. For this type of loading case  $\Delta\gamma_{rz}$  and  $\Delta\gamma_{z\theta}$  have the same value; however, the mean stress associated with the  $\Delta\gamma_{rz}$  planes is zero, while the  $\Delta\gamma_{z\theta}$  planes have a mean stress of  $\sigma_{\theta}/2$ . The mean stress present on the  $\Delta\gamma_{r\theta}$  plane is the same as the  $\Delta\gamma_{z\theta}$ ; for this test,  $\Delta\gamma_{r\theta}$  has a value of zero. Therefore, shear cracks will initiate on the  $\Delta\gamma_{z\theta}$  planes. The surface cracking for these tests should exhibit a preferred cracking direction of 45 degrees from the z-axis.

Six tests were conducted, two at each test level, and resulted in fatigue lives ranging from  $3.3 \times 10^3$  to  $1.7 \times 10^5$  cycles. The shortest life tests were INA4 and INA17, which lasted 3654 and 3293 cycles, respectively. These were mixed mode controlled tests where the axial strain was cycled between  $\pm 0.005$ , while the tangential stress was maintained at 517 Mpa on the outer surface. Test conditions and resulting Mohr's circles of stress and strain for these two tests are shown in Figures 32 and 33. The stress states illustrated are for the outer surface where the surface cracks initiated. The total strains in the  $\theta$  and  $r$  directions were calculated using the technique described in the strain analysis section and Equations 26 and 27. Surface crack details are presented in Figures 34 and 35 and show a definite preference for crack growth on the  $\Delta\gamma_{z\theta}$  planes that are at 45 degrees to the  $z$ -axis. Cracking occurred on complementary planes and resulted in a jagged crack that grew by linking many smaller cracks.

Another set of mixed mode tests was performed with the axial strain cycled between  $\pm 0.005$  and the tangential stress maintained at 276 Mpa on the outer surface. These were denoted as INA13, which lasted 7221 cycles, and INA5, which lasted 6735 cycles. The test conditions and resulting Mohr's circles of stress and strain for the outer surface are shown in Figures 36 and 37, and surface crack details are shown in Figures 38 and 39. The cracking resembled that of the previous mean stress test in that the cracks grew by the linking of smaller shear cracks. The overall crack appearance again was jagged, caused by complementary  $\Delta\gamma_{z\theta}$  planes initiating and linking cracks.

The longest life biaxial mean stress tests were cycled axially between  $\pm 517$  Mpa while the tangential stress was maintained at 517 Mpa on the outer surface. These elastic tests, denoted INA12 and INA23, lasted 142,061 and



165,088 cycles, respectively. Figures 40 and 41 depict the test conditions and resulting Mohr's circles of stress and strain on the outer surface, and surface crack details are shown in Figures 42 and 43. Tangential and radial strains were calculated from Lamé's equations and the theory of elasticity. Again, cracking was concentrated on the maximum shear plane with the highest mean stress. The jagged nature of the cracks was once more attributed to the linking of smaller cracks to form larger cracks.

#### 5.1.4 Summary of Cracking Observations

Failure cracks, which were easily observed on the outer surface for all tests except the released tension tests, initiated from the outside surface for completely reversed biaxial-tension loading and from the inside for the released tension case. Biaxial mean stress tests failed by the linking of many smaller shear cracks.

All of the tests resulted in failure cracks that initiated and grew in shear. Roughly 90 percent of the fatigue life was spent initiating and growing these shear cracks to a surface length of 1.0 mm. Transition from Mode II to Mode I crack growth occurred at 90 to 95 percent of the fatigue life.

For cracks of up to 1.0 mm surface length, crack aspect ratios were the same as those observed in other states of stress.

#### 5.2 Life Predictions

Experimental life results were compared with baseline uniaxial and torsional data. For each specimen, damage calculations were made at the failure location. Outer surface stresses and strains were used for the completely

reversed and mean stress tests, while inside surface values were used for the released tension tests because an increase in calculated damage of approximately 10 percent results if the inside surface values are used for the completely reversed and mean stress tests. All of the values required to estimate fatigue life can be taken directly from the Mohr's circles of stress and strain presented earlier for each test.

Correlations of the biaxial-tension and biaxial mean stress data with the multiaxial fatigue theories described earlier are displayed in Figures 44-48. In these figures biaxial-tension tests are indicated by circles, completely reversed tests are represented by solid circles, and released tension tests are represented by open circles. Biaxial mean stress tests are indicated here by the open triangles. The dashed line depicts uniaxial baseline data while torsional baseline data are illustrated by a solid line.

Figure 44 shows maximum principal strain amplitude versus cycles to failure for the biaxial mean stress and biaxial-tension tests. This fatigue theory has overestimated fatigue life, with the mean of the life predictions nonconservative by a factor of 26 compared to the uniaxial baseline data. Fatigue life predictions for 86 percent of the tests are correlated within a scatterband in life of a factor of 64.

Tresca's theory of maximum shear strain amplitude versus cycles to failure is shown in Figure 45. Since this is a shear based fatigue theory, torsional baseline data are used here rather than uniaxial data and are represented by the solid line. The mean of the life predictions for this theory was overestimated by a factor of 11 when compared to the torsional baseline data, with 86 percent of the tests correlated within a scatterband in life of a factor of 16.

Brown and Miller's theory (Eq. 8) was used to correlate the fatigue data and is shown in Figure 46. Fatigue life predictions based on this theory are nonconservative by an average of a factor of 6 compared to the torsional or uniaxial baseline data, with 86 percent of the tests correlated within a scatterband in life of a factor of 10.

Correlation of the data using Socie's mean stress modified shear strain theory (Eq. 3) is shown in Figure 47. Mean fatigue life prediction for this theory was nonconservative by a factor of 2 when compared to the torsional or uniaxial baseline data, with 86 percent of the tests falling within a scatterband in life of a factor of 7.

Figure 48 displays the correlation of fatigue data using Fatemi and Socie's maximum normal stress modified shear strain theory (Eq. 9) with the parameters  $\eta = 1.0$  and  $\sigma_y = 1160$  MPa. Life predictions based on this theory were more centrally distributed about the baseline data; the mean life prediction was only a factor of 1.4 nonconservative, bringing 86 percent of the tests within a scatterband in life of a factor of 4.2.

#### 5.2.1 Summary of Life Predictions

Life predictive capabilities of the multiaxial fatigue theories discussed above improved as terms were added that affected shear crack initiation and growth. The poorest correlation came from the maximum principal strain theory, which was nonconservative by as much as a factor of 84. Fatemi and Socie's theory resulted in the best correlation, with 93 percent of the data distributed about the torsional baseline data within a factor of 6 in life.

## 6.0 DISCUSSION

Post-failure sectioning of the specimens revealed an anomaly; failure cracks initiated on the inside for the released tension tests and on the outside for completely reversed tests. To determine whether pressure induced local bending stresses that occur during the compressive cycle were much higher on the outside than on the inside, an elastic finite element analysis was performed with loading conditions that matched the completely reversed tests. Specimen response was very nearly symmetric with regard to bending induced stresses. The axial stress gradient caused by bending was roughly equal to, though in the opposite direction of, the tangential stress gradient caused by the thick-walled cylinder conditions. For example, during the tensile peak of a cycle the axial stress was higher on the outside surface than on the inside due to bending, while the tangential stress was higher on the inside surface than on the outside due to thick-walled cylinder constraints. The most highly stressed region was still on the inside surface with a stress magnitude roughly 10 percent higher than that of the outside surface.

This anomaly--initiation of the failure cracks on the inside versus the outside surface--cannot be predicted by any of the fatigue theories considered, nor can it be directly explained by the stress response from finite element modeling of the tensile and compressive cycles. The biaxial stress ratio was higher on the outer surface than on the inner surface for the completely reversed tests. This was the only consistent condition that could account for the initiation of failure cracks at the outer surface.

Initiation sites in the biaxial mean stress tests occurred in the region of 5 to 10 micron inclusions. Inclusion initiation sites were observed on both

inner and outer surfaces. The presence of these inclusions may have caused the higher biaxial stress ratio on the outer surface to be more effective in nucleating cracks for the completely reversed tests.

### 6.1 Evaluation of Fatigue Theories

Life predictions for the biaxial-tension and biaxial mean stress tests were based on the multiaxial fatigue models described earlier. The ability of any fatigue model to predict accurately fatigue life has traditionally been the primary test of the theory. For this work the ability to predict cracking behavior was considered as important as the life predictive ability. A discussion of the different theories in terms of their effectiveness in predicting both cracking behavior and fatigue life follows.

The maximum principal strain theory was the only nonshear-based theory used, and it predicted that cracks would initiate on the planes normal to the maximum principal strain amplitude. None of the biaxial-tension or biaxial mean stress tests exhibited cracking on these planes of maximum principal strain. Regarding its life predictive capabilities, this theory failed to correlate the biaxial-tension data to any usable degree, as seen in Figure 44. Biaxial mean stress data were correlated to the uniaxial baseline data within a factor of 3; the correlation deteriorated as the mean stress increased. The mean fatigue life of the completely reversed biaxial-tension tests was nonconservative by a factor of 20, while the mean life of the released tension tests was nonconservative by a factor of 60.

The maximum principal strain theory was included for comparison with shear based theories since it is equivalent to the uniaxial strain-life approach.

This theory should not be used to analyze this metal in stress quadrants I and III since it can predict neither life nor cracking behavior.

While the maximum shear strain theory did predict the correct plane of cracking for the biaxial-tension tests, it did not distinguish the  $\gamma_{\theta z}$  failure planes from the  $\gamma_{rz}$  planes in the biaxial mean stress tests. For example, from the biaxial mean stress test INA13,  $\hat{\gamma}_{\theta z} = \hat{\gamma}_{rz}$  and has a value of 0.00646 (Fig. 37). Since biaxial mean stress tests consistently cracked on the  $\hat{\gamma}_{\theta z}$  planes, the theory must omit an important parameter for predicting cracking behavior. This theory, as depicted in Figure 45, correlated the data within a scatterband in life of a factor of 28. Completely reversed and biaxial mean stress tests were correlated within a scatterband in life of a factor of 9 with the mean life prediction nonconservative by a factor of 7. Correlations of the released tension tests were poor when compared to torsional baseline data; the mean life prediction was nonconservative by a factor of 18, and the data fell within a scatterband in life of a factor of 26. Shear strain amplitude must be the fundamental parameter for predicting fatigue damage in stress quadrants I and III, as the maximum shear strain theory was able to predict cracking behavior for most of the tests. Addition of a mean stress or mean strain parameter is needed to correlate the released tension tests.

Brown and Miller's theory, by adding normal strain amplitude to the maximum shear plane, improved life predictions slightly but still did not distinguish the failure  $\hat{\gamma}_{\theta z}$  planes from the  $\hat{\gamma}_{rz}$  set of planes in the biaxial mean stress tests.

Socie's mean stress modified Brown and Miller theory, which added the effect of mean normal stress, predicted the correct plane of cracking for all biaxial-tension and biaxial mean stress tests. Clearly, the mean normal

stress term was important for predicting the planes of cracking in this material. Life predictive capabilities were significantly improved as well, with the life prediction for the shortest completely reversed biaxial-tension test overestimated by a factor of 9, while all the other tests are correlated within a factor of 6 compared to torsional baseline data.

Fatemi and Socie's theory predicted the correct planes of cracking for all biaxial-tension and biaxial mean stress tests. As noted earlier, this theory has an added advantage in that no damage is calculated without cyclic shear strain. Also, damage occurring from out-of-phase loading, where the maximum stress and strain do not occur at the same point during the cycle, can be accommodated using the maximum normal stress on the plane of maximum shear strain amplitude. This theory yielded the best life predictions of all the theories considered, with test data more centrally distributed about the torsional and axial baseline data. The longest life released tension biaxial-tension test was nonconservative by a factor of 6, while the remaining biaxial test data fell within a factor of 3 of the torsional baseline data.

Cracking behavior and life predictive capabilities of the multiaxial fatigue theories discussed here improved as parameters were added that influenced Mode II crack initiation and growth process. Terms that influenced Mode I crack growth were effective for only a few percent of the total fatigue life, if at all, and are therefore not worth considering.

## 6.2 Critical Comparisons of Fatigue Behavior in All Stress Quadrants

The biaxial fatigue research described in this thesis can be combined with previous research [1-7] on multiaxial fatigue in quadrants II and IV to allow a more complete understanding of the multiaxial fatigue behavior of Inconel

718 in all stress quadrants. The complicated interactions of stress state, stress or strain amplitude, and cracking behavior (i.e., damage mechanisms) for this metal are most easily comprehended through the use of fatigue damage maps as proposed by Socie [36].

Socie described the fatigue damage occurring in ductile metals based on observations of the primary failure mechanisms and grouped these into three distinct categories: Type A, Type B, and Type C. In his categorization, Socie described Type A fatigue damage as shear initiation followed by shear crack growth. Failure for this type of damage occurred when enough smaller shear cracks linked to form a critical size crack. Shear crack growth was thus considered the primary failure mode for Type A fatigue damage. Like Type A damage, Type B fatigue damage began with shear initiation but ended with tensile crack growth to failure. This tensile crack growth was the primary failure mode for Type B fatigue damage. Type C fatigue damage, on the other hand, exhibited no observable shear initiation or may have comprised shear initiation of nonpropagating cracks. For Type C fatigue damage, Socie demonstrated the importance of shear stresses for ductile metals, whereas principal stresses should be considered for defect dominated materials.

The fatigue maps shown in Figure 49 illustrate the cracking behavior of Inconel 718 for the stress states of torsion, tension, and biaxial-tension loadings over a life range from 100 to  $10^7$  cycles. The horizontal axis represents cycles to failure, and the vertical axis represents life fraction. Three types of cracking behavior are presented in these maps: crack nucleation, shear crack growth, and tensile crack growth. Fatigue damage must start by the nucleation of a crack; on the damage maps this process is expressed by the lower solid line. Once initiated, a fatigue crack may grow as a shear



crack or as a tensile crack, depending on the stress or strain amplitude. For stress levels that result in fatigue lives of less than  $10^5$  cycles, from 10 to 40 percent of the life is spent nucleating a crack, while the remaining portion of life is spent in shear crack growth. This is denoted as Region A in Figure 49 and represents the region where Type A fatigue damage occurs. Inconel 718 is unusual in that Type A fatigue damage dominates for lives less than  $10^6$  cycles for all stress states, as can be seen by comparing the life range of Region A for the three stress states shown in Figure 49. Since the cracking behavior does not change from one stress state to another, exact details of the damage mechanisms are, in effect, unnecessary. The complex interactions between microstructure and stress systems need not be completely understood to predict accurately cracking behavior and fatigue lives for this metal.

### 6.3 Research Limitations

The limited number of tests performed in stress quadrants I and III prevents statistical assessment of these data. The focus of this research has been on understanding cracking behavior to gain confidence in an appropriate fatigue theory, rather than on attempting to generate a large amount of test data. As a consequence of understanding cracking behavior, fatigue tests from less complex stress states can provide the statistical confidence needed for design purposes.

This research program has been confined to ambient temperature, low strain rates, constant amplitude cycles, ideal specimen geometries, and controlled surface finishes. Variations in these parameters may affect cracking behavior

and need to be carefully considered when using this research to estimate the fatigue performance of a component.

#### 6.4 Summary of Discussion

The damage maps in Figure 49 illustrate that most of fatigue test life is spent growing shear cracks for all three represented stress states. Therefore, a multiaxial fatigue theory must be sensitive to shear crack initiation and growth. The Fatemi and Socie theory demonstrates this sensitivity and describes shear nucleation and crack growth for Inconel 718 better than any other theory considered.

In Figure 50, the Fatemi and Socie theory is used to correlate all the biaxial fatigue data generated for Inconel 718 at the University of Illinois to date, including test data from all stress quadrants as well as out-of-phase results. Open circles represent the completely reversed loading paths A and B illustrated in Figure 3, open triangles represent loading paths D to L, and open squares show the out-of-phase loading paths M to O. Solid circles represent the biaxial-tension and biaxial mean stress tests. Uniaxial tension tests from smooth specimens, represented by x, include strain ratios of -2, -1, 0, and 0.2. Fatemi and Socie's theory correlates this vast range of testing conditions very well with over 90 percent of the tests distributed within a scatterband of a factor of 5 in life. Fatigue lives above  $10^6$  cycles are controlled by inclusions. This results in increased scatter in the data at long life, as shown in Figure 50 for the uniaxial tests lasting greater than  $10^6$  cycles. Of equal importance is the fact that the theory accurately predicts the cracking behavior of Inconel 718 for the wide range of loading paths and stress states considered.

## 7.0 CONCLUSIONS

1. The best overall correlation of cracking behavior and fatigue lives was obtained using Fatemi and Socie's multiaxial fatigue theory. This theory should accurately predict cracking behavior and fatigue life for any combined stress state, since the primary failure mode remains shear crack growth for all stress quadrants, and should work well on any metal within the life regime where the primary failure mode is shear crack growth to failure.
2. Biaxial-tension loading initiates many cracks that continue to grow in shear and eventually link to form the failure crack.
3. Crack nucleation occurs within the first 30 percent of the fatigue life, with the remaining cycles spent growing these cracks in shear. Shear crack growth is the primary failure mode over the life range from  $10^2$  to  $10^6$  cycles.
4. Transition from shear crack growth to tensile crack growth occurred when the surface crack length reached 0.75 mm to 1.0 mm. Tensile crack growth occurred late in life for the long life tests and occupied at most 15 percent of the fatigue life.
5. The aspect ratios of surface cracks up to 1.0 mm in length, measured by post-failure sectioning of the biaxial-tension specimens, are similar to ratios measured in tension and torsion.

TABLES

TABLE 1 Chemical Composition and Heat Treatment for Inconel 718

a) Inconel 718 Chemical Composition, wt%

<u>Element</u>	<u>wt%</u>
Ni	52.12
Cr	18.23
Fe	19.48
Nb	5.03
Mo	2.89
Ti	1.01
Al	0.54
Co	0.28
Mn	0.09
Si	0.06
Cu	0.05
C	0.034
P	0.007
B	0.0035
S	0.001

b) Inconel 718 Heat Treatment Procedure

Solution treated at 968°C for 1 hour; oil quenched then aged at 832°C for 8 hours; furnace cooled at 55°C per hour to 635°C; held at 635°C for 8 hours then air cooled.

TABLE 2 Material Properties for Inconel 718

Monotonic Properties

E	Modulus of Elasticity	209 GPa
$\sigma_{y(0.2\%)}$	0.2% Offset Yield Strength	1160 MPa
% RA	% Reduction in Area	28
$\sigma_f$	True Fracture Strength	1850 MPa
$\epsilon_f$	True Fracture Strain	0.33
K	Strength Coefficient	1910 MPa
n	Strain Hardening Exponent	0.08
G	Shear Modulus	77.8 GPa

Axial Cyclic Properties

K'	Cyclic Strength Coefficient	1564 MPa
n'	Cyclic Strain Hardening Exponent	0.0681
$\sigma'_f$	Fatigue Strength Coefficient	3950 MPa
b	Fatigue Strength Exponent	-0.151
$\epsilon'_f$	Fatigue Ductility Coefficient	1.5
c	Fatigue Ductility Exponent	-0.761

Torsional Cyclic Properties

$K'_0$	Shear Strength Coefficient	860 MPa
$n'_0$	Shear Strain Hardening Exponent	0.079
$\tau'_f$	Shear Fatigue Strength Coefficient	2146 MPa
b	Shear Fatigue Strength Exponent	-0.148
$\gamma'_f$	Shear Fatigue Ductility Coefficient	18.0
c	Shear Fatigue Ductility Exponent	-0.922

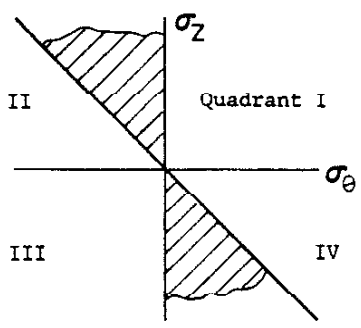
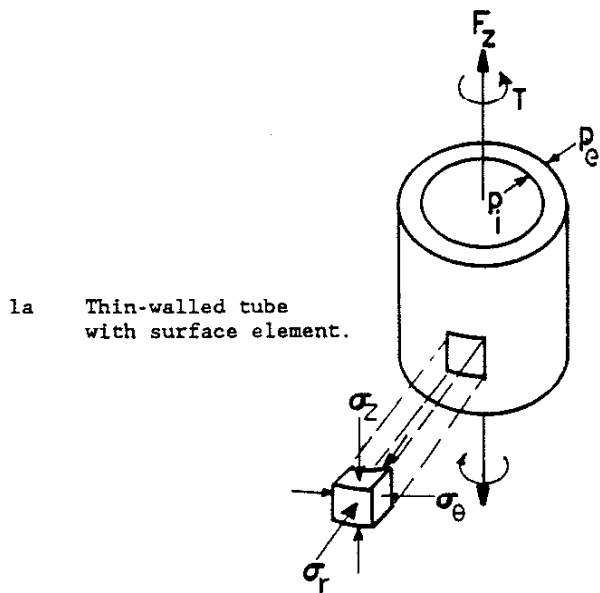
TABLE 3 Test Matrix

a) Biaxial Mean Stress Tests

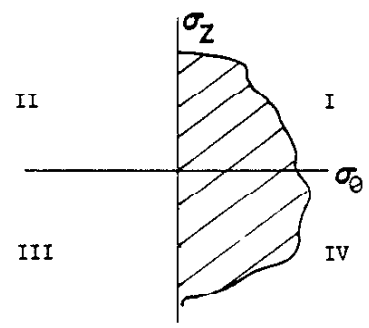
Constant Tangential Mean Stress		
	276 MPa (40 ksi)	517 MPa (75 ksi)
Axial Strain $\Delta\epsilon/2 = 0.005$ $R_\epsilon = -1$	Specimen INA13 $N_f = 7221$	Specimen INA4 $N_f = 3654$
	Specimen INA5 $N_f = 6735$	Specimen INA17 $N_f = 3293$
Axial Stress $\Delta\sigma/2 = 517$ MPa $R_\sigma = -1$	N/A	Specimen INA12 $N_f = 142061$
	N/A	Specimen INA23 $N_f = 165088$

b) Biaxial-Tension Test Matrix,  $\phi \approx +1$

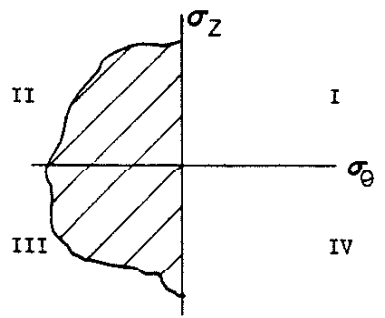
Expected Cycles to Failure			
	$5 \times 10^3$	$5 \times 10^4$	$5 \times 10^5$
Completely Reversed	Specimen INDM01 $R_\epsilon \approx -1$ $\Delta\epsilon/2 \approx 0.003$ $N_i \approx 1000$ $N_{1.0} > 2000$ $N_f = 3739$ $A_f = N/A$	Specimen INDM05 $R_\sigma \approx -1$ $\Delta\sigma/2 \approx 620$ MPa $N_i \approx 20000$ $N_{1.0} \approx 55414$ $N_f = 58084$ $A_f \approx 4.43$ mm	Specimen INDM03 $R_\sigma \approx -1$ $\Delta\sigma/2 \approx 517$ MPa $N_i \approx 38000$ $N_{1.0} \approx 120000$ $N_f = 126628$ $A_f \approx 6.4$ mm
	Released Tension	Specimen INDM07 $R_\epsilon \approx 0$ $\Delta\epsilon/2 \approx 0.0021$ $N_i \approx 6000$ $N_{1.0} > 19000$ $N_f = 20262$ $A_f \approx 5.13$ mm	Specimen INDM08 $R_\sigma \approx 0$ $\Delta\sigma/2 \approx 517$ MPa $N_i \approx 2150$ $N_{1.0} \approx 25000$ $N_f = 25656$ $A_f \approx 2.5$ mm
		Specimen INO1 $N_f = 30790$ $\Delta\sigma/2 \approx 517$ MPa	
		Specimen INO2 $N_f = 35910$ $\Delta\sigma/2 \approx 517$ MPa	



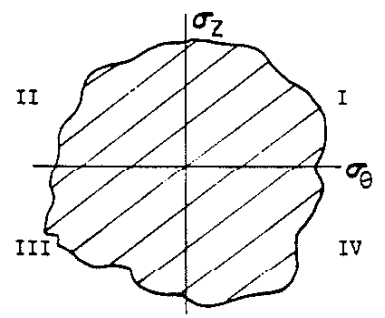
1b Tension/Compression plus Torsion



1c Internal Pressure plus Axial Tension/Compression



1d External Pressure plus Axial Tension/Compression



1e Internal plus External Pressure and Axial Tension/Compression

Figure 1. a) Thin-walled tube; b-e) possible loadings in two-dimensional stress space.

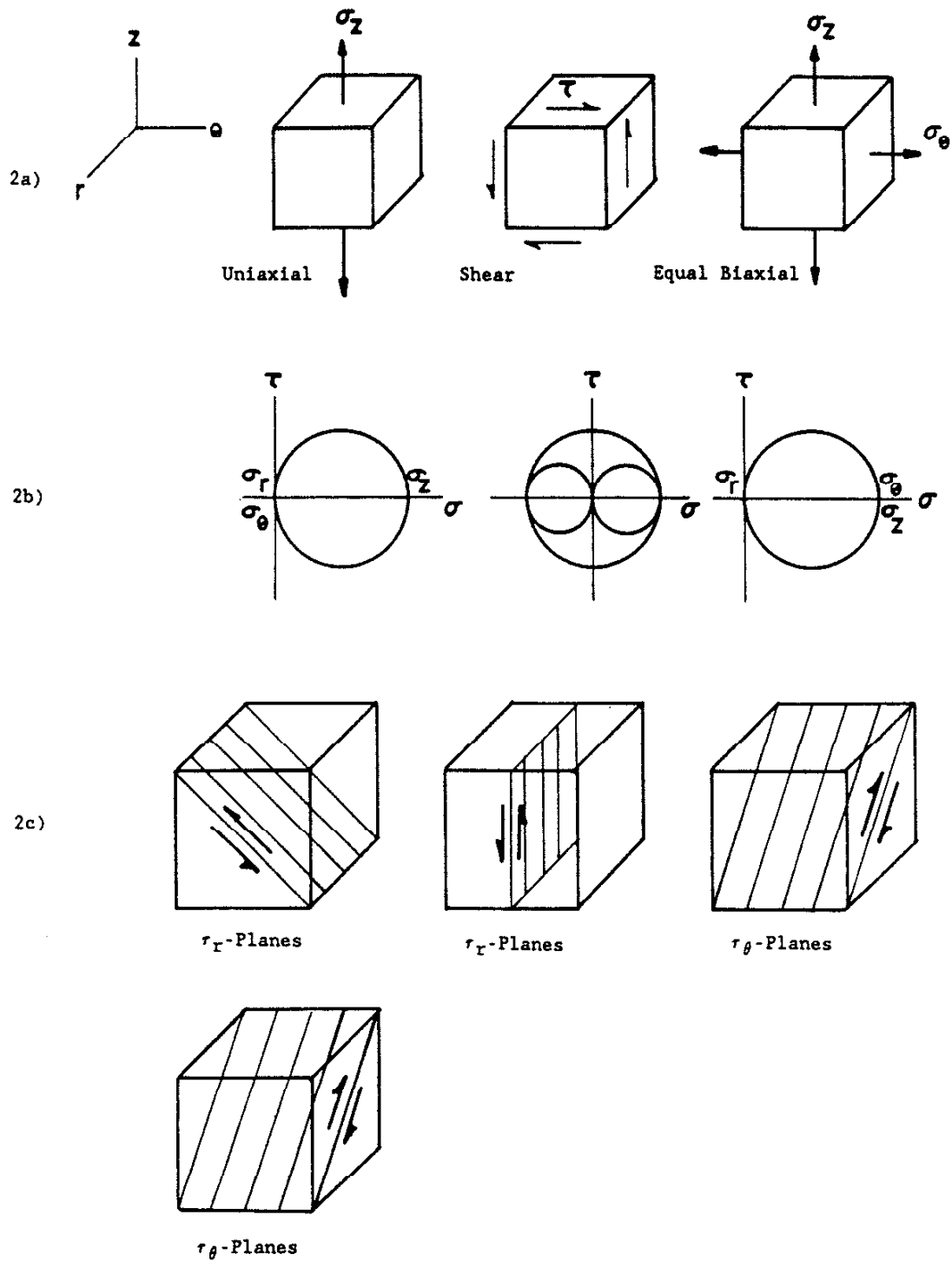


Figure 2. a) Surface elements in uniaxial tension, shear, and biaxial tension; b) Mohr's stress circles; c) resulting maximum principal shear planes.



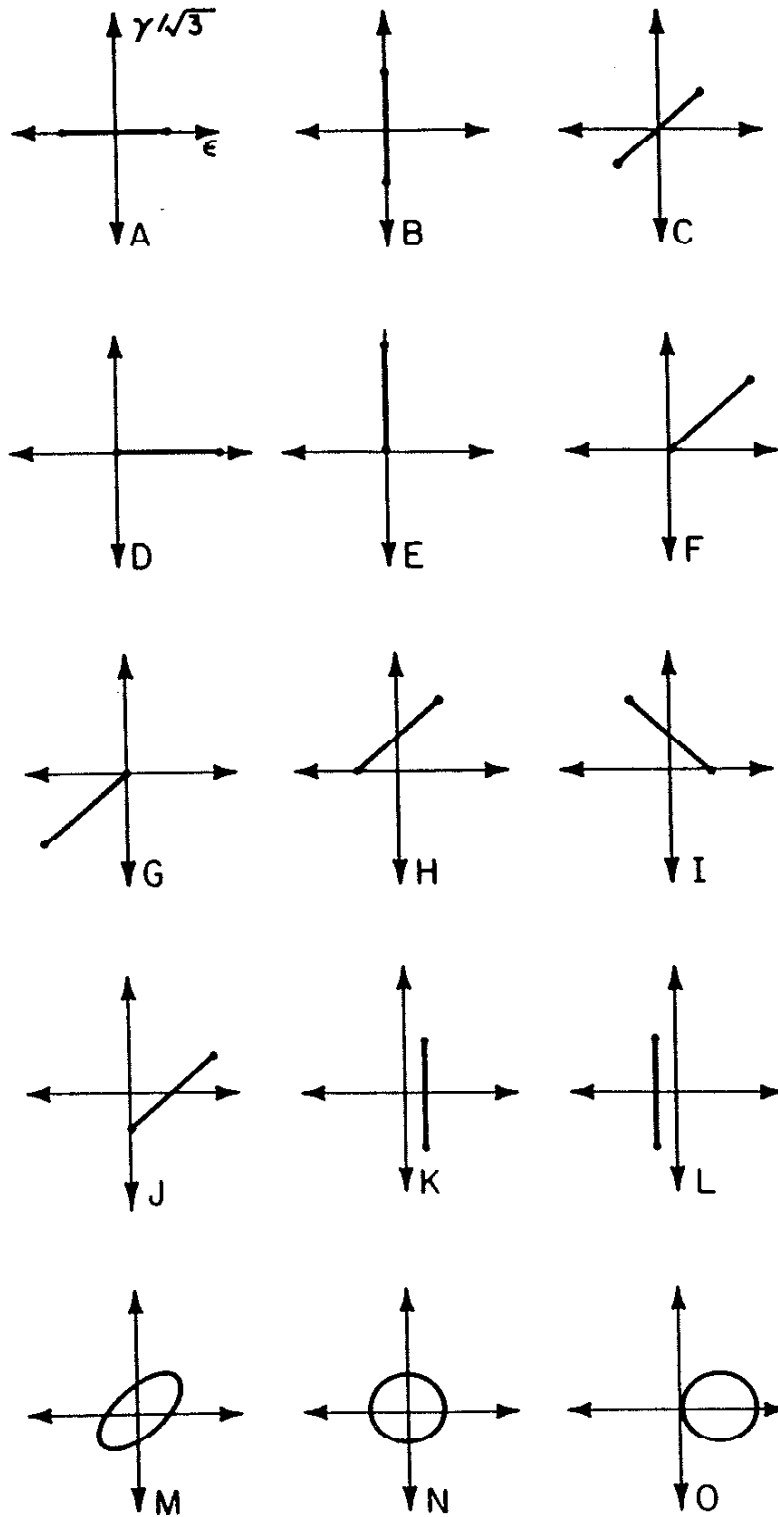


Figure 3. Biaxial strain paths.

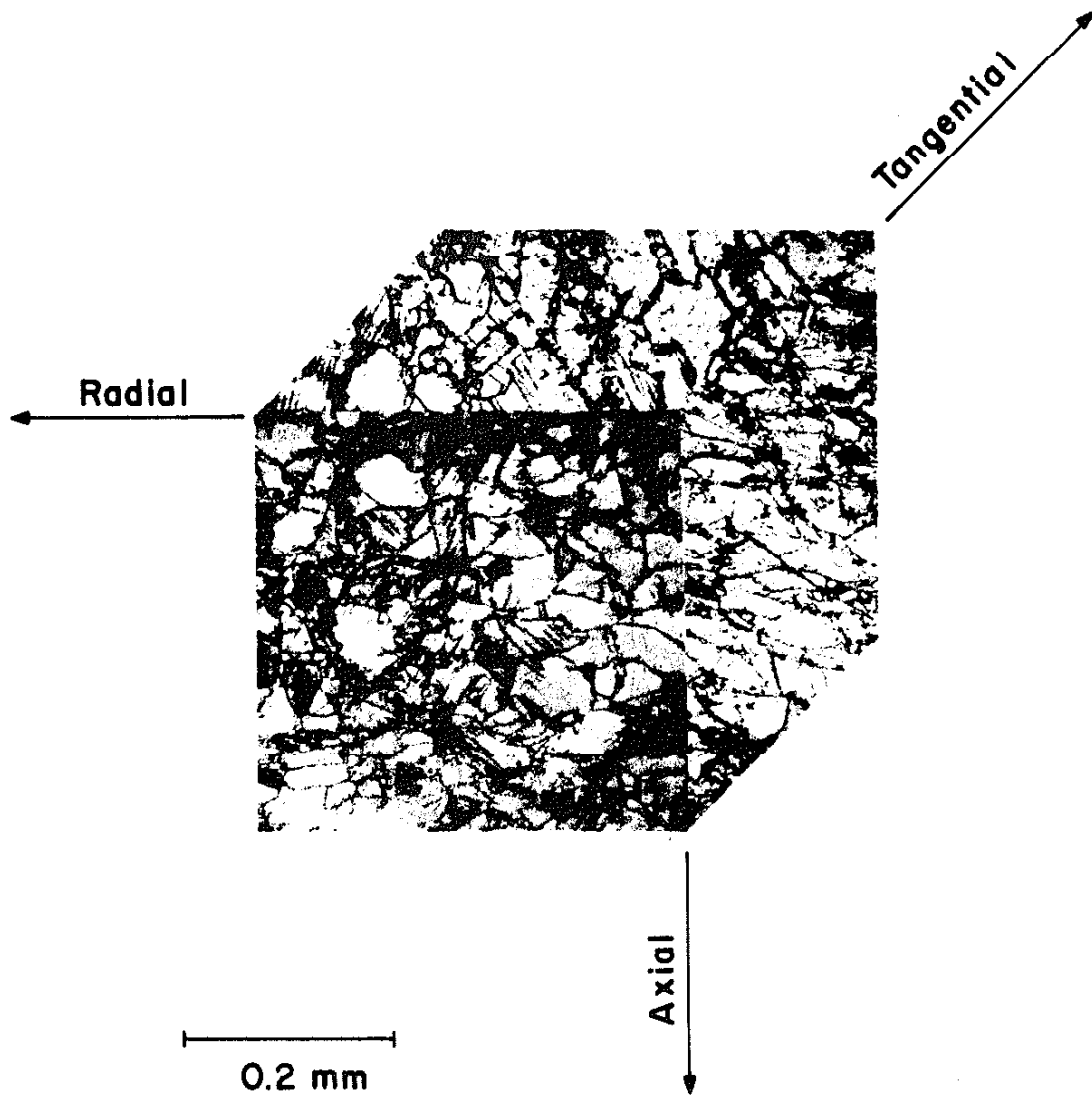


Figure 4. Etched microstructure.

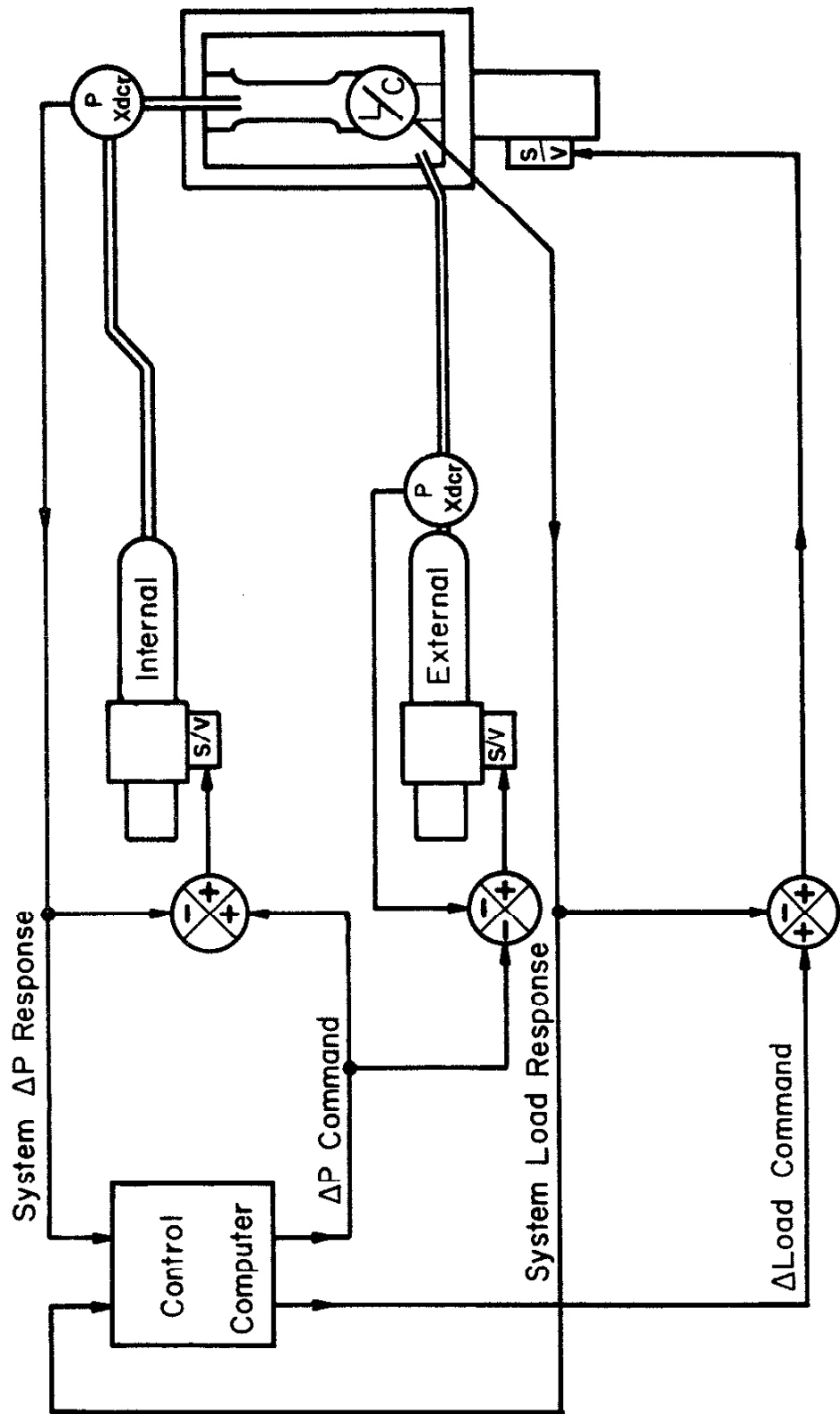


Figure 5. Schematic of test system controls.

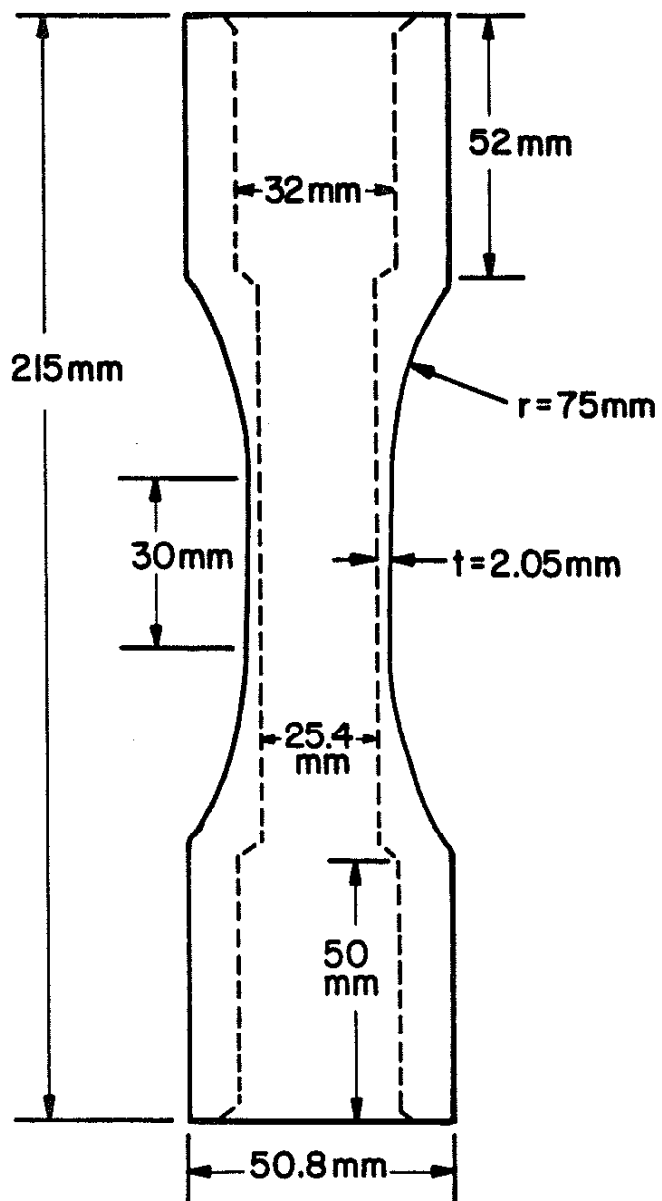


Figure 6. Single reduced specimen dimensions.

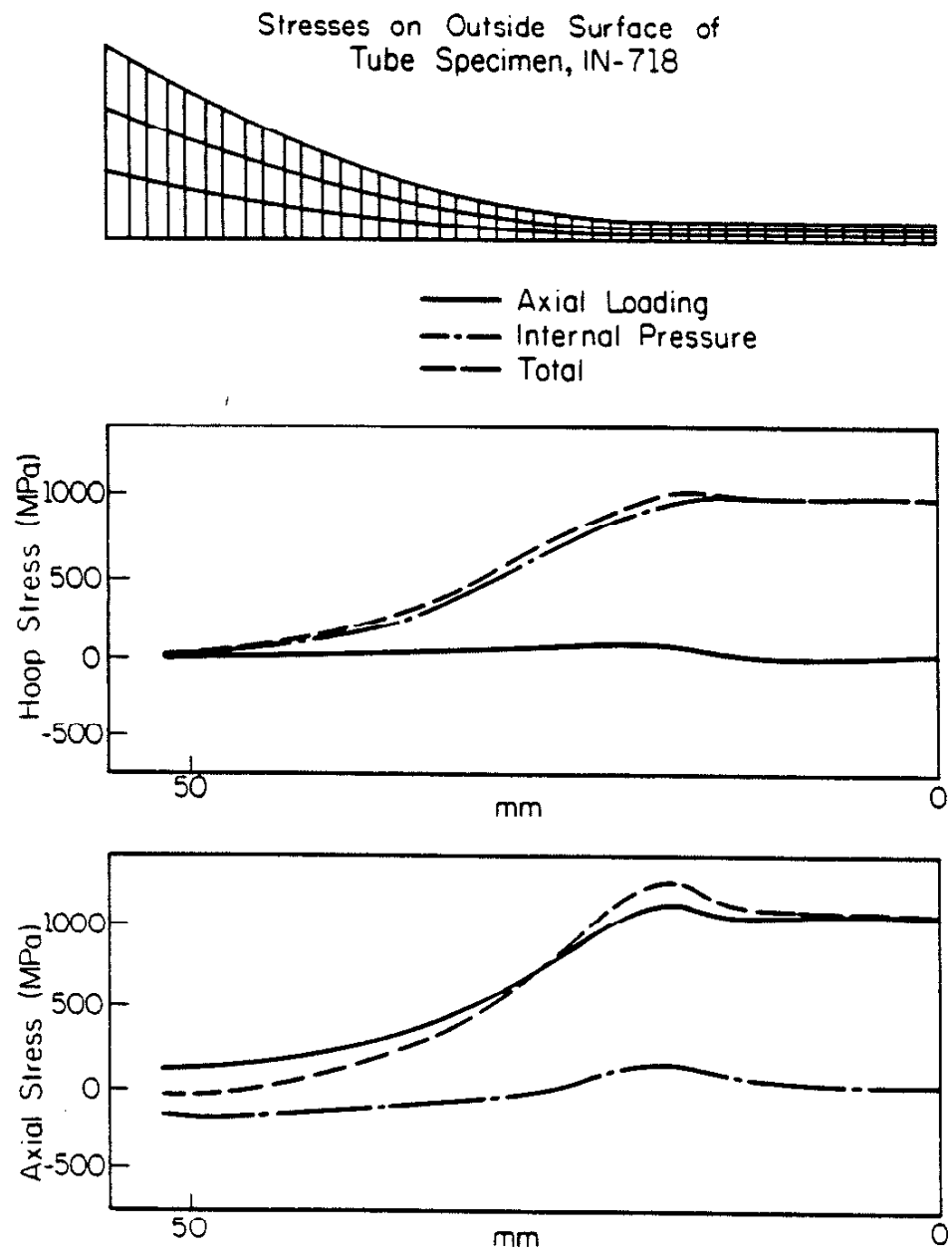


Figure 7. Stress distribution from Finite Element Method for single reduced specimen.

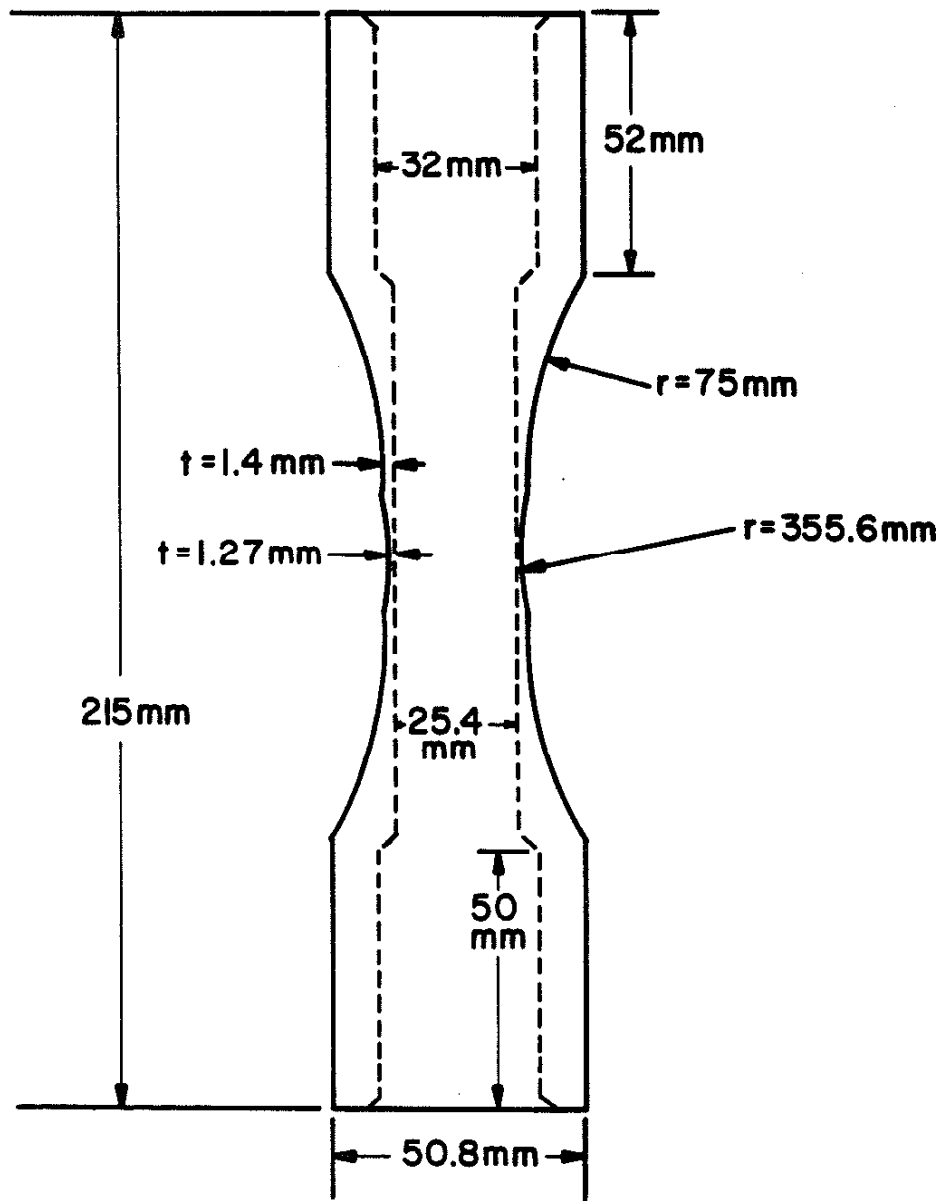
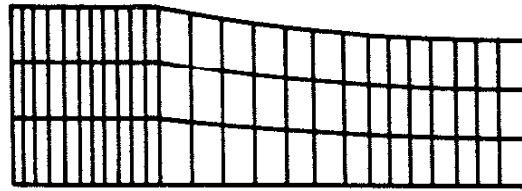


Figure 8. Double reduced specimen dimensions.

# STRESS DISTRIBUTION IN CENTER SECTION OF DOUBLE REDUCED SPECIMEN



- $\sigma_\theta$  Inside Surface
- $\sigma_z$  Inside Surface
- $\sigma_\theta$  Outside Surface
- - -  $\sigma_z$  Outside Surface

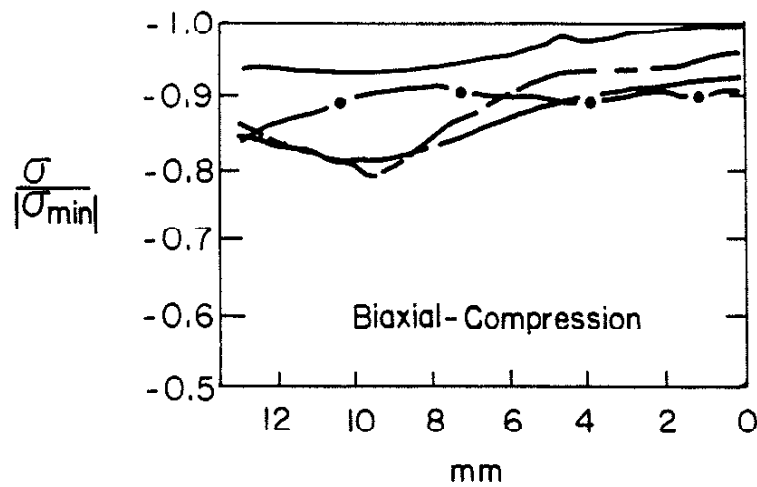
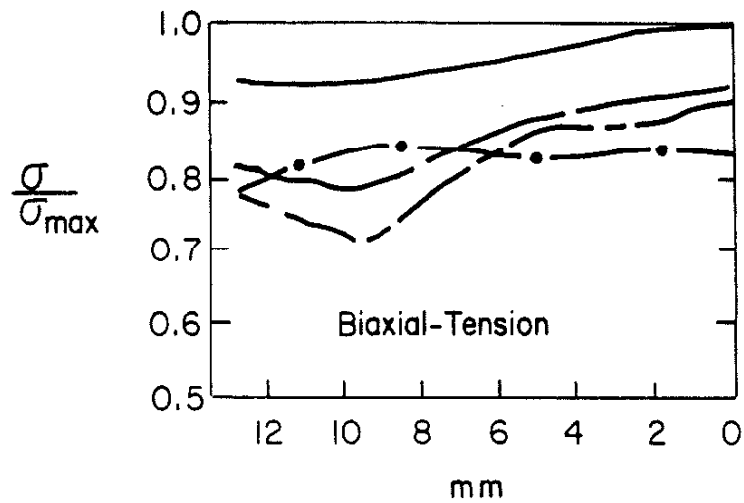


Figure 9. Stress distribution from Finite Element Method for double reduced specimen.

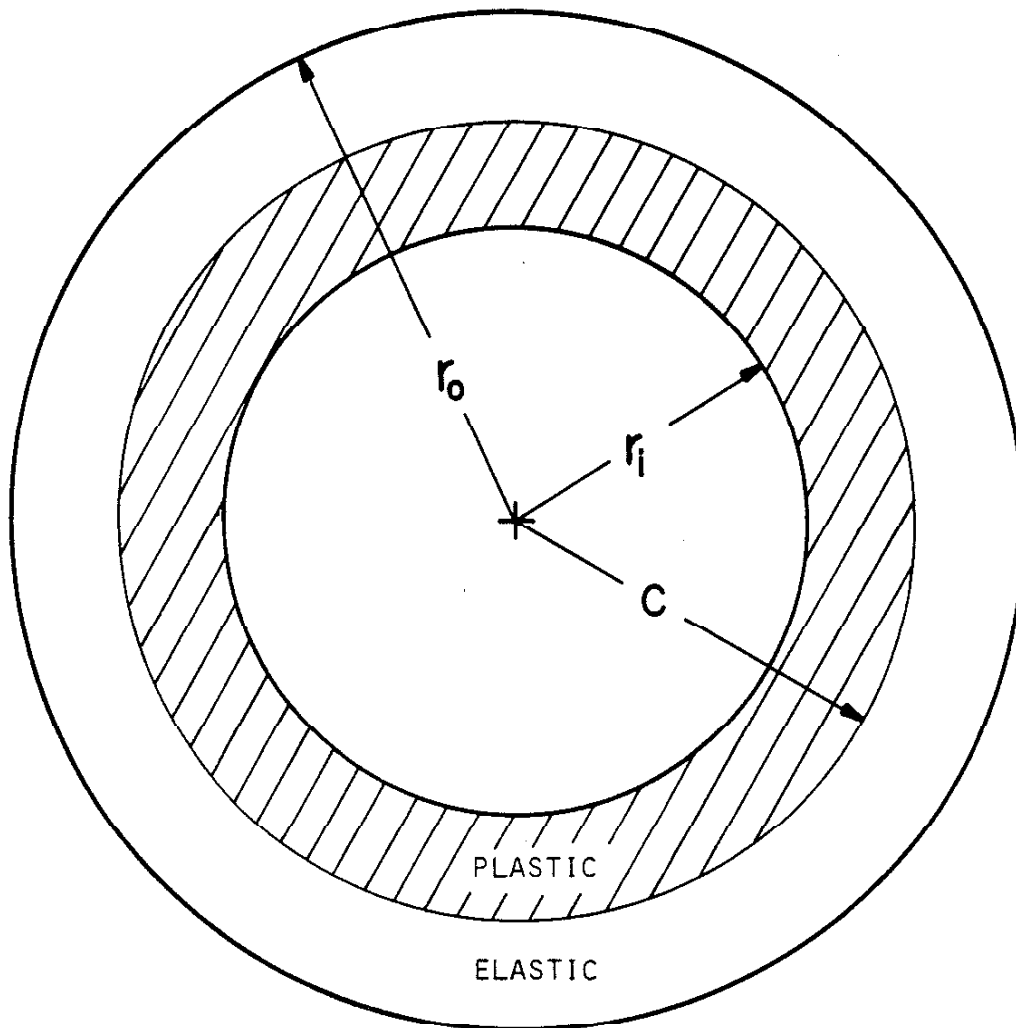


Figure 10. Plastic zone definition for an elastic-plastic tube.



DIAMETRAL RESIDUAL STRESSES RESULTING FROM PARTIAL OR FULLY PLASTIC YIELDING OF TUBULAR SPECIMEN

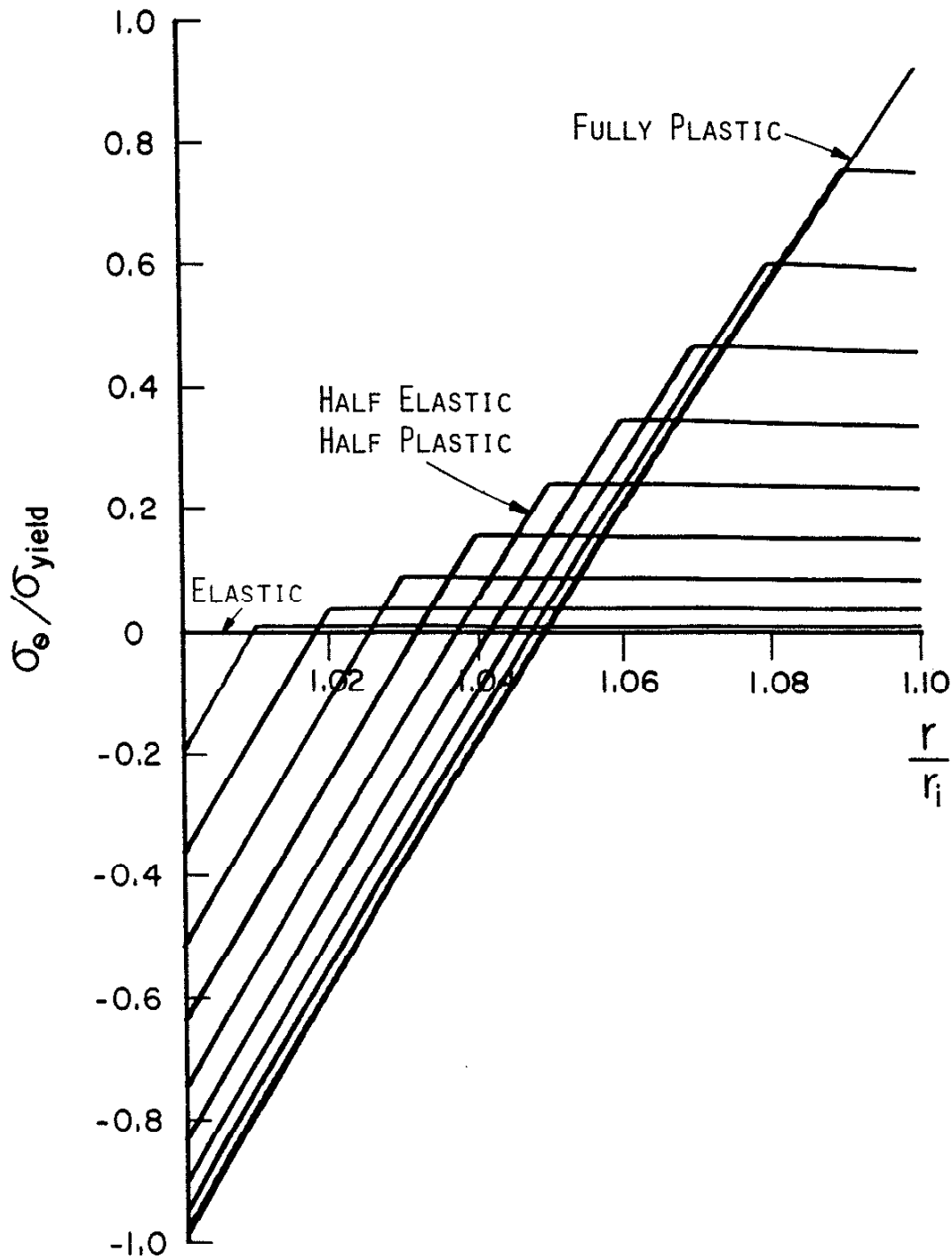


Figure 11.  $\sigma_\theta$  residual stresses from single overload.

AXIAL RESIDUAL STRESSES RESULTING FROM PARTIAL  
OR FULLY PLASTIC YIELDING OF TUBULAR SPECIMEN

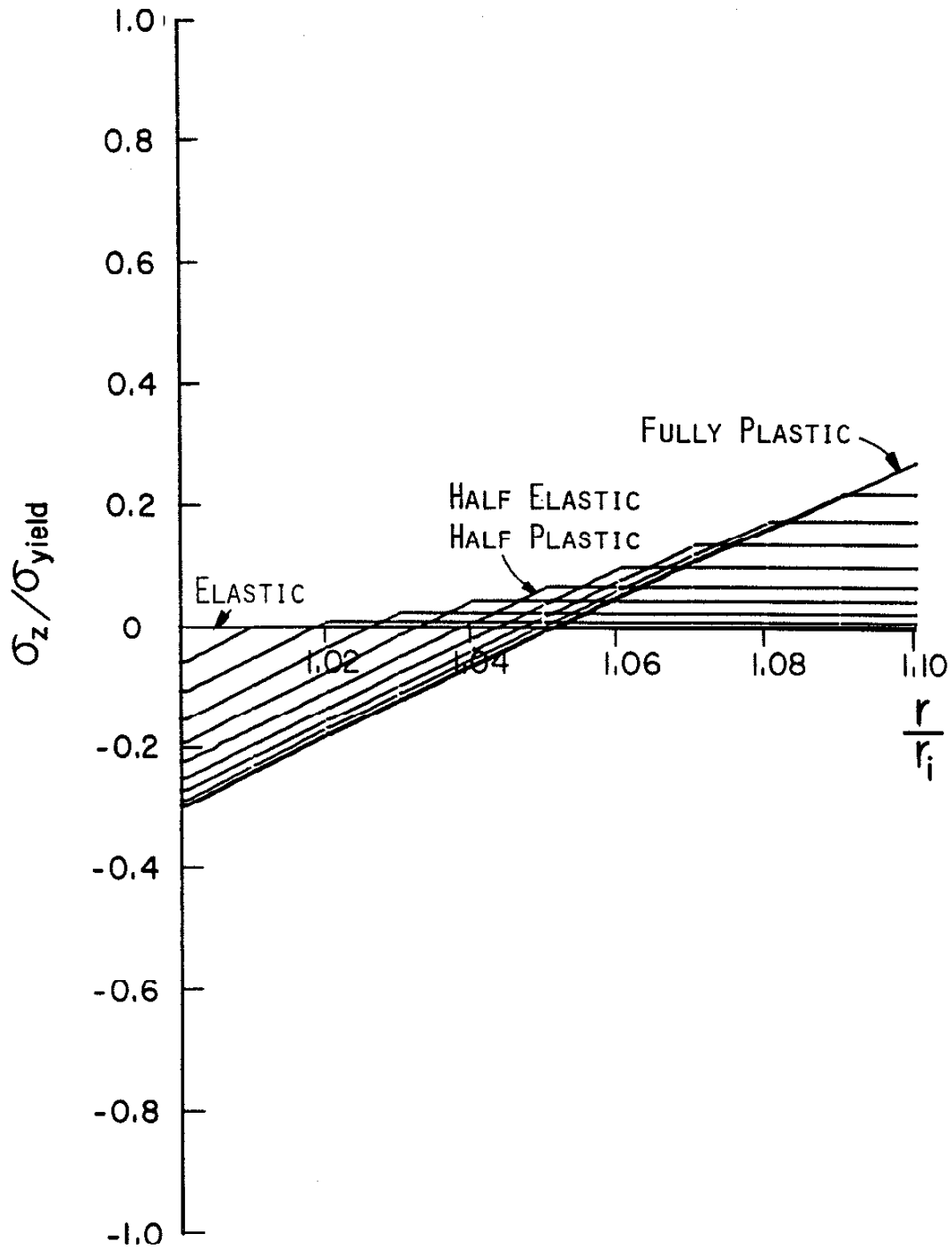


Figure 12.  $\sigma_z$  residual stresses from single overload.

**SPECIMEN INDMOI**

**CONTROL MODE, STRAIN(200cycles), LOAD(remainder)**

**TEST LEVELS, Maximum  $\epsilon_z=0.00332$ ,  $\epsilon_\theta=0.00312$**

**Minimum  $\epsilon_z=-0.00336$ ,  $\epsilon_\theta=-0.00318$**

**INITIATION LIFE,  $N_i = N/A$**

**Imm CRACK LIFE,  $N_{i,0} = N/A$**

**FAILURE LIFE,  $N_f = 3739$**

**FINAL CRACK LENGTH,  $A_f = N/A$**

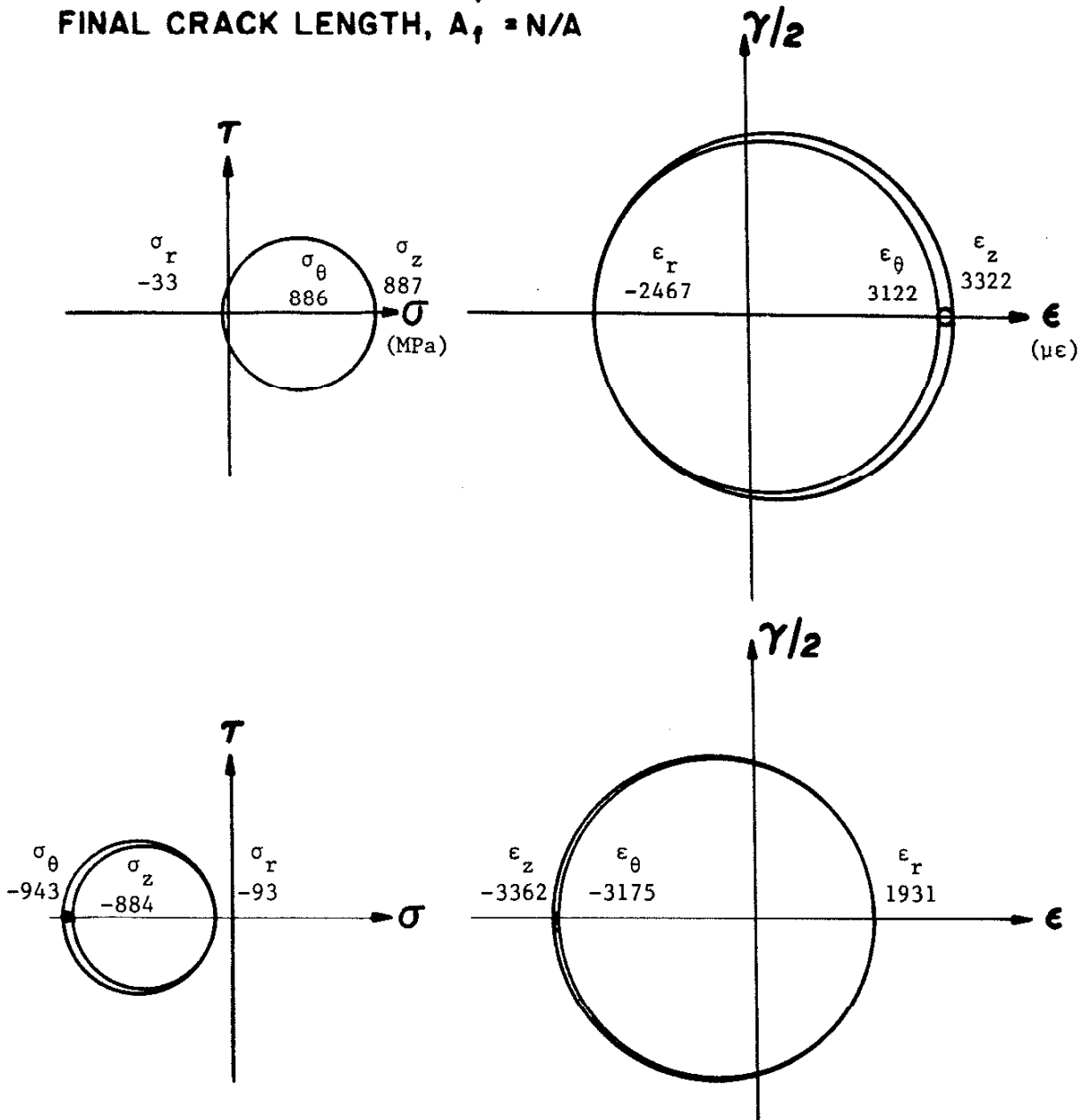
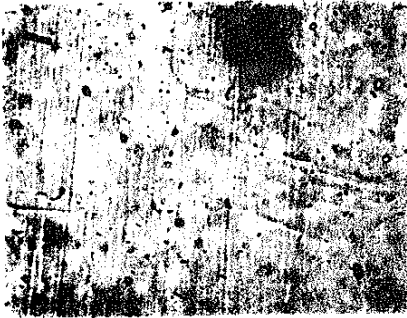
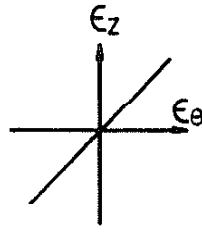


Figure 13. Test details and Mohr's circles for INDMOI on outer surface.

INDM01,  $N_f = 3739$

$R_\epsilon \approx -1$ ,  $\phi \approx +1$ ,  $\Delta\epsilon/2 \approx 0.003$



0.1mm  
N=2000



0.5mm  
N=3739

SPECIMEN  
AXIS

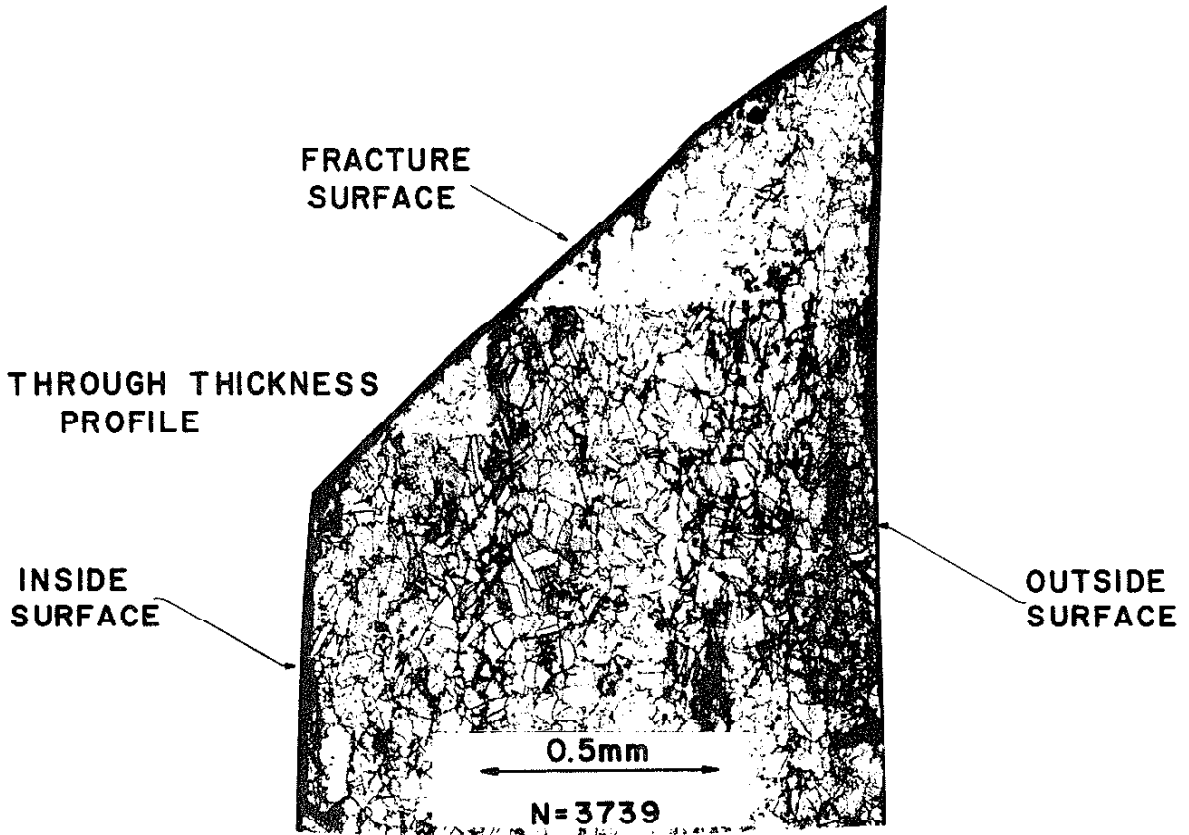


Figure 14. Cracking details for INDM01.

**SPECIMEN INDM05**

**CONTROL MODE, LOAD/PRESSURE**

**TEST LEVELS, Maximum  $\sigma_z = 625 \text{ MPa}$ ,  $\sigma_\theta = 638 \text{ MPa}$**   
**Minimum  $\sigma_z = -663 \text{ MPa}$ ,  $\sigma_\theta = -638 \text{ MPa}$**

**INITIATION LIFE,  $N_i = 20\,000$**

**Imm CRACK LIFE,  $N_{i,0} = 55\,414$**

**FAILURE LIFE,  $N_f = 58\,084$**

**FINAL CRACK LENGTH,  $A_f = 4.43 \text{ mm}$**

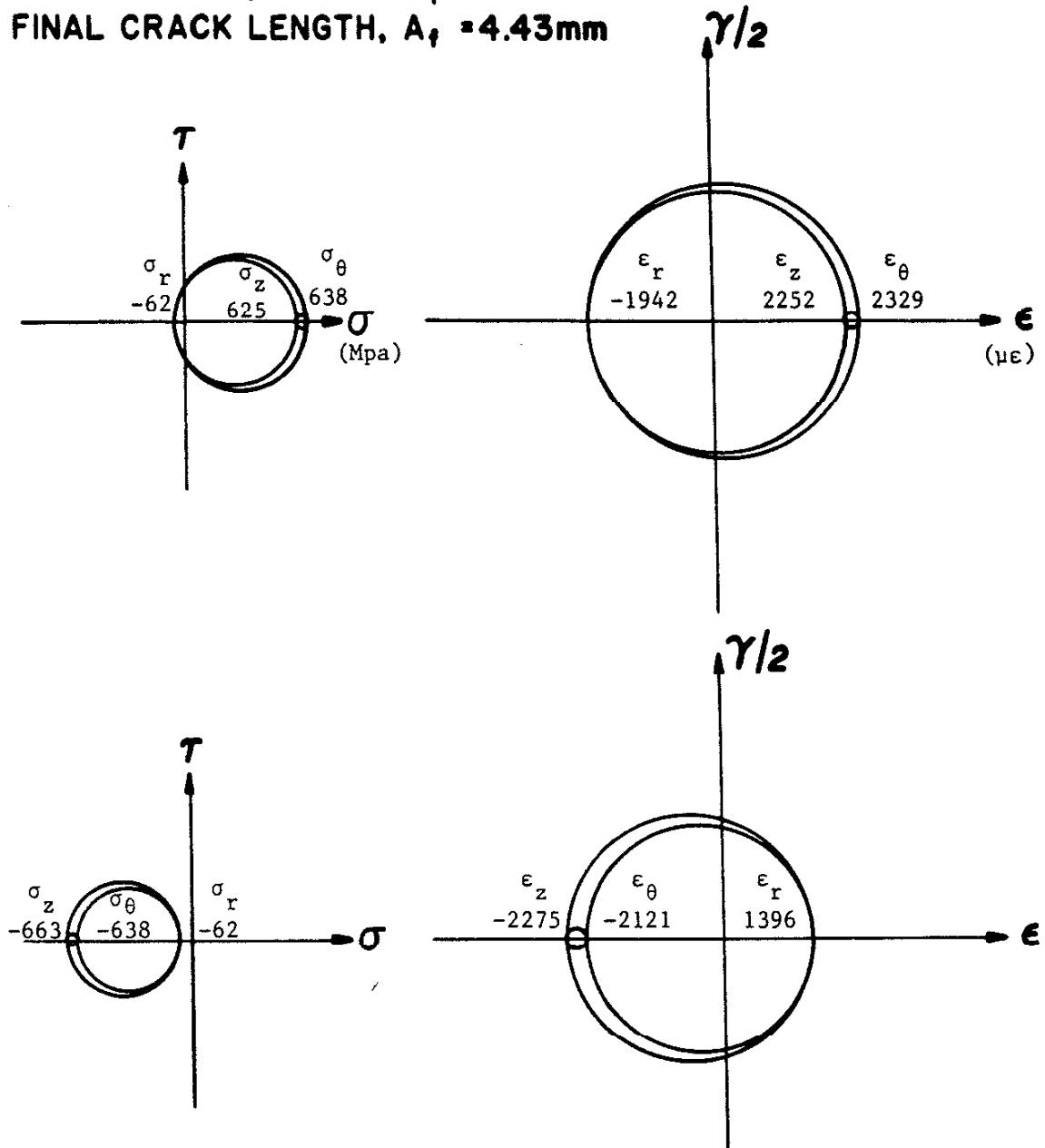
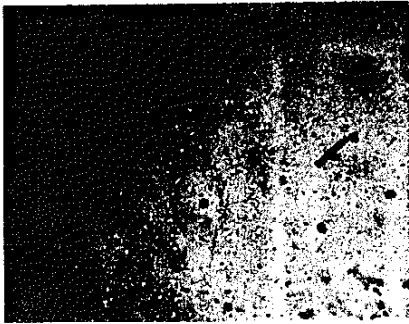
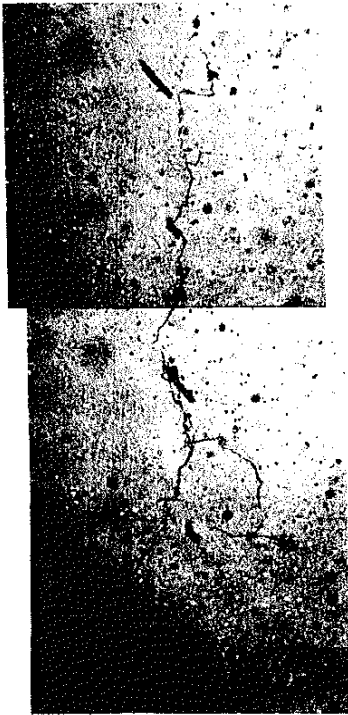
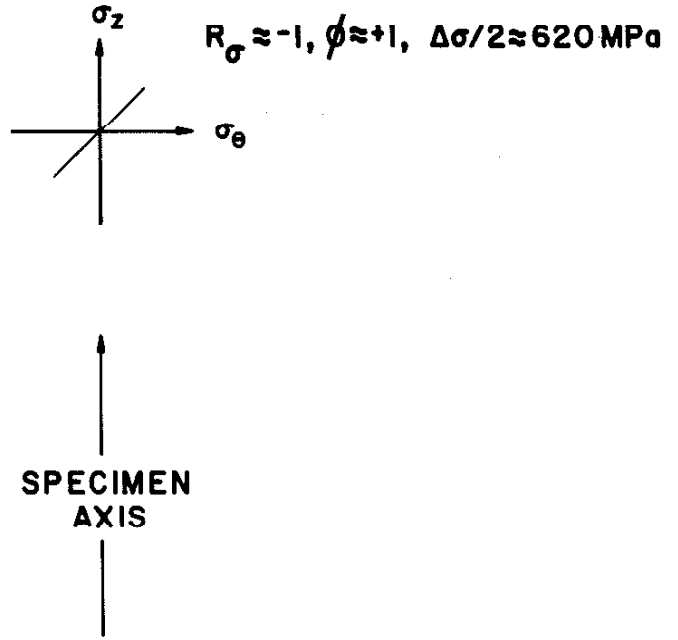


Figure 15. Test details and Mohr's circles for INDM05 on outer surface.

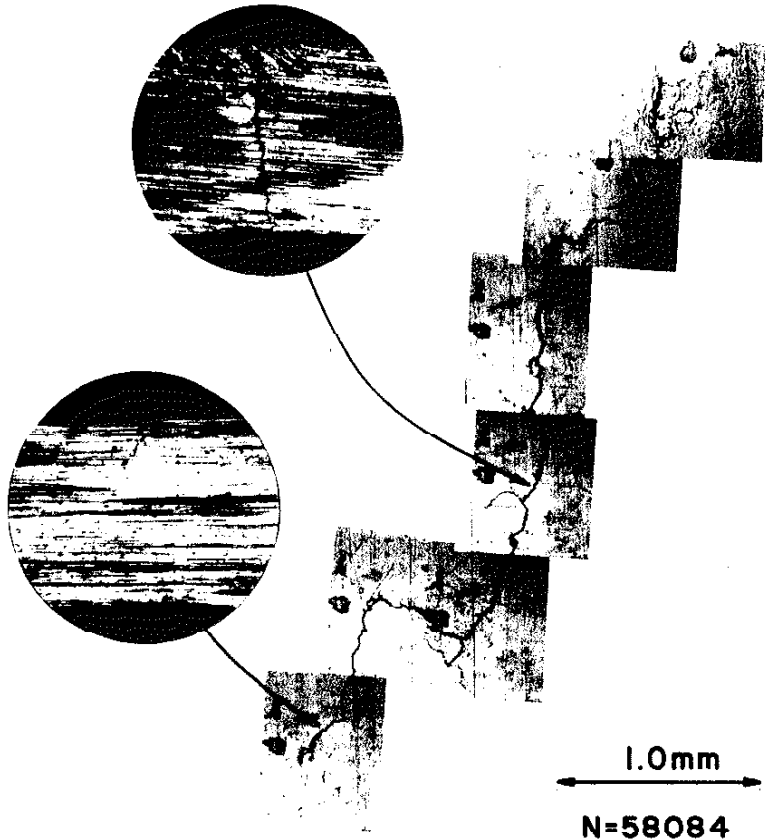
INDM05,  $N_f = 58084$



0.5mm  
N=46000



0.5mm  
N=55414



1.0mm  
N=58084

Figure 16. Cracking details for INDM05.

**SPECIMEN INDM03**

**CONTROL MODE LOAD/PRESSURE**

TEST LEVELS, Maximum  $\sigma_z = 541 \text{ MPa}$ ,  $\sigma_\theta = 532 \text{ MPa}$   
 Minimum  $\sigma_z = -541 \text{ MPa}$ ,  $\sigma_\theta = 532 \text{ MPa}$

INITIATION LIFE,  $N_i = 38\ 000$

Imm CRACK LIFE,  $N_{i,0} = 120\ 000$

FAILURE LIFE,  $N_f = 126\ 628$

FINAL CRACK LENGTH,  $A_f = 6.4 \text{ mm}$

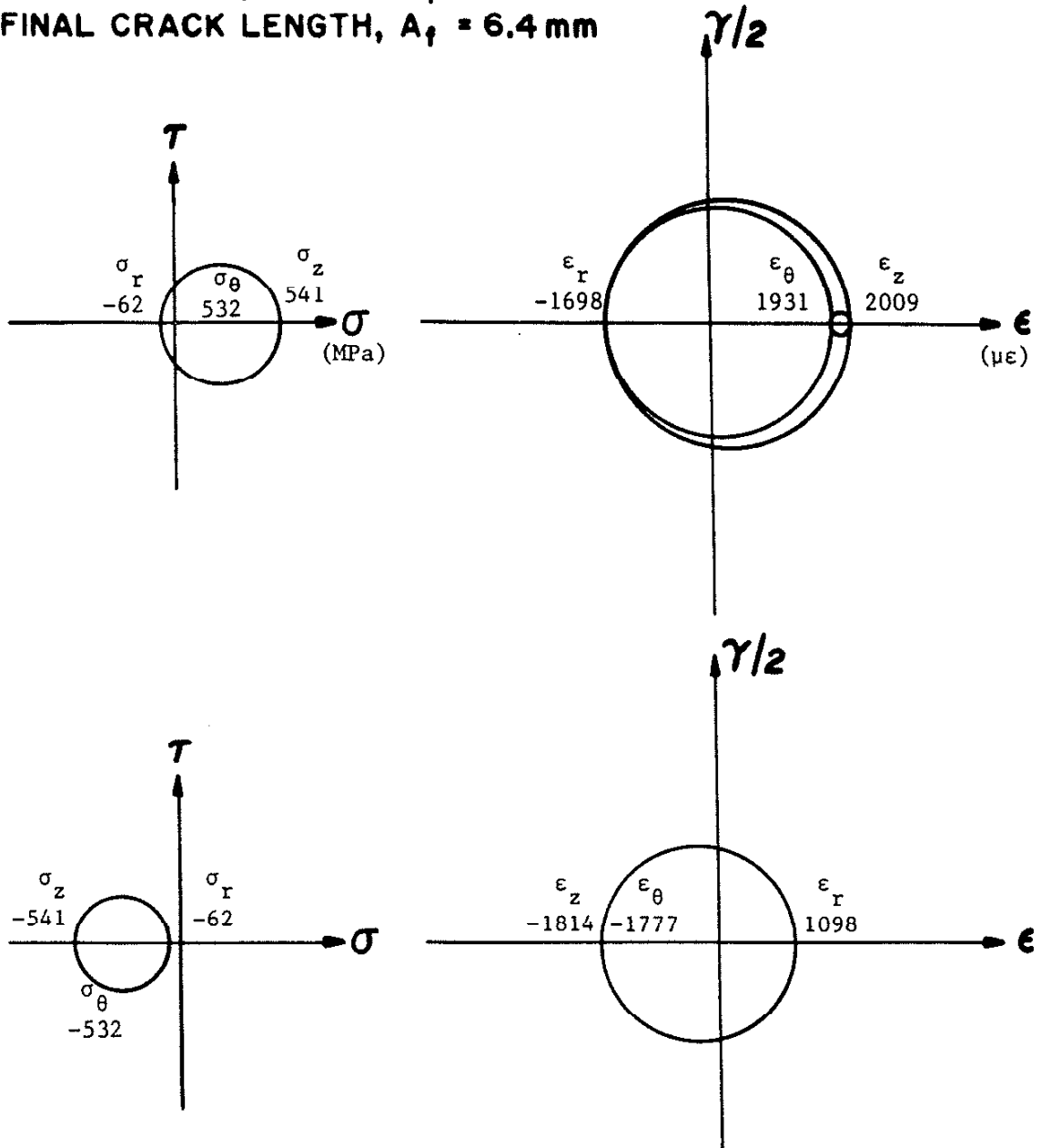
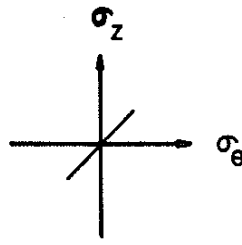


Figure 17. Test details and Mohr's circles for INDM03 on outer surface.

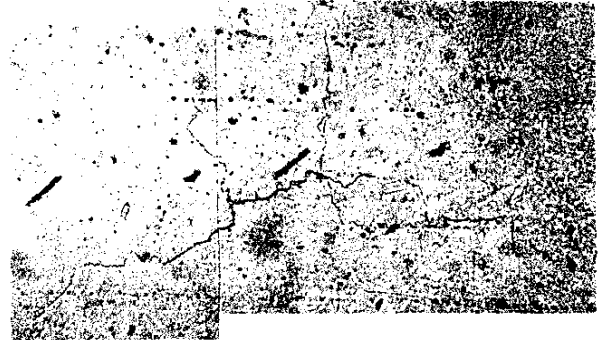
INDM03,  $N_f=126628$

$R_\sigma \approx -1$ ,  $\phi \approx +1$ ,  $\Delta\sigma/2 \approx 517\text{MPa}$

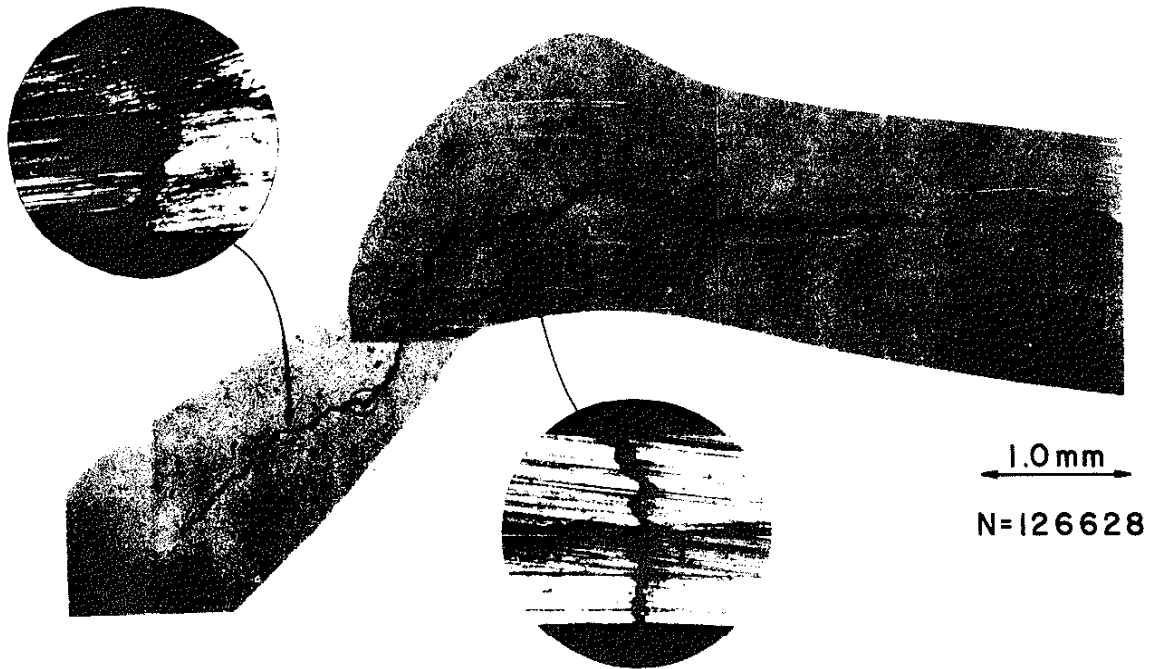


0.5mm  
N=110000

SPECIMEN  
AXIS



0.5mm  
N=120000



1.0mm  
N=126628

Figure 18. Cracking details for INDM03, Failure crack.



INDM03,  $N_f=126628$

$R_\sigma \approx -1$ ,  $\phi \approx +1$ ,  $\Delta\sigma/2 \approx 517 \text{ MPa}$

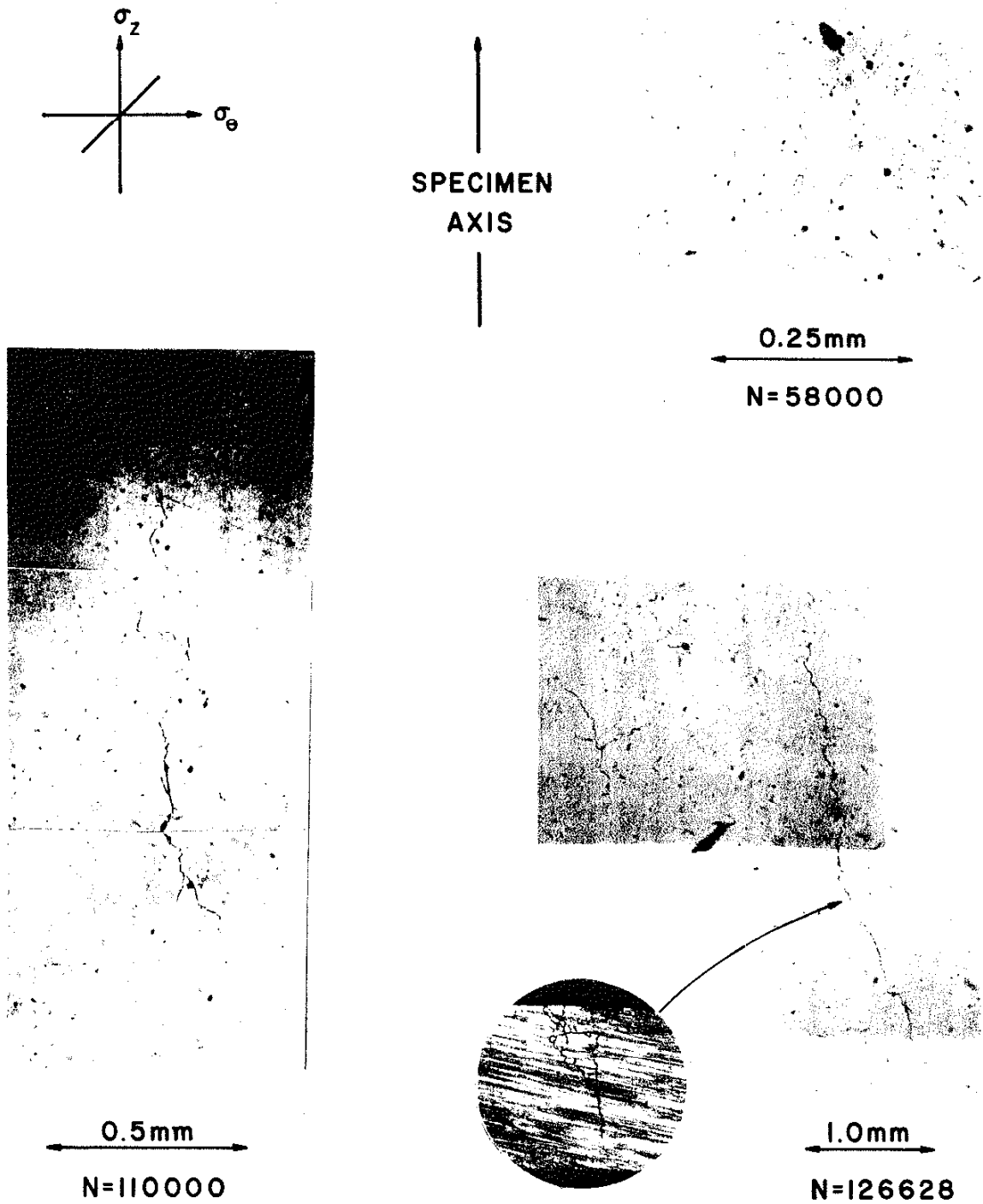


Figure 19. Cracking details for INDM03, Non-failure crack.

INDM03,  $N_f=126628$

$R_\sigma \approx -1$ ,  $\phi \approx +1$ ,  $\Delta\sigma/2 \approx 517\text{MPa}$

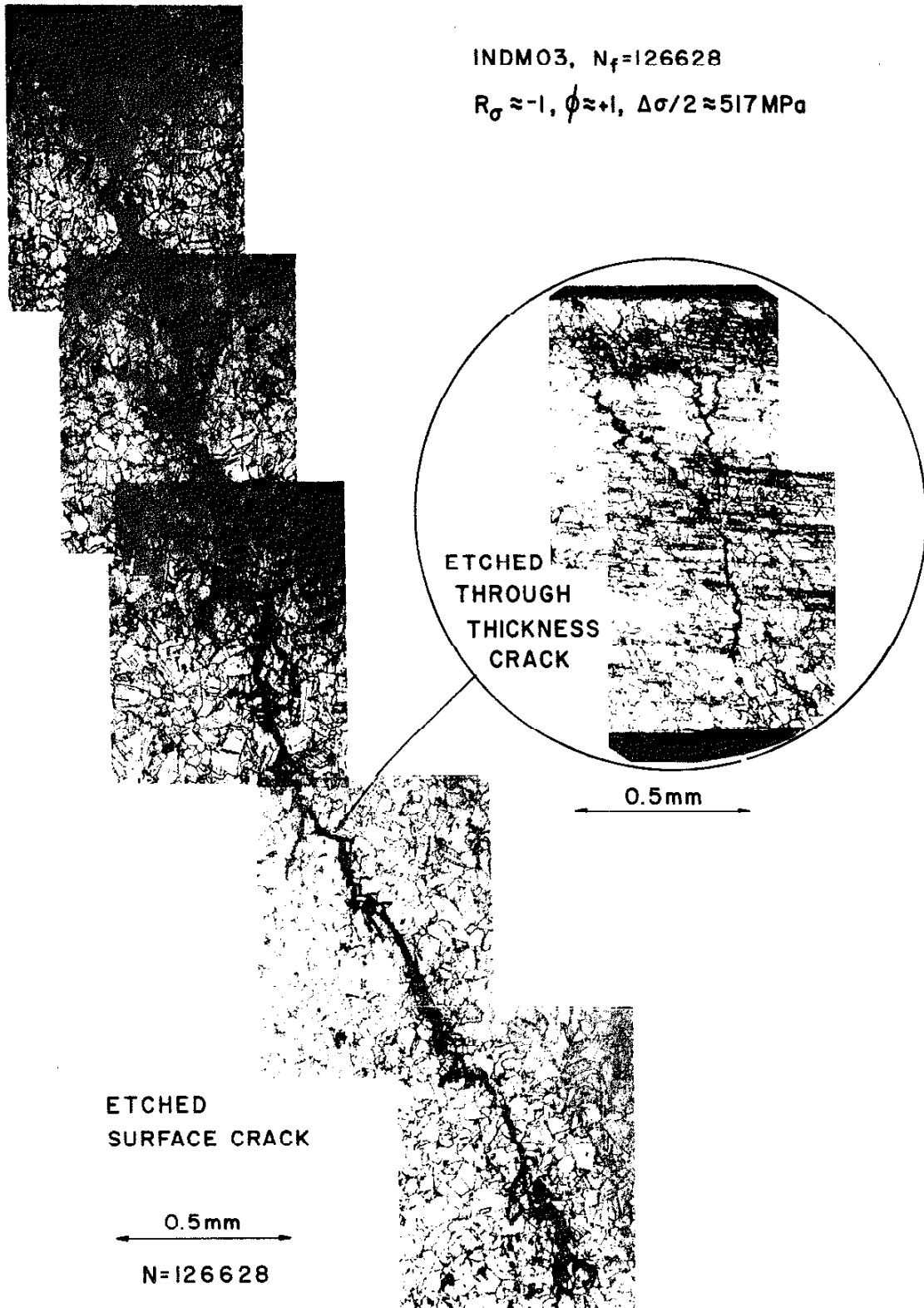


Figure 20. Cracking details for INDM03, Non-failure crack etched.

**SPECIMEN INDM07**

**CONTROL MODE, STRAIN**

TEST LEVELS, Maximum  $\epsilon_z = 0.00416$ ,  $\epsilon_\theta = 0.00454$   
 Minimum  $\epsilon_z = 0$ ,  $\epsilon_\theta = -0.00065$

INITIATION LIFE,  $N_i = 6000$

Imm CRACK LIFE,  $N_{i,0} = 19000$

FAILURE LIFE,  $N_f = 20262$

FINAL CRACK LENGTH,  $A_f = 5.13\text{ mm}$

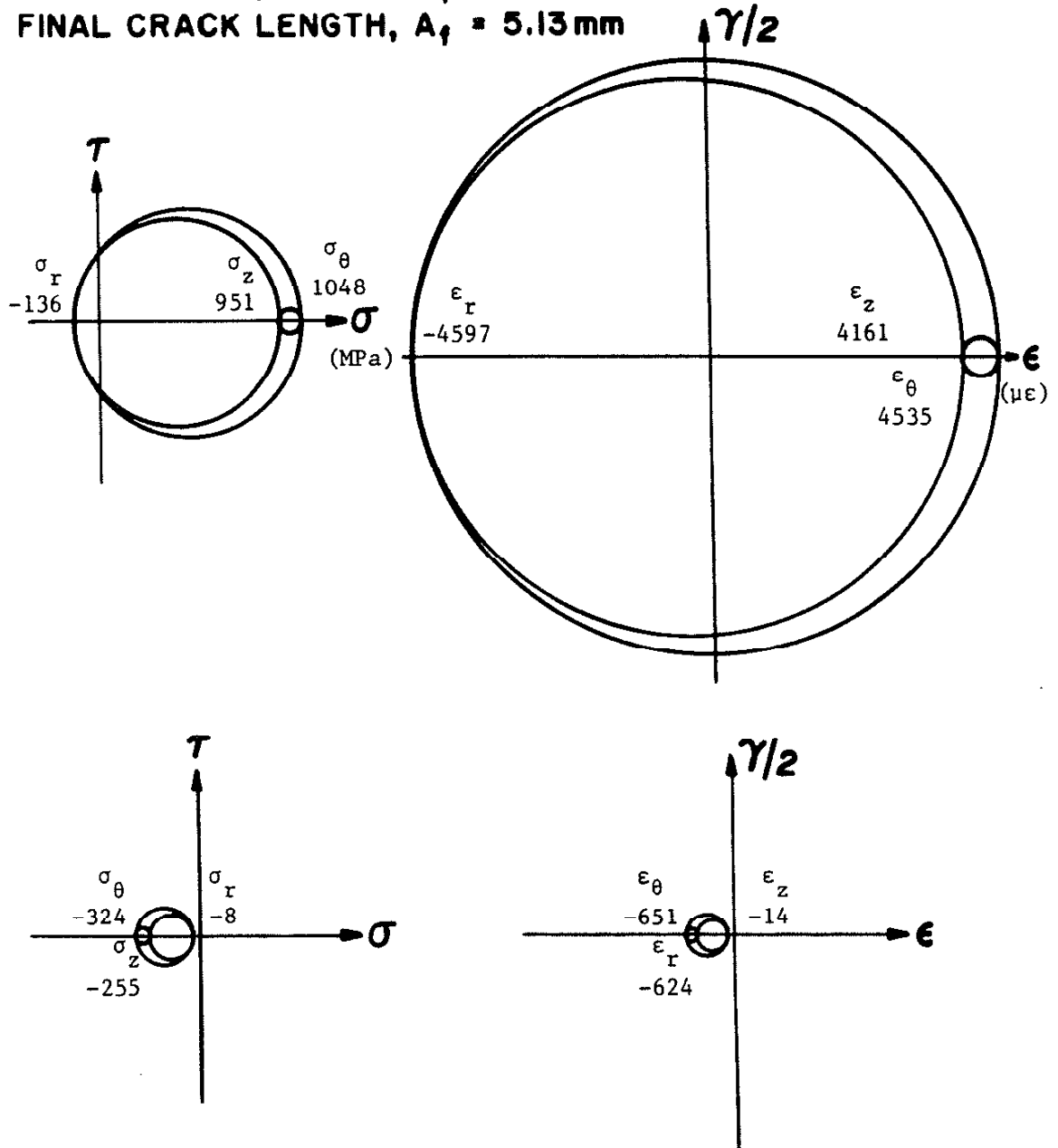


Figure 21. Test details and Mohr's circles for INDM07 on inner surface.

INDM07,  $N_f = 20262$

$R_\epsilon = 0$ ,  $\phi = +1$ ,  $\Delta\epsilon = 0.0042$

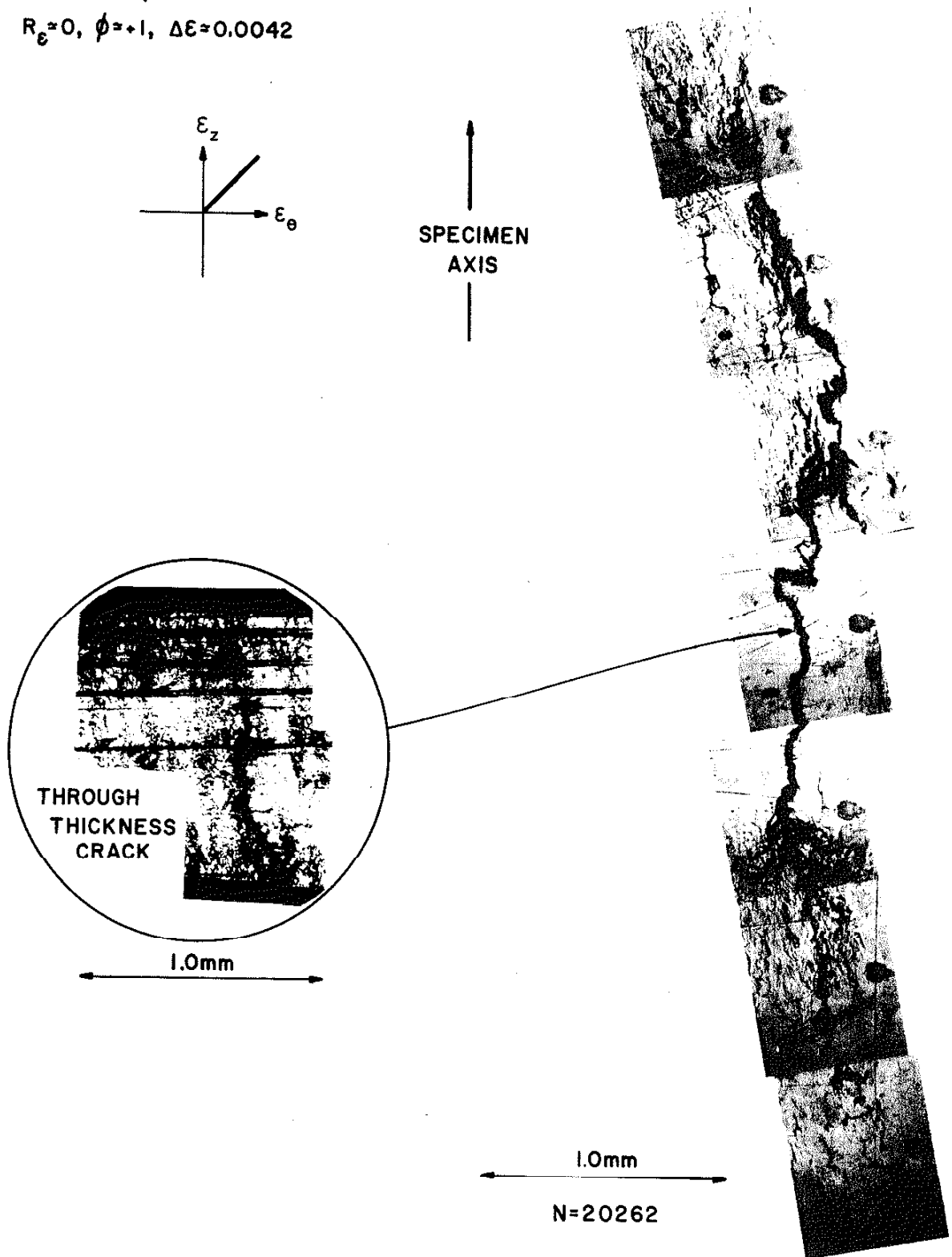


Figure 22. Cracking details for INDM07.

### INDM07, Outer Surface Diametral Response

Setup Cycle, Loading Path ① → ② → ③

Released Tension Cycles, Loading Path ③ → ④ → ③

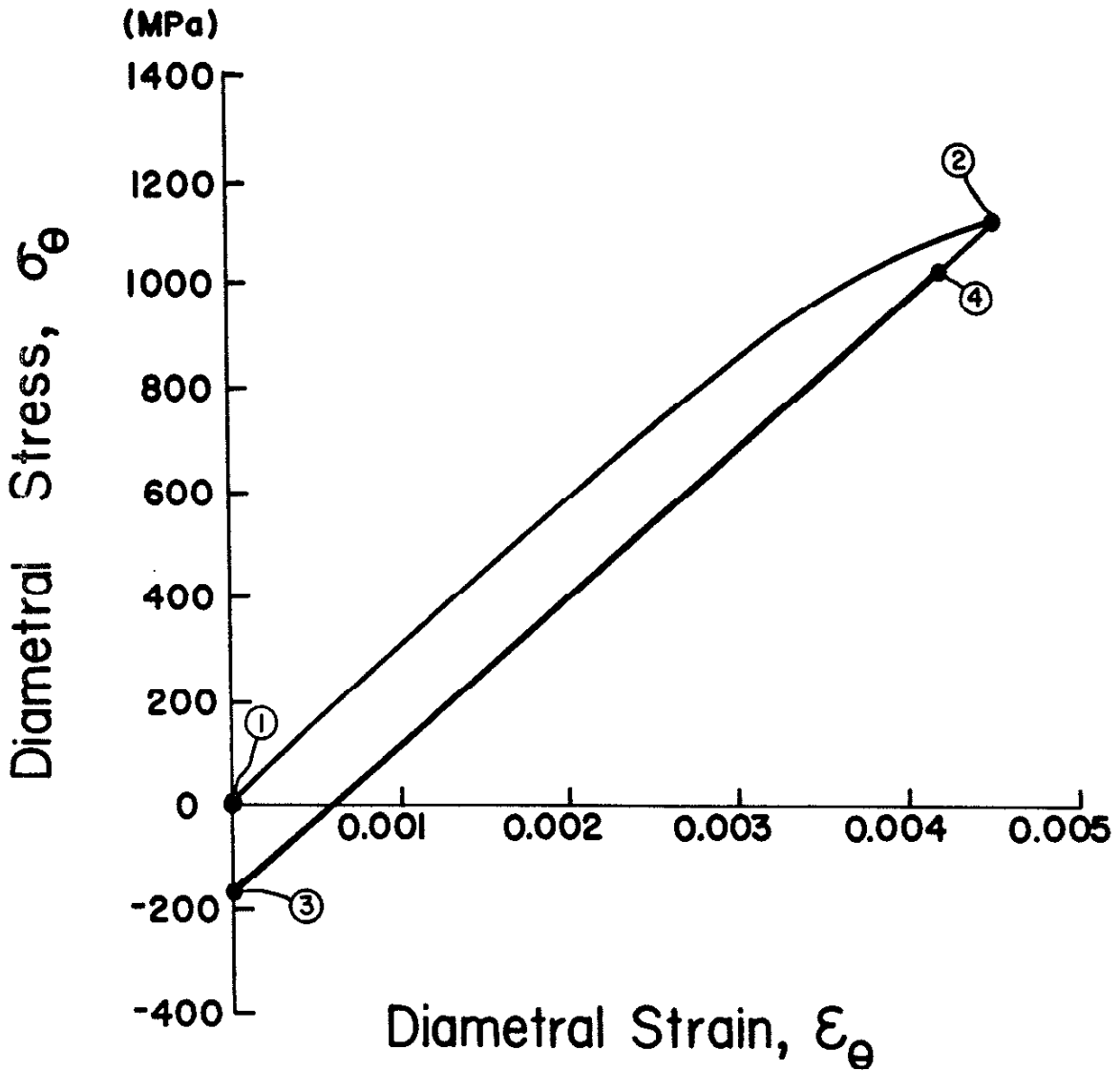


Figure 23. Diametral stress-strain loop, setup cycle for INDM07.

**SPECIMEN INDM08**

**CONTROL MODE, LOAD/PRESSURE**

**TEST LEVELS, Maximum  $\sigma_z = 972$  MPa,  $\sigma_\theta = 1062$  MPa**  
**Minimum  $\sigma_z = -28$  MPa,  $\sigma_\theta = -94$  MPa**

**INITIATION LIFE,  $N_i = 2150$**

**Imm CRACK LIFE,  $N_{i,0} = 25\ 000$**

**FAILURE LIFE,  $N_f = 25\ 656$**

**FINAL CRACK LENGTH,  $A_f = 2.5$  mm**

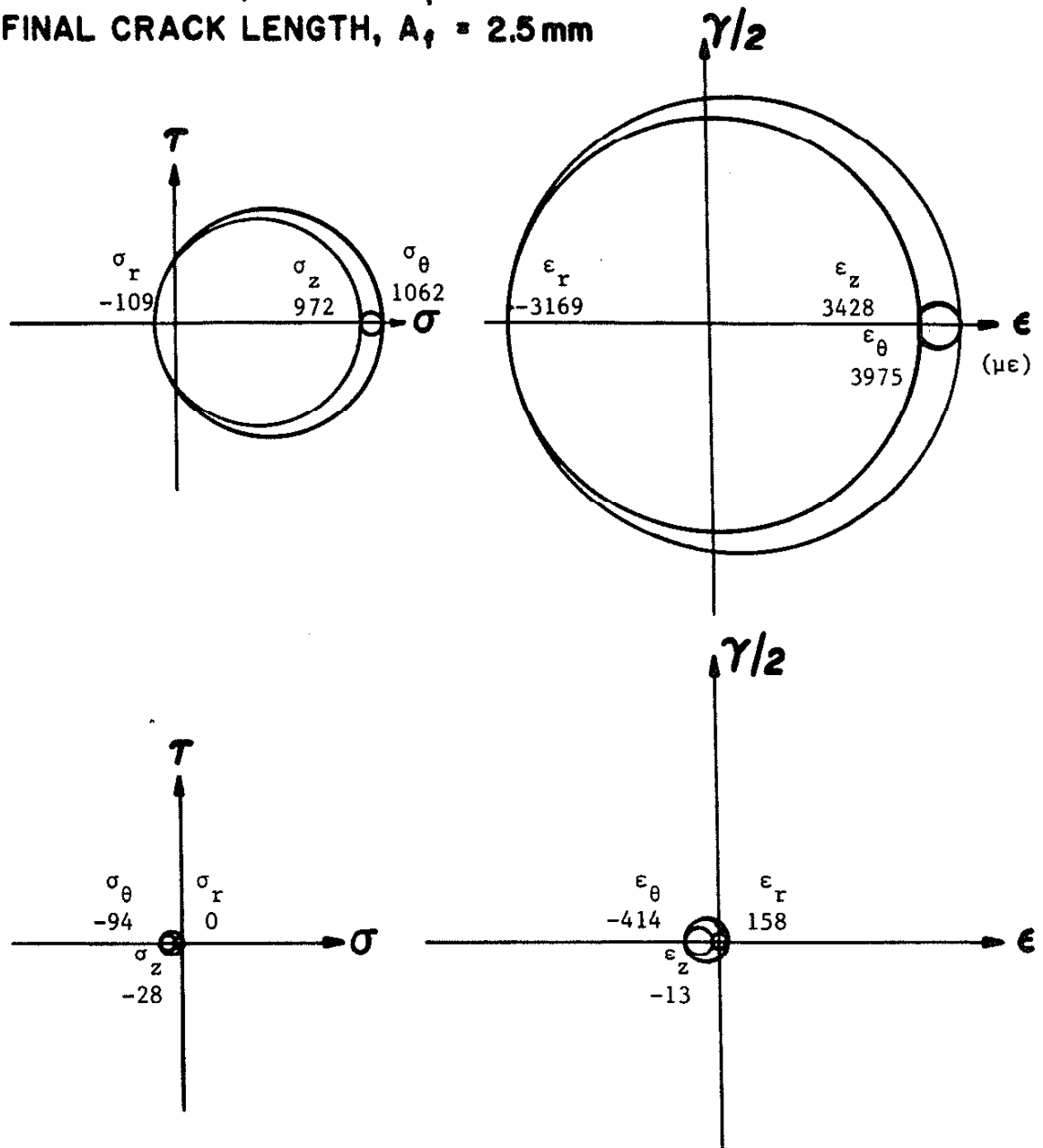


Figure 24. Test details and Mohr's circles for INDM08 on inner surface.

INDM08,  $N_f=25656$

$R_\sigma=0, \phi=1, \Delta\sigma=1140 \text{ MPa}$

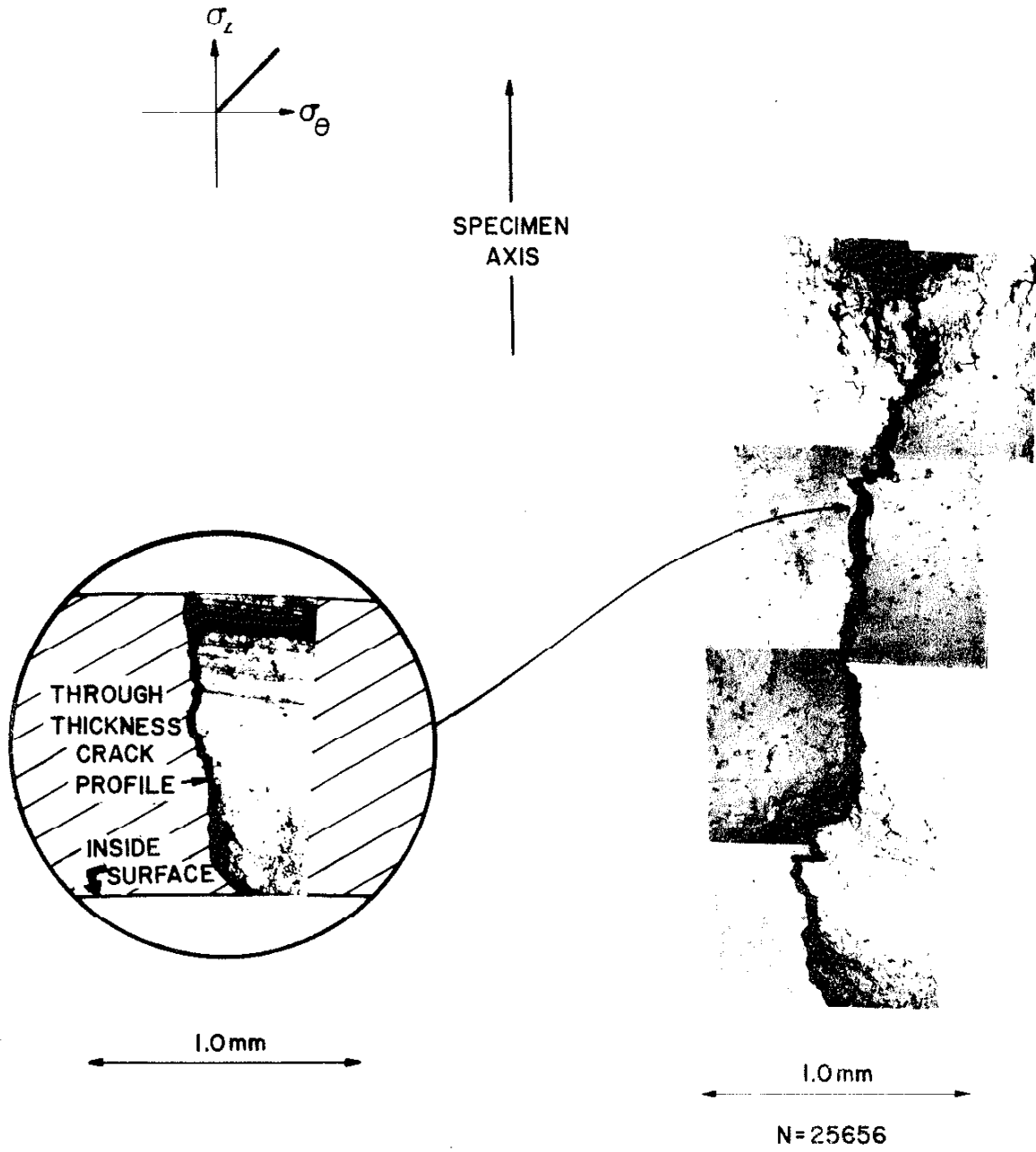


Figure 25. Cracking details for INDM08.

SPECIMEN IN01

CONTROL MODE , LOAD/PRESSURE

TEST LEVELS, Maximum  $\sigma_z = 1013\text{MPa}$  ,  $\sigma_\theta = 1083\text{MPa}$

Minimum  $\sigma_z = 0\text{MPa}$   $\sigma_\theta = 0\text{MPa}$

INITIATION LIFE,  $N_i = \text{N/A}$

Imm CRACK LIFE,  $N_{i,0} = \text{N/A}$

FAILURE LIFE,  $N_f = 30790$

FINAL CRACK LENGTH,  $A_f = 3.1\text{mm}$

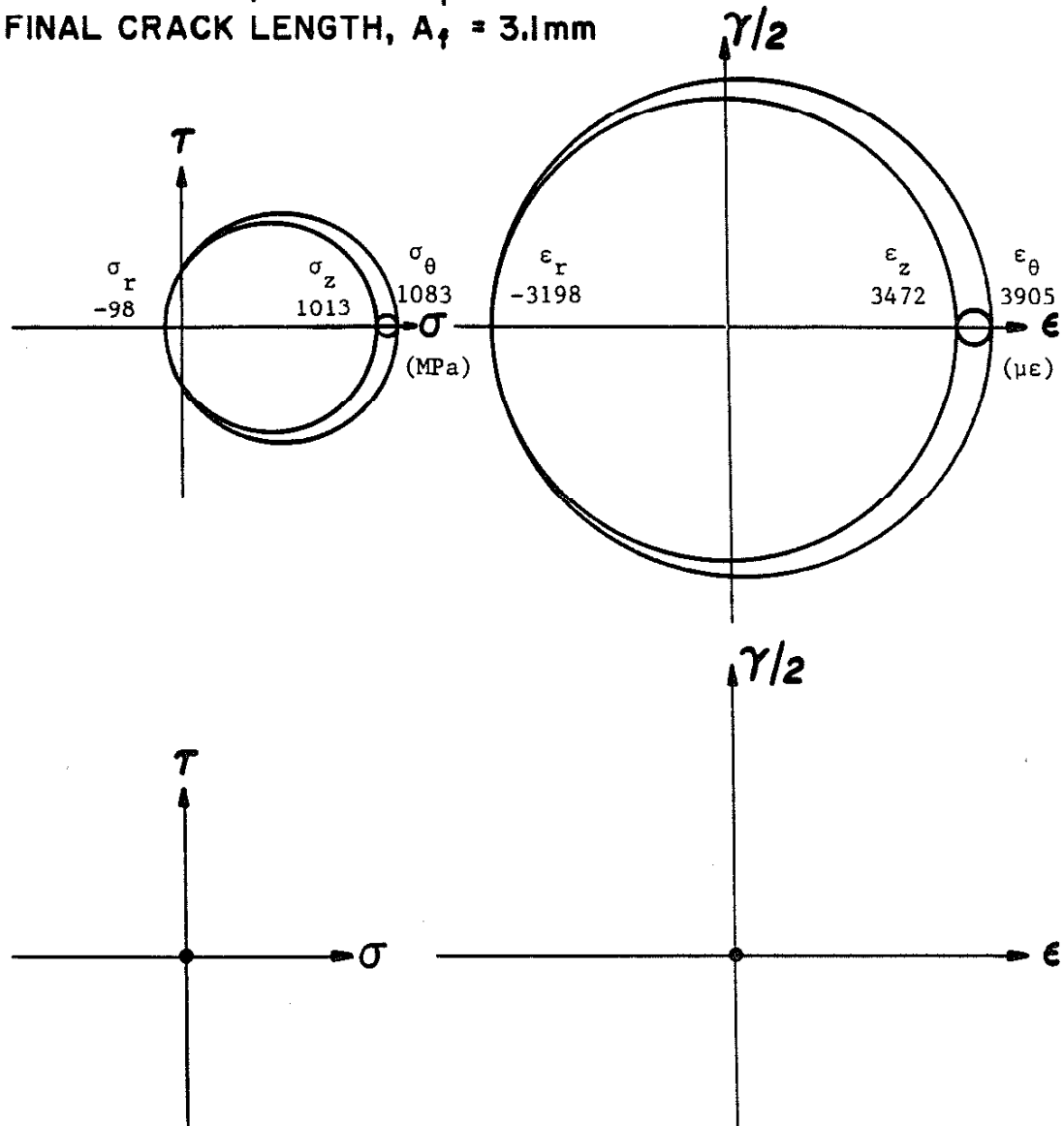


Figure 26. Test details and Mohr's circles for IN01 on inner surface.



SPECIMEN IN02

CONTROL MODE , LOAD/PRESSURE

TEST LEVELS, Maximum  $\sigma_z = 1013\text{MPa}$  ,  $\sigma_\theta = 1083\text{MPa}$

Minimum  $\sigma_z = 0\text{MPa}$   $\sigma_\theta = 0\text{MPa}$

INITIATION LIFE,  $N_i = \text{N/A}$

Imm CRACK LIFE,  $N_{i,0} = \text{N/A}$

FAILURE LIFE,  $N_f = 35910$

FINAL CRACK LENGTH,  $A_f = 3.3\text{mm}$

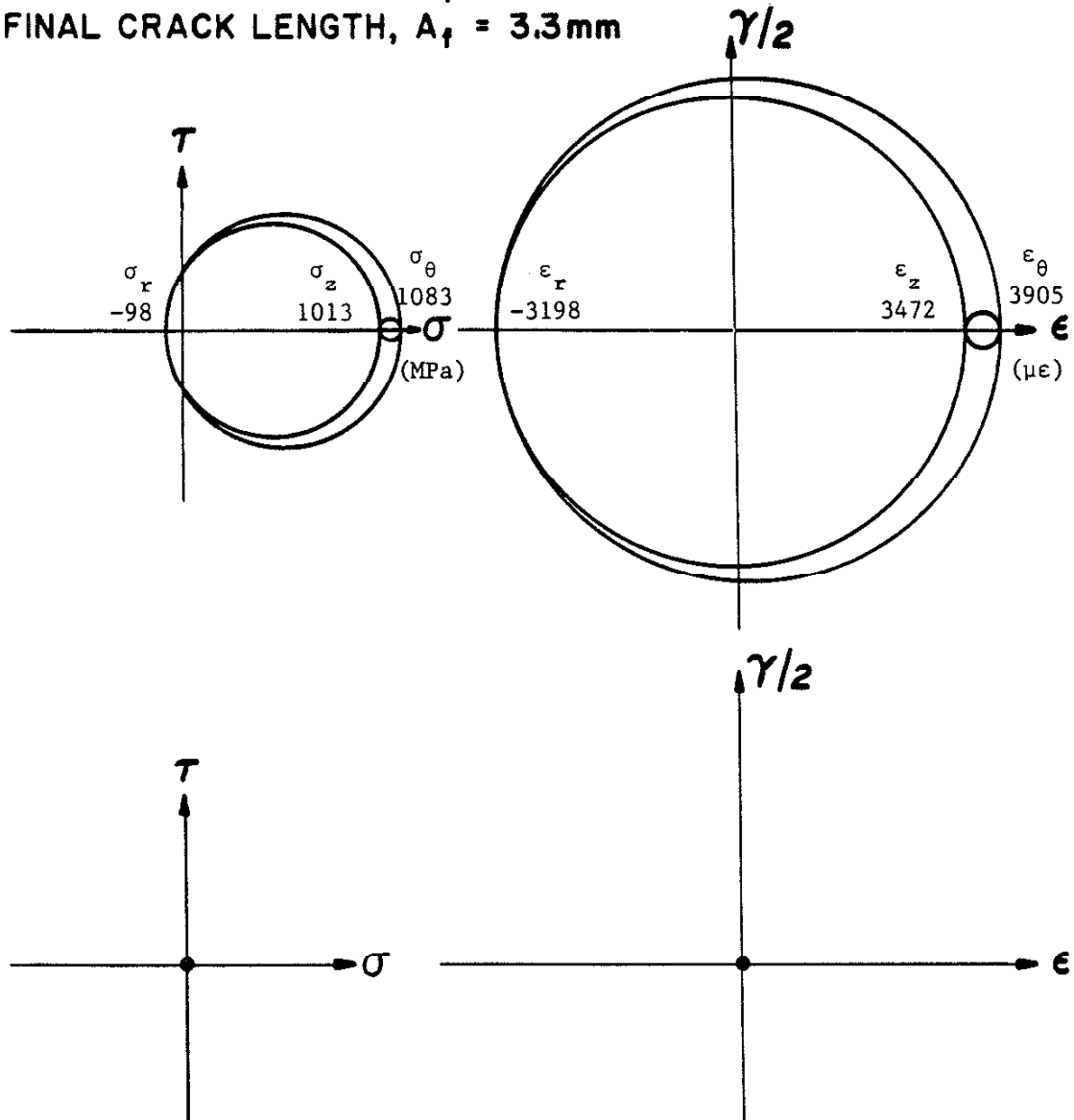
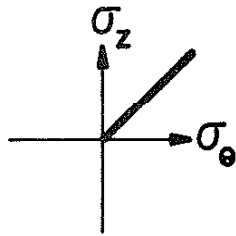


Figure 27. Test details and Mohr's circles for IN02 on inner surface.

INO1 and INO2

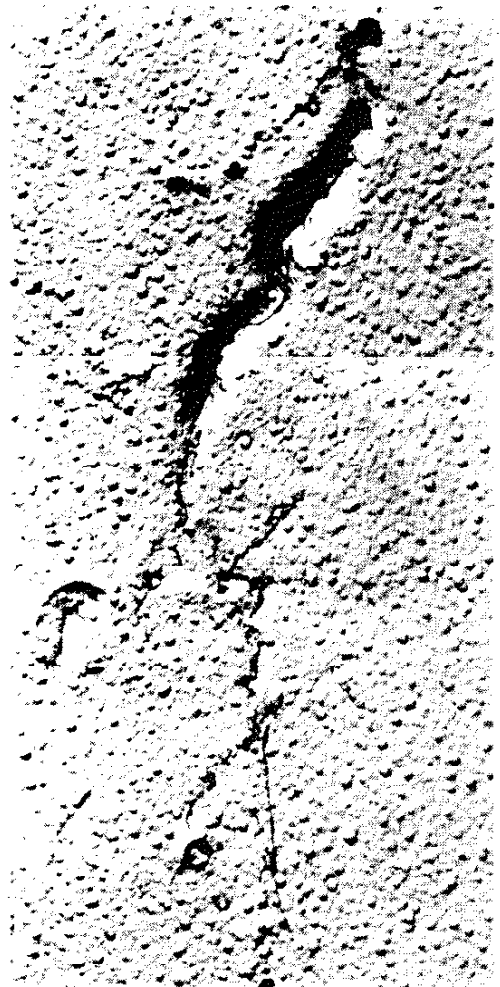
$R_\sigma = 0$ ,  $\phi = +1$ ,  $\Delta\sigma = 1034$



SPECIMEN  
AXIS

INO2

INO1



1.0mm  
N<sub>f</sub> = 30790

1.0mm  
N<sub>f</sub> = 35910

Figure 28. Failure cracks for INO1 and INO2.

**SPECIMEN INDM06**

**CONTROL MODE, LOAD/PRESSURE**

**TEST LEVELS, Maximum  $\sigma_z = 682 \text{ MPa}$ ,  $\sigma_\theta = 772 \text{ MPa}$**   
**Minimum  $\sigma_z = 0 \text{ MPa}$ ,  $\sigma_\theta = 0 \text{ MPa}$**

**INITIATION LIFE,  $N_i = 40\,000$**

**Imm CRACK LIFE,  $N_{i,0} = 124\,000$**

**FAILURE LIFE,  $N_f = 142\,836$**

**FINAL CRACK LENGTH,  $A_f = 4.0 \text{ mm}$**

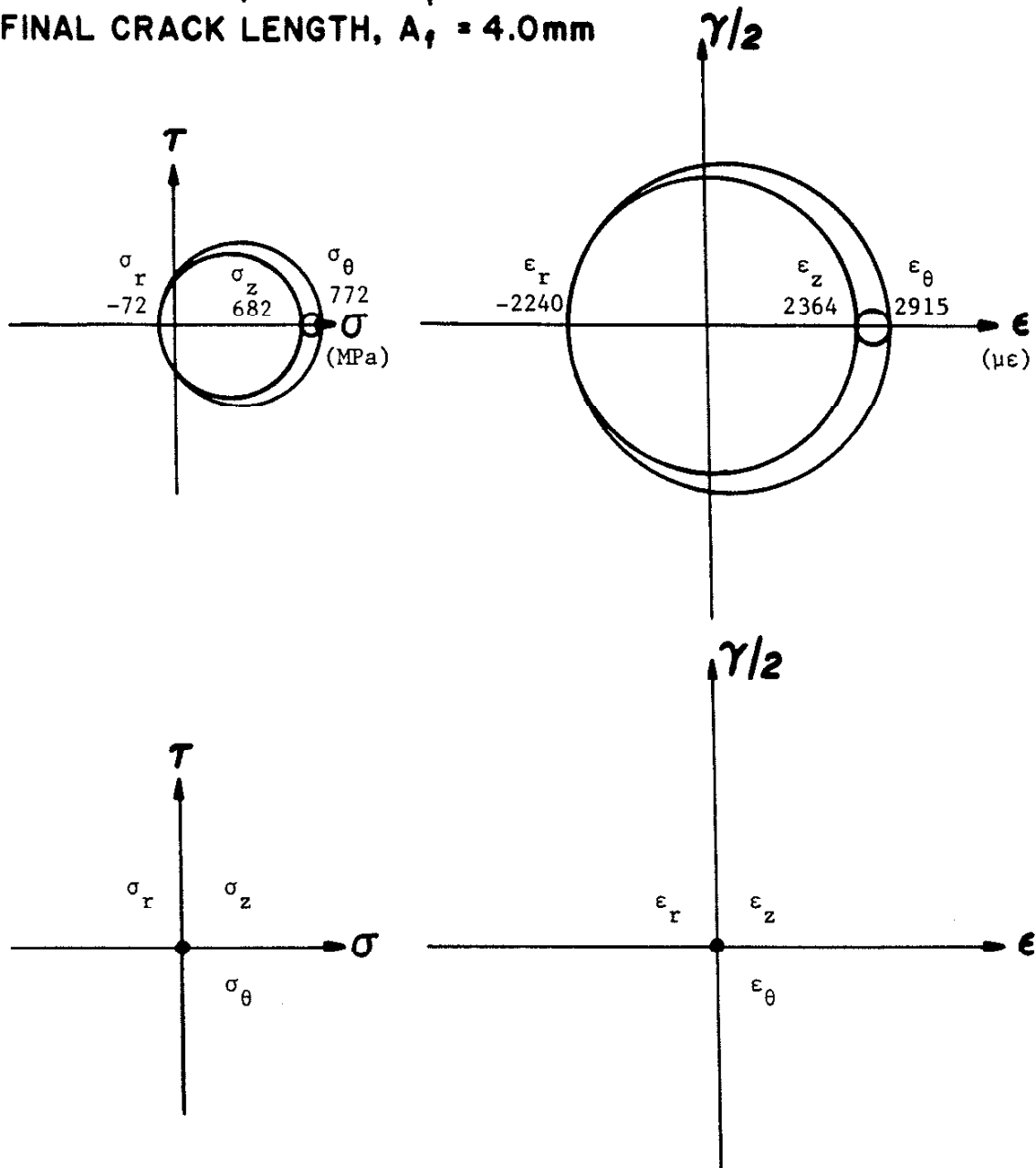
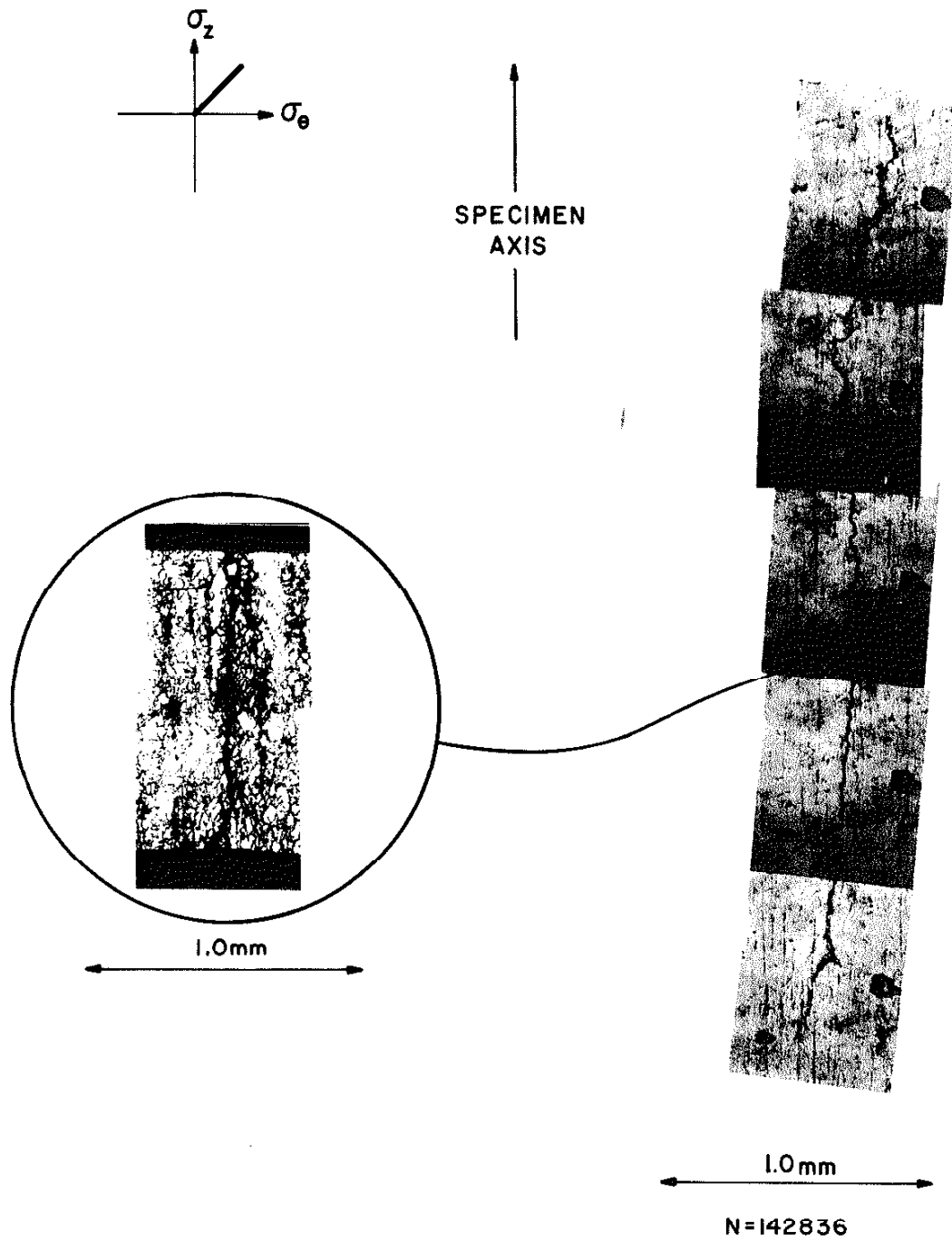


Figure 29. Test details and Mohr's circles for INDM06 on inner surface.

INDM06, N<sub>F</sub>=142836

R<sub>σ</sub> = 0, O = +1, Δσ = 690 MPa



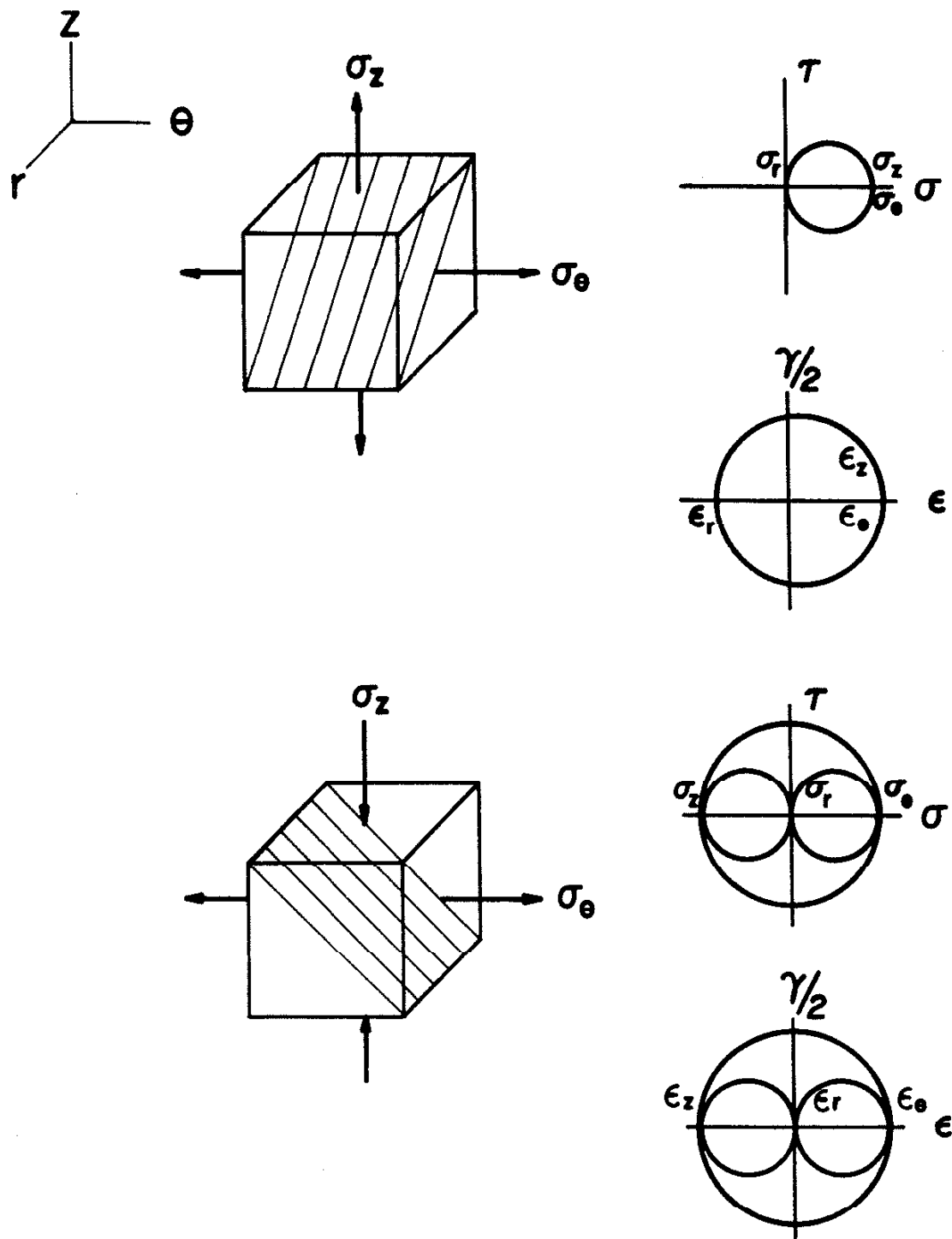


Figure 31. Mohr's circles for biaxial mean stress tests on outer surface.

**SPECIMEN INA4**

**CONTROL MODE STRAIN/PRESSURE**

**TEST LEVELS, Maximum  $\epsilon_z = 0.00433$  ,  $\sigma_\theta = 524$  MPa**

**Minimum  $\epsilon_z = -0.00566$  ,  $\sigma_\theta = 524$  MPa**

**INITIATION LIFE,  $N_i = N/A$**

**Imm CRACK LIFE,  $N_{i,0} = N/A$**

**FAILURE LIFE,  $N_f = 3654$**

**FINAL CRACK LENGTH,  $A_f = N/A$**

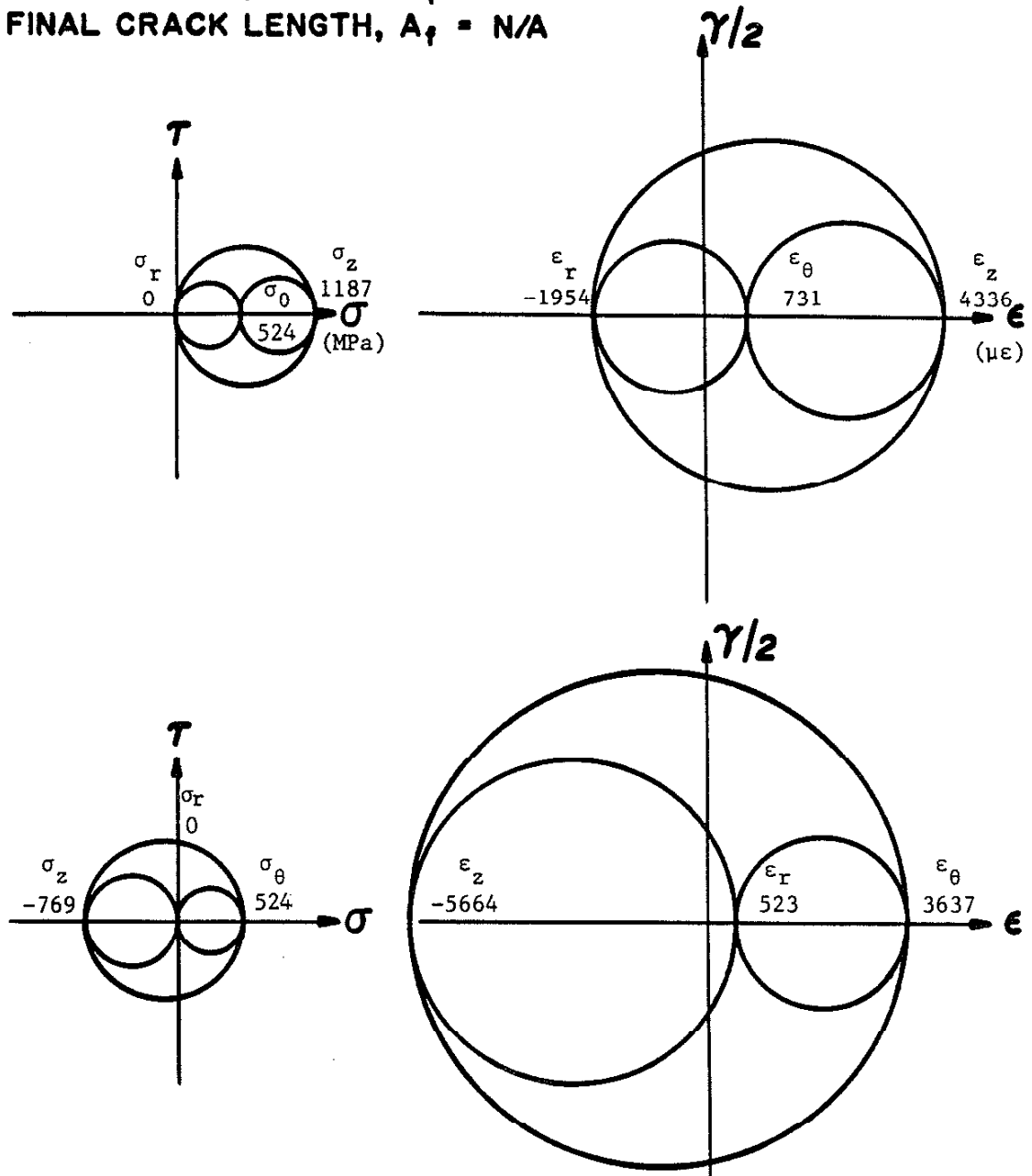


Figure 32. Test details and Mohr's circles for INA4 on outer surface.

**SPECIMEN INA17**

**CONTROL MODE STRAIN/PRESSURE**

**TEST LEVELS, Maximum  $\epsilon_z = 0.004348$ ,  $\sigma_\theta = 530$  MPa**

**Minimum  $\epsilon_z = -0.005652$ ,  $\sigma_\theta = 530$  MPa**

**INITIATION LIFE,  $N_i = N/A$**

**Imm CRACK LIFE,  $N_{i,0} = N/A$**

**FAILURE LIFE,  $N_f = 3293$**

**FINAL CRACK LENGTH,  $A_f = N/A$**

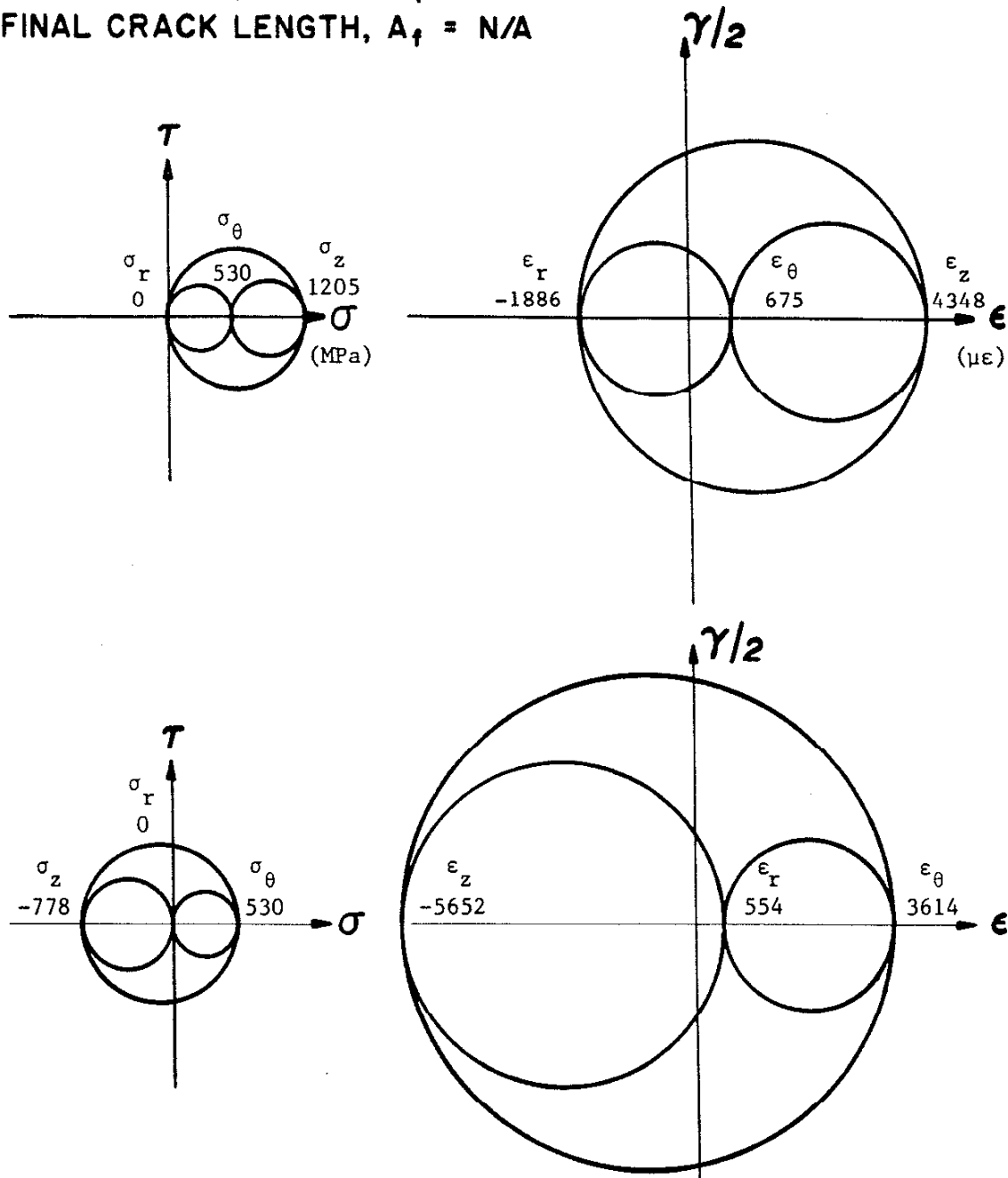


Figure 33. Test details and Mohr's circles for INA17 on outer surface.

INA4,  $N_f=3654$

$\Delta\epsilon_z/2=0.005$ ,  $\sigma_\theta=517\text{ MPa}$

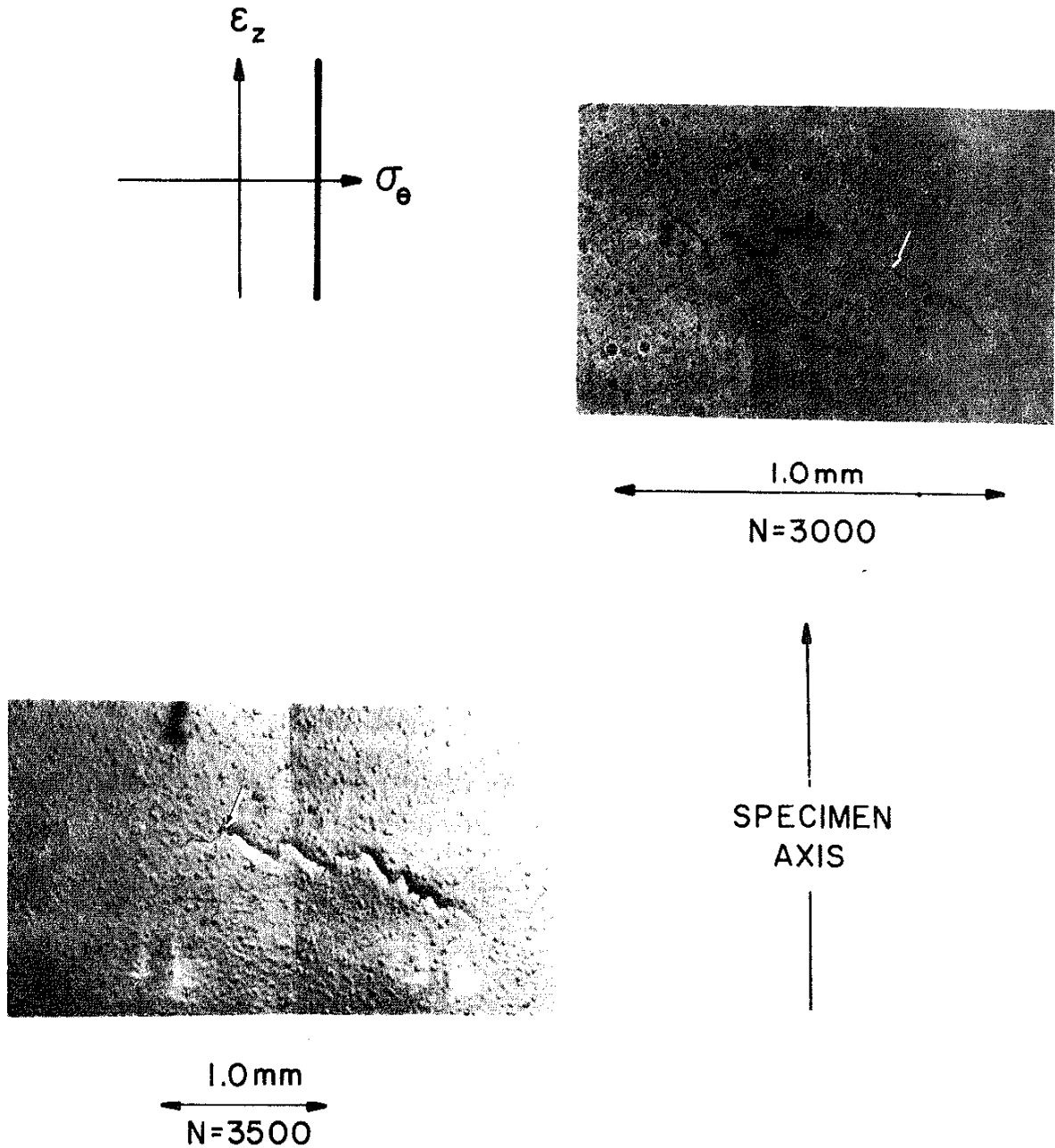
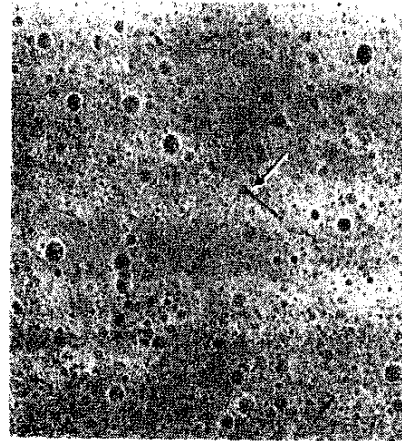
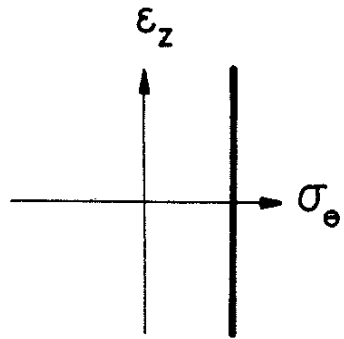


Figure 34. Cracking details for INA4.



INA17,  $N_f=3293$

$\Delta\epsilon_z/2=0.005$ ,  $\sigma_\theta=517\text{MPa}$



0.5mm  
N=2000



0.5mm  
N=2500

SPECIMEN  
AXIS

Figure 35. Cracking details for INA17.

**SPECIMEN INA5**

**CONTROL MODE STRAIN/PRESSURE**

**TEST LEVELS, Maximum  $\epsilon_z=0.004634$  ,  $\sigma_\theta=281$  MPa**

**Minimum  $\epsilon_z=-0.005366$  ,  $\sigma_\theta=281$  MPa**

**INITIATION LIFE,  $N_i = N/A$**

**Imm CRACK LIFE,  $N_{i,0} = N/A$**

**FAILURE LIFE,  $N_f = 6735$**

**FINAL CRACK LENGTH,  $A_f = N/A$**

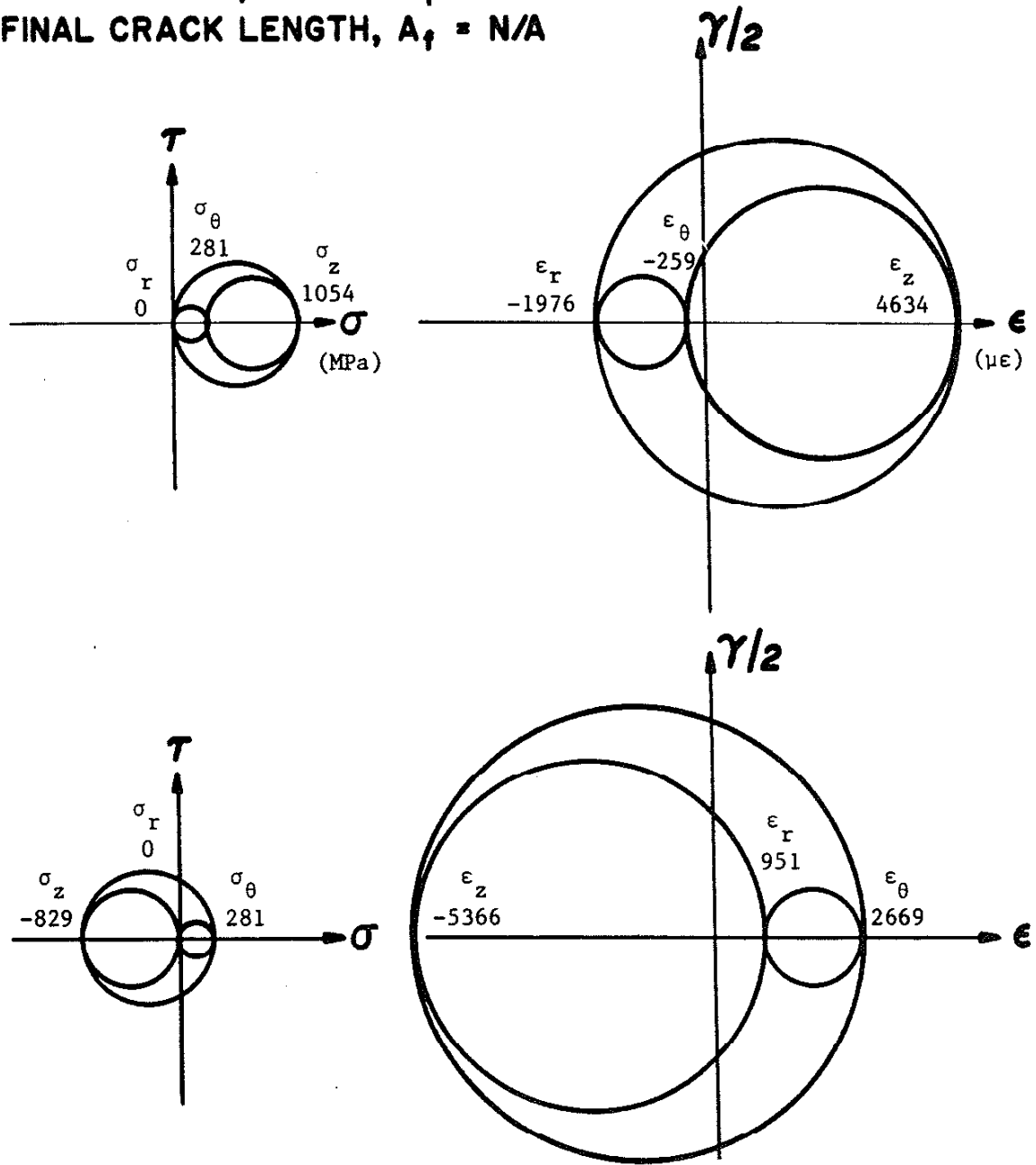


Figure 36. Test details and Mohr's circles for INA5 on outer surface.

SPECIMEN INAI3

CONTROL MODE STRAIN/PRESSURE

TEST LEVELS, Maximum  $\epsilon_z = 0.00463$  ,  $\sigma_\theta = 281 \text{ MPa}$

Minimum  $\epsilon_z = -0.00536$  ,  $\sigma_\theta = 281 \text{ MPa}$

INITIATION LIFE,  $N_i = \text{N/A}$

Imm CRACK LIFE,  $N_{i,0} = \text{N/A}$

FAILURE LIFE,  $N_f = 7221$

FINAL CRACK LENGTH,  $A_f = \text{N/A}$

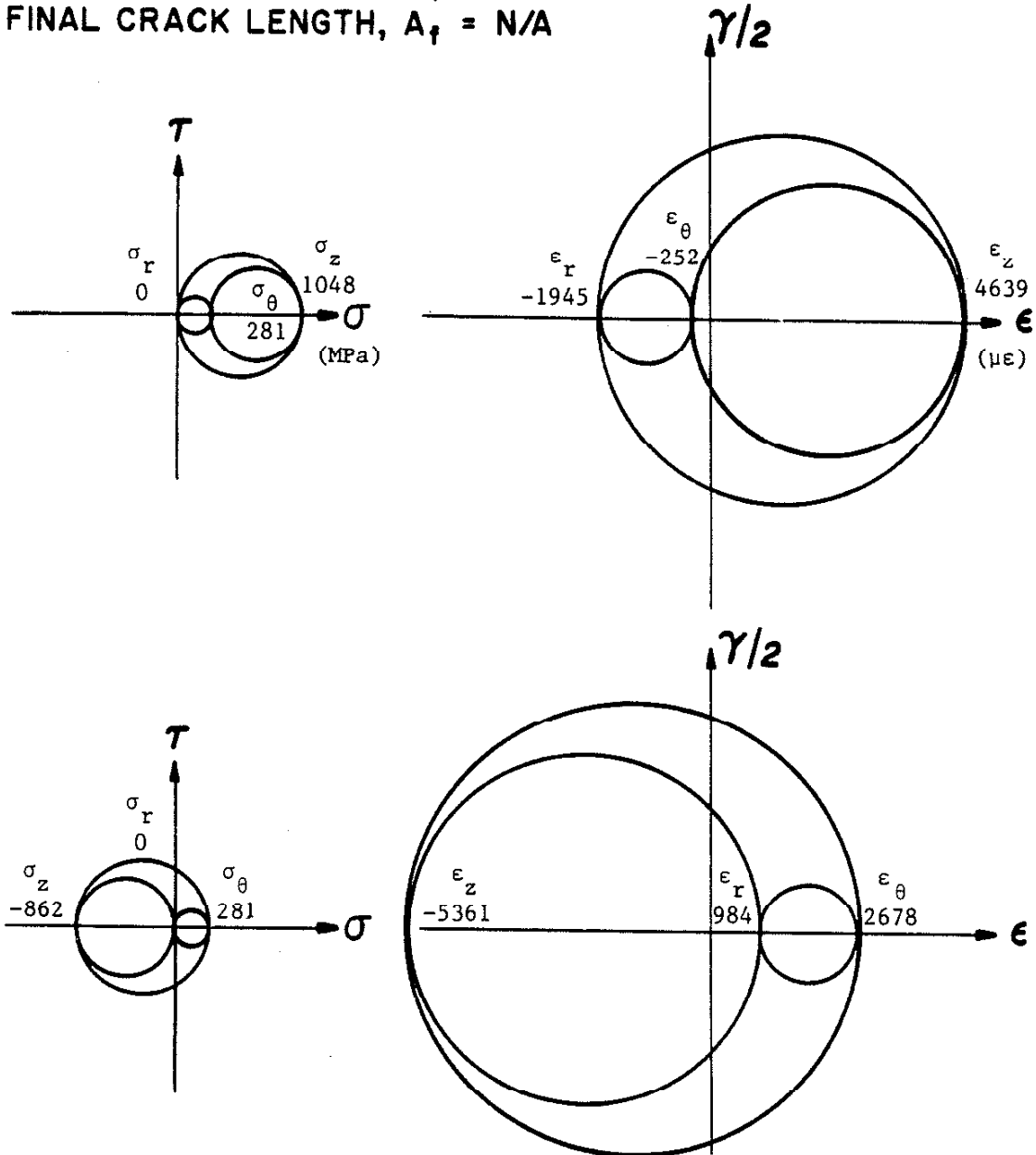


Figure 37. Test details and Mohr's circles for INAI3 on outer surface.

INA5,  $N_f=6735$

$\Delta\epsilon_z/2=0.005$ ,  $\sigma_e=276$  MPa

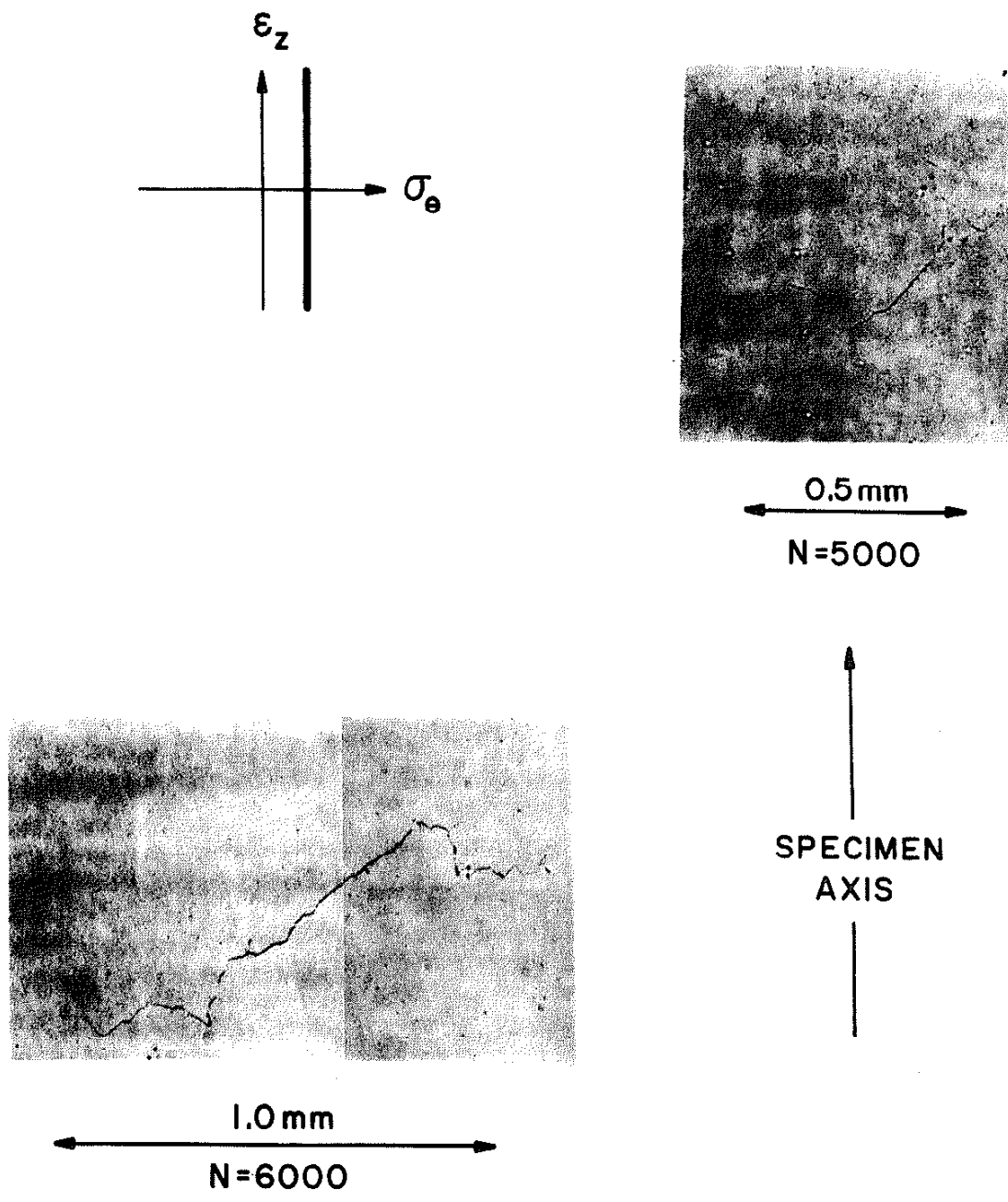
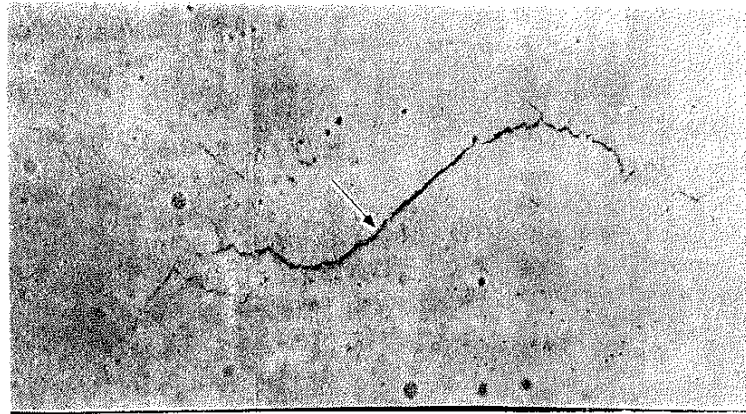
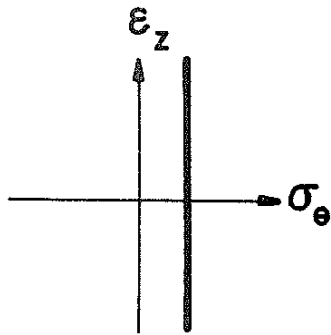


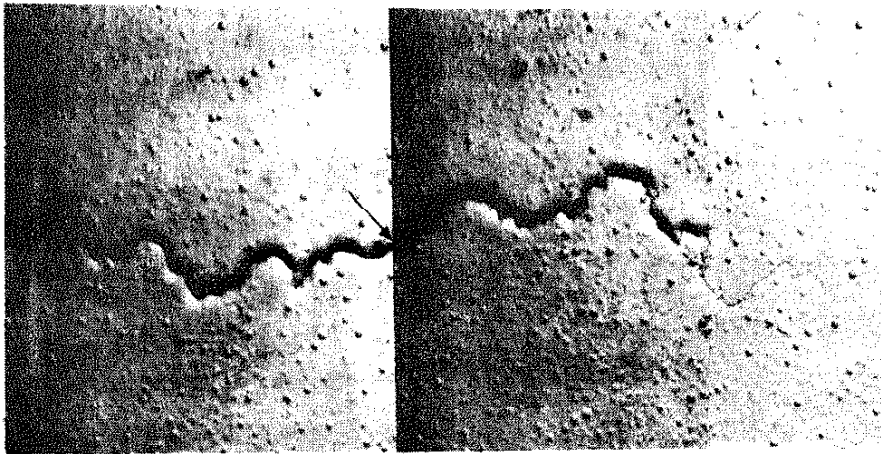
Figure 38. Cracking details for INA5.

INA13,  $N_f=7221$

$\Delta\varepsilon_z/2=0.005$ ,  $\sigma_\theta=276\text{ MPa}$



0.5mm  
N=6000



1.0mm  
N=7000

SPECIMEN  
AXIS

Figure 39. Cracking details for INA13.

**SPECIMEN INAI2**

**CONTROL MODE LOAD/PRESSURE**

**TEST LEVELS, Maximum  $\sigma_z=514\text{MPa}$ ,  $\sigma_\theta=522\text{MPa}$**

**Minimum  $\sigma_z=-514\text{MPa}$ ,  $\sigma_\theta=522\text{MPa}$**

**INITIATION LIFE,  $N_i = \text{N/A}$**

**Imm CRACK LIFE,  $N_{i,0} = \text{N/A}$**

**FAILURE LIFE,  $N_f = 142100$**

**FINAL CRACK LENGTH,  $A_f = \text{N/A}$**

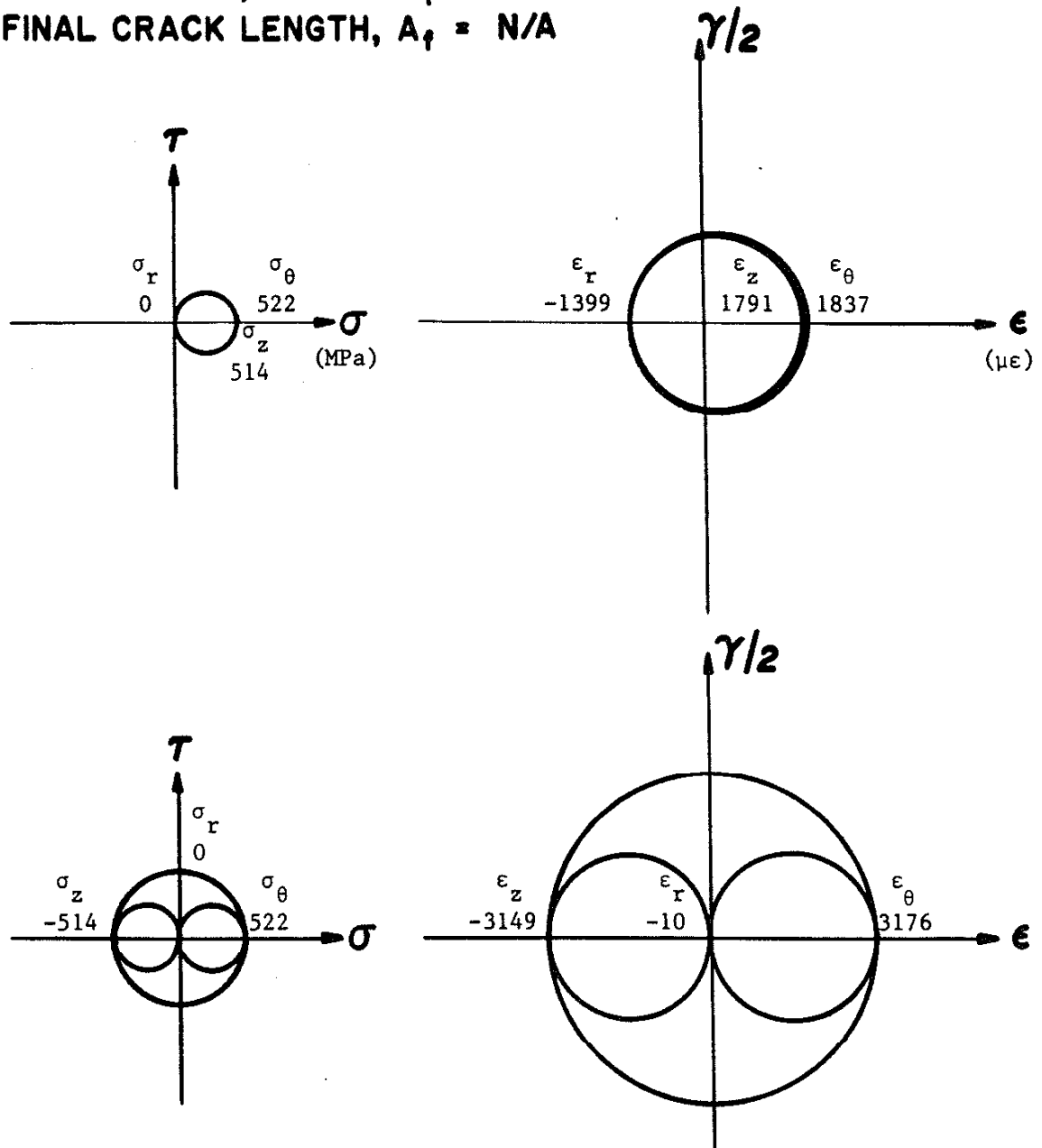


Figure 40. Test details and Mohr's circles for INA12 on outer surface.

**SPECIMEN INA23**

**CONTROL MODE LOAD/PRESSURE**

**TEST LEVELS, Maximum  $\sigma_z=510\text{MPa}$  ,  $\sigma_\theta=508\text{MPa}$**

**Minimum  $\sigma_z=-510\text{MPa}$ ,  $\sigma_\theta=508\text{MPa}$**

**INITIATION LIFE,  $N_i = \text{N/A}$**

**Imm CRACK LIFE,  $N_{i,0} = \text{N/A}$**

**FAILURE LIFE,  $N_f = 165100$**

**FINAL CRACK LENGTH,  $A_f = \text{N/A}$**

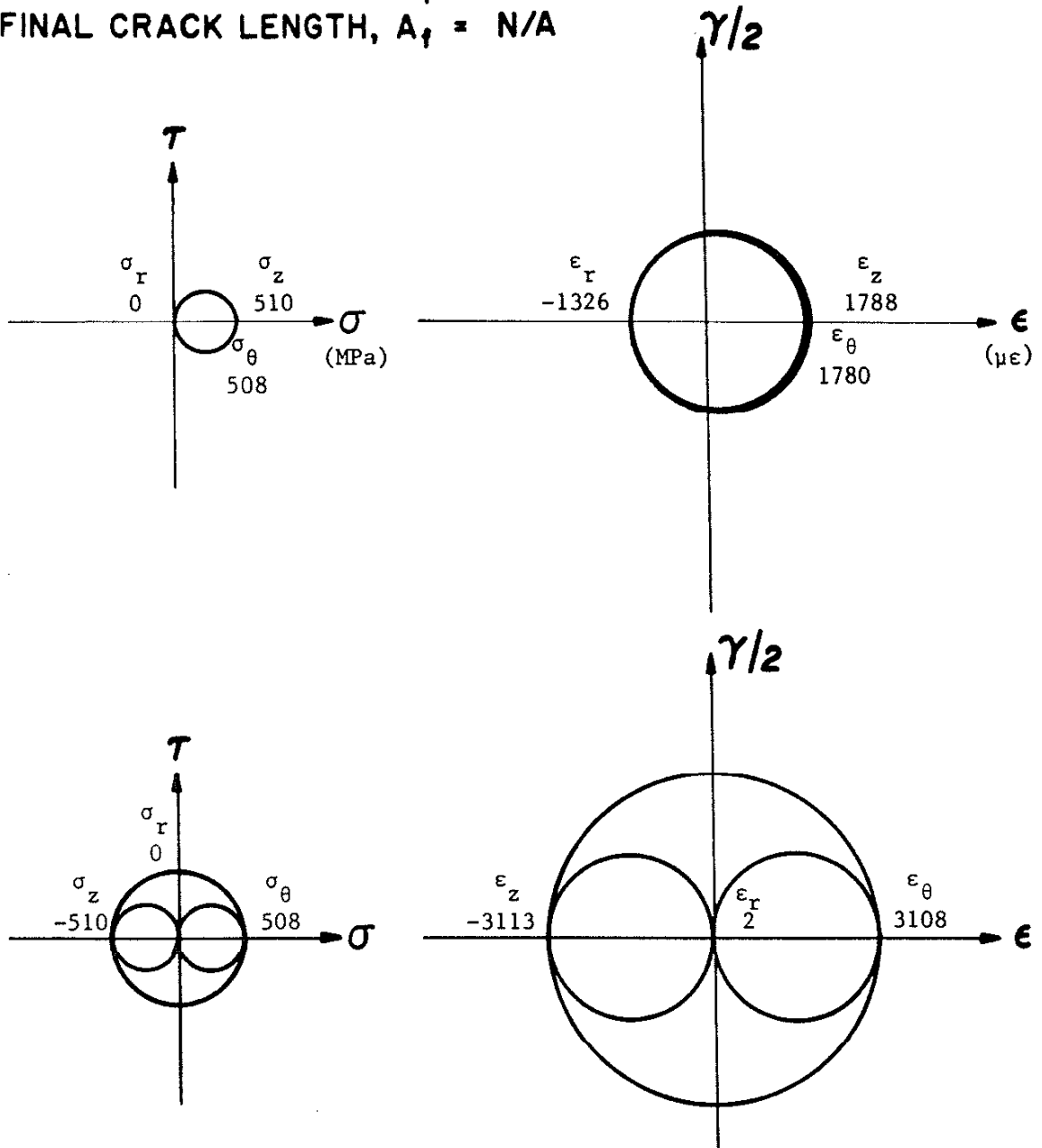


Figure 41. Test details and Mohr's circles for INA23 on outer surface.

INA12,  $N_f=142061$   
 $\Delta\sigma_z/2=517 \text{ MPa}$ ,  $\sigma_e=517 \text{ MPa}$

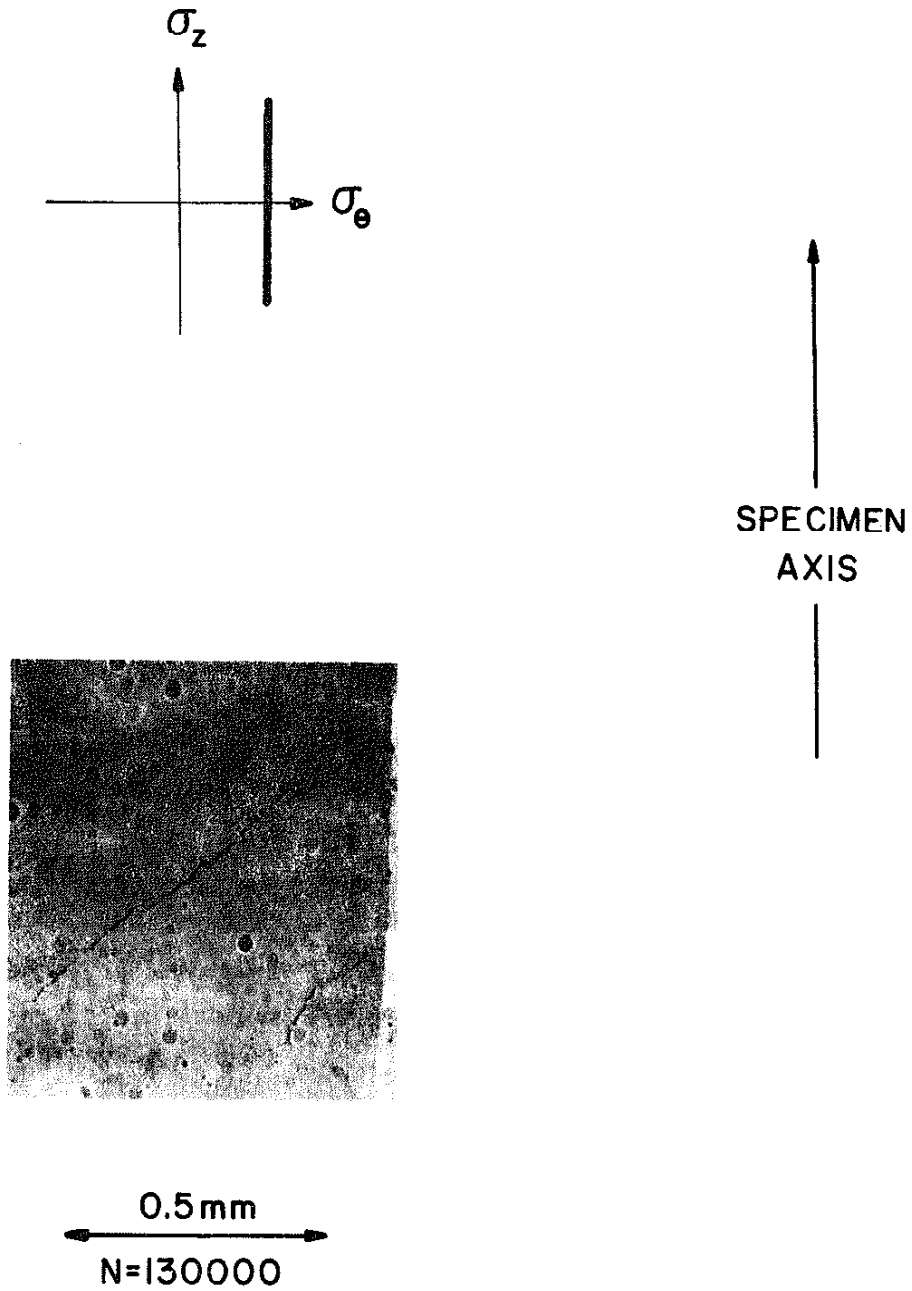


Figure 42. Cracking details for INA12.



INA23,  $N_f=165088$

$\Delta\sigma_z/2=517$  MPa,  $\sigma_\theta=517$  MPa

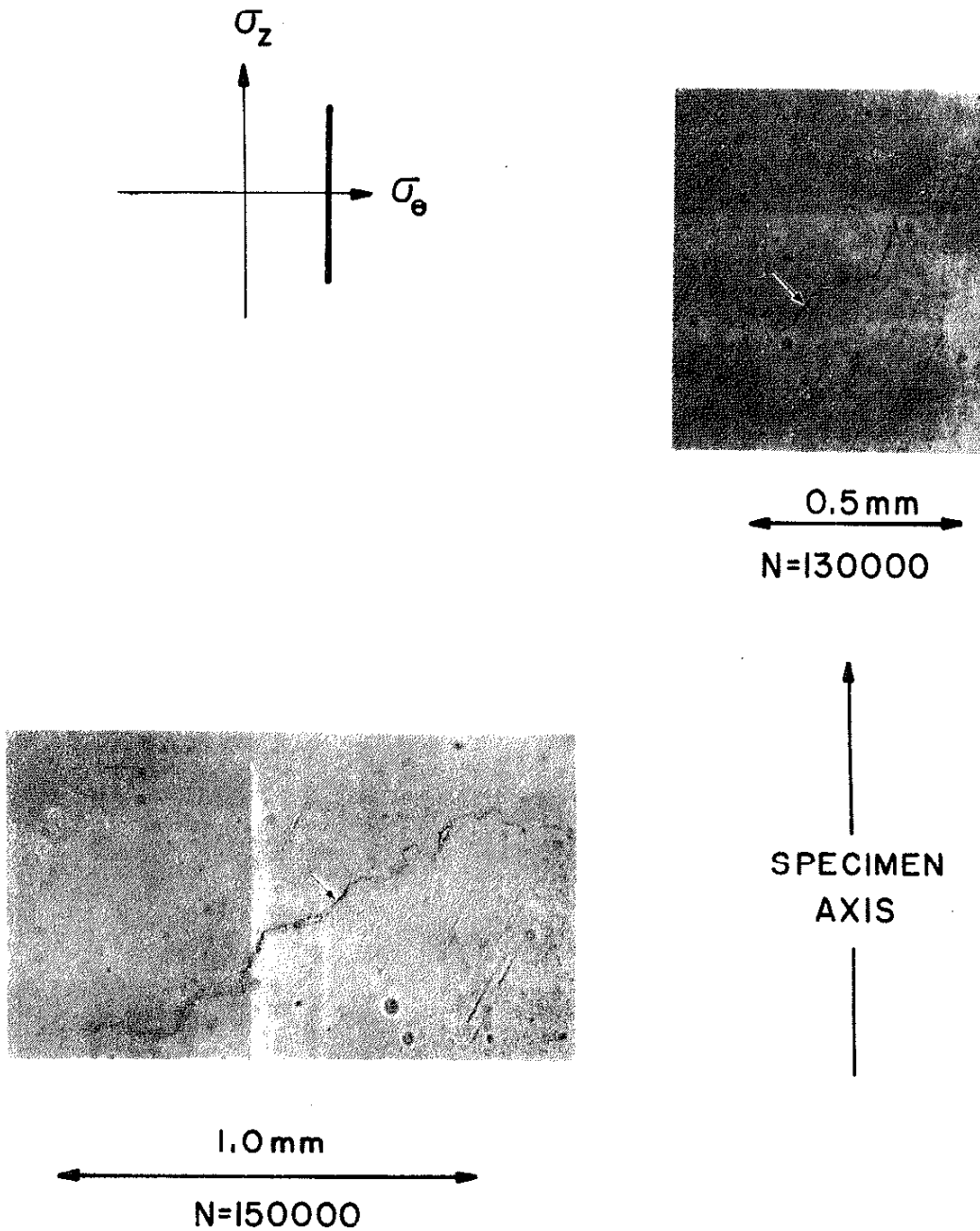


Figure 43. Cracking details for INA23.

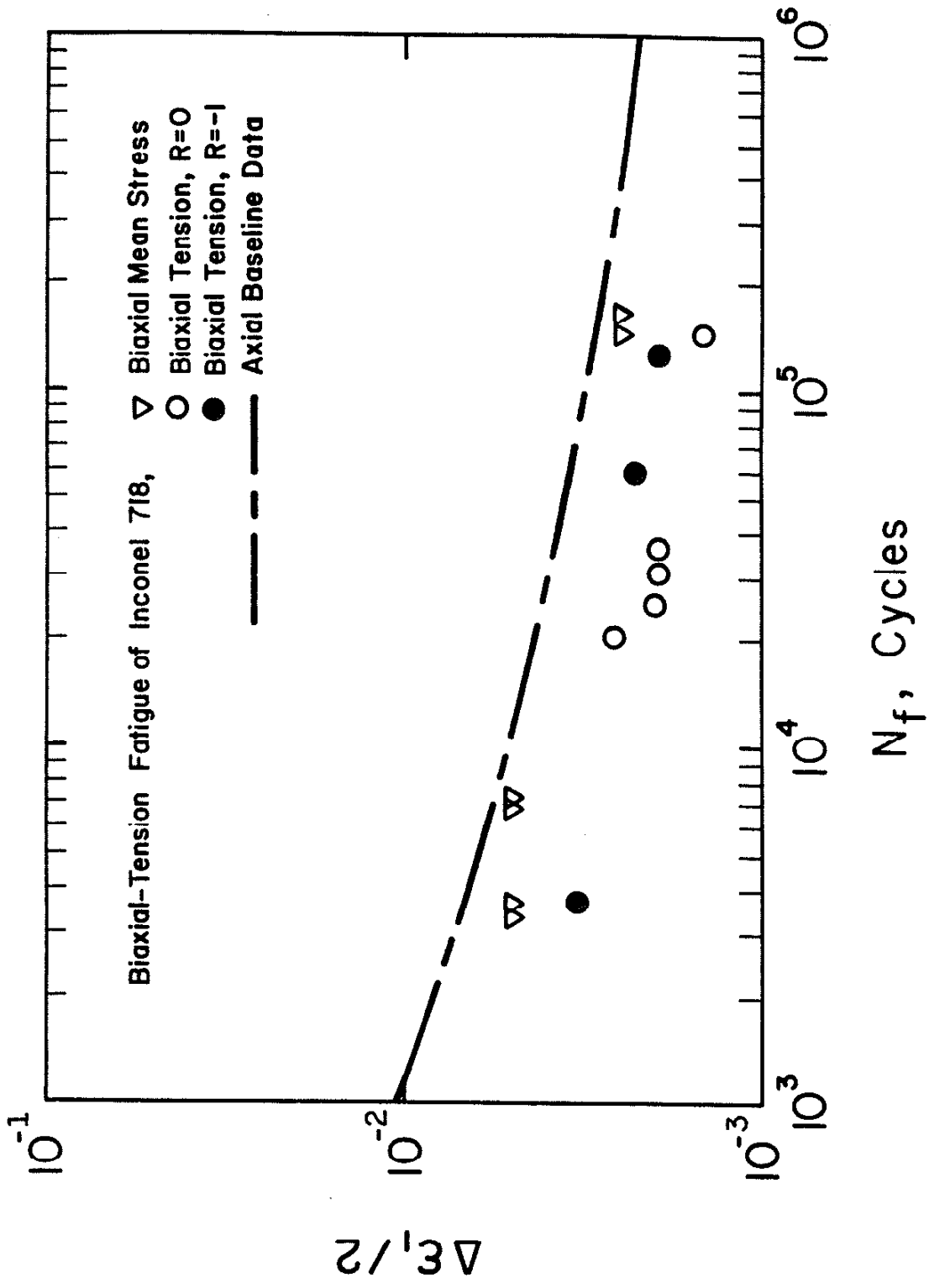


Figure 44. Life predictions for biaxial-tension data, maximum principal strain theory.

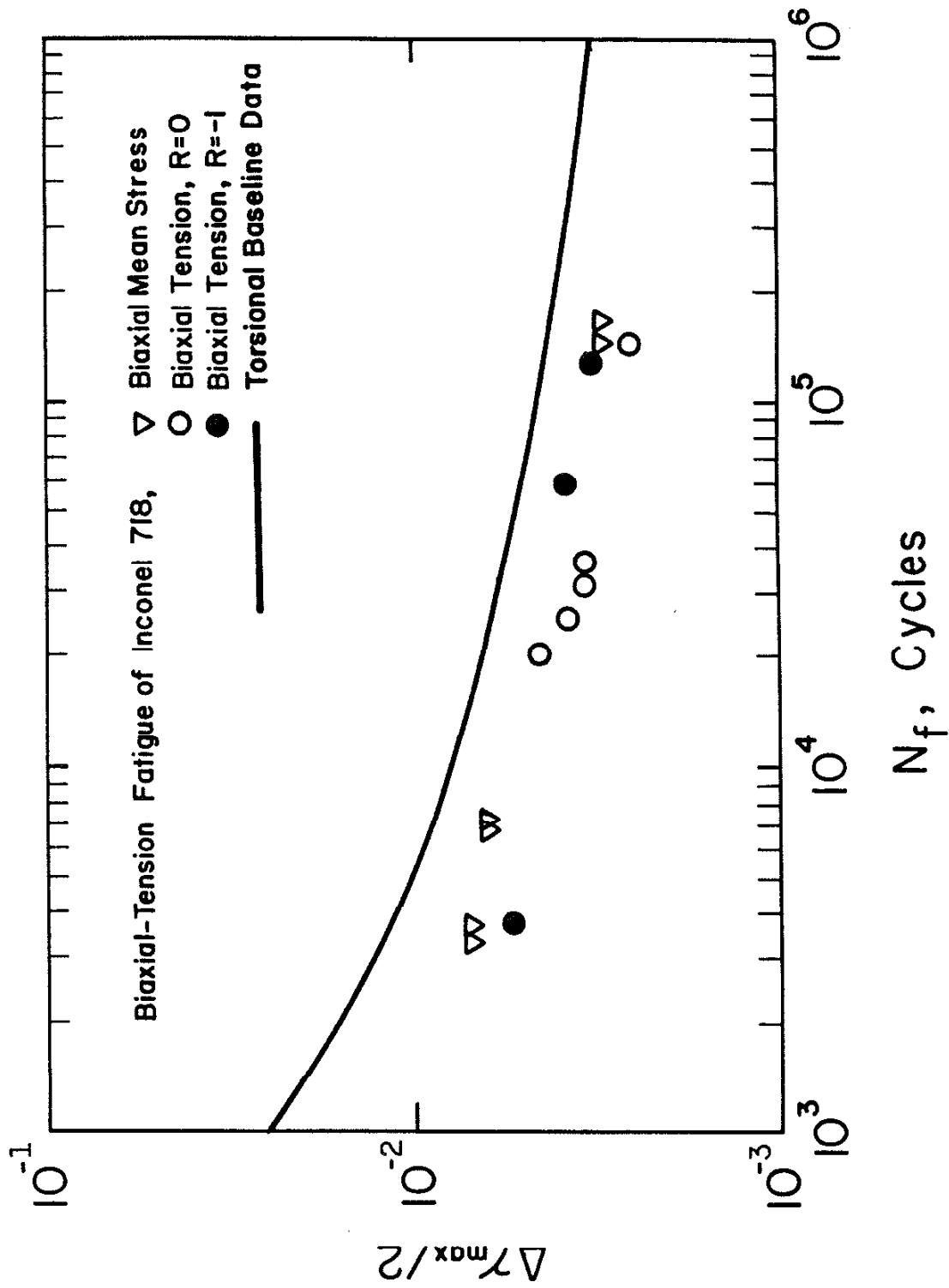


Figure 45. Life predictions for biaxial-tension data, maximum shear strain (Tresca's) theory.

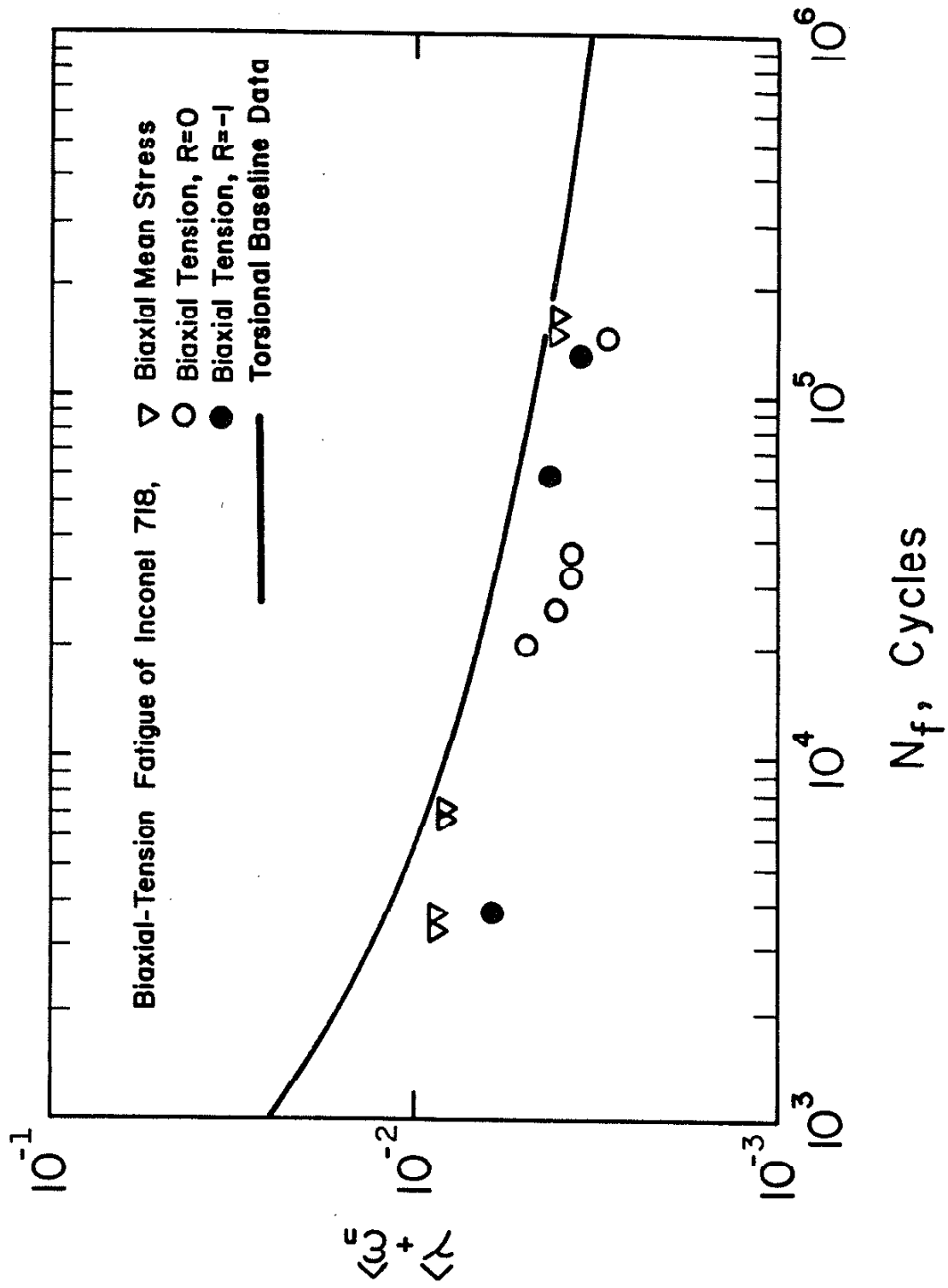


Figure 46. Life predictions for biaxial-tension data, Brown and Miller theory.

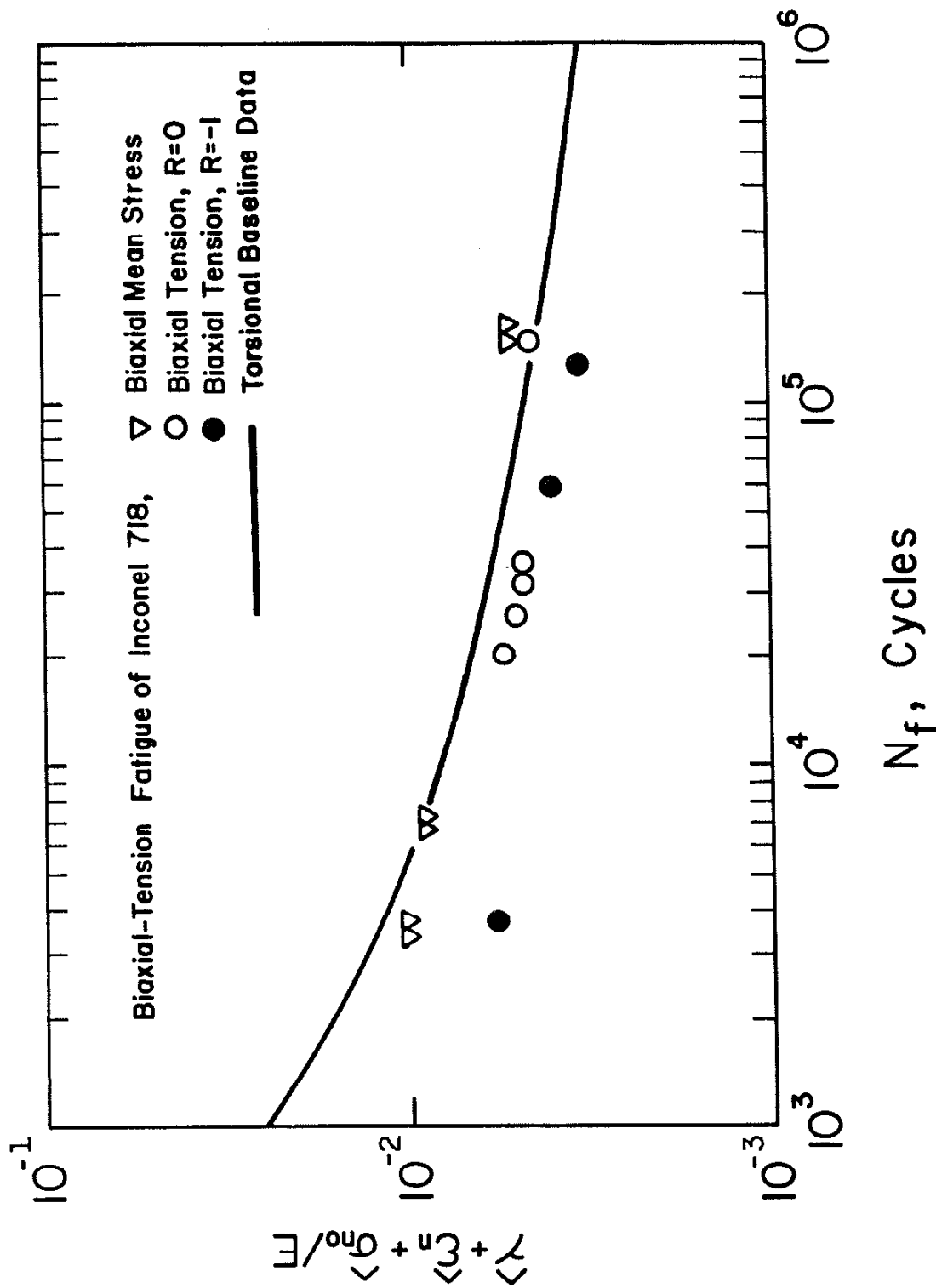


Figure 47. Life predictions for biaxial-tension data, Socie's mean stress modified Brown and Miller theory.

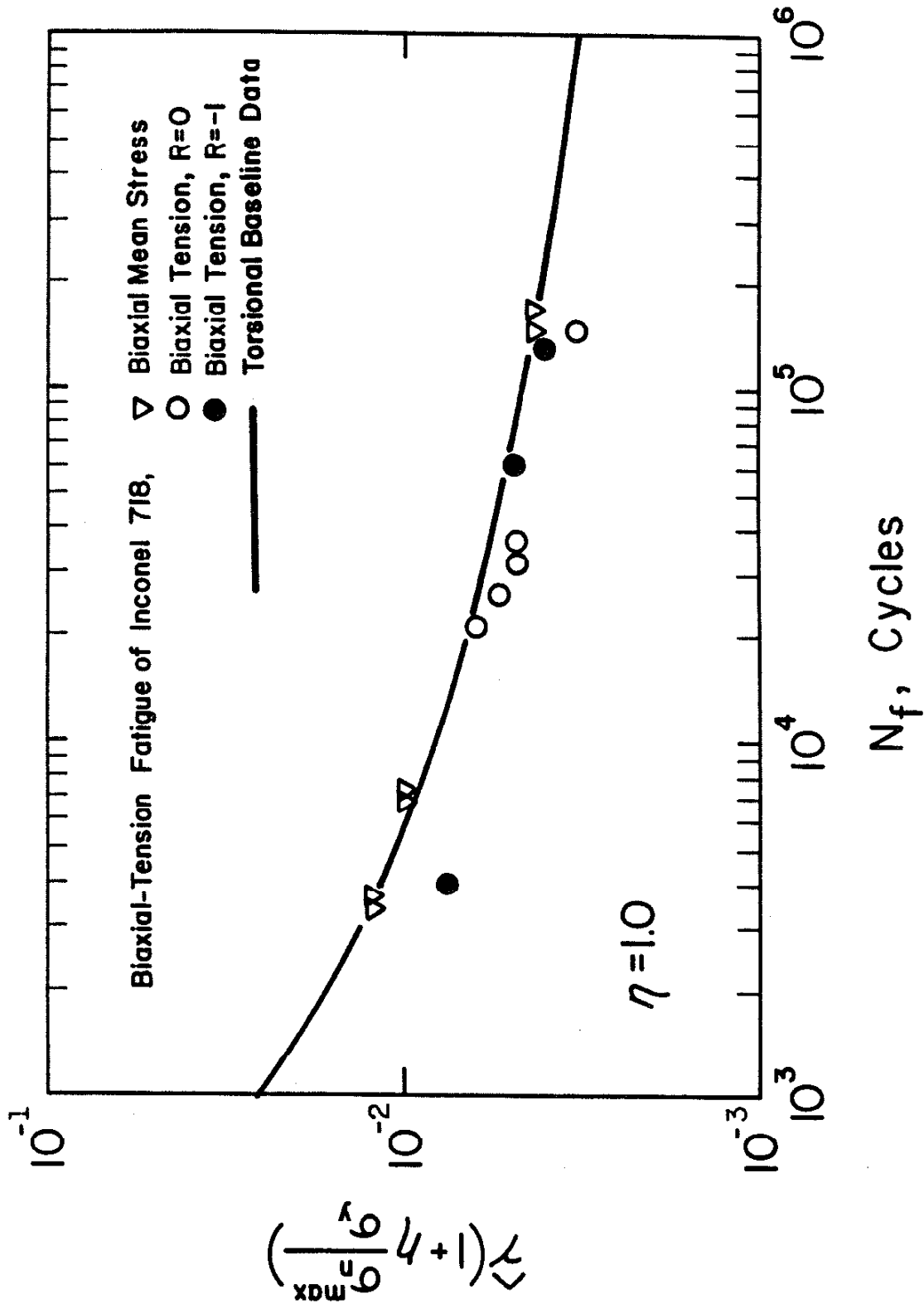


Figure 48. Life predictions for biaxial-tension data, Fatemi and Socie theory.

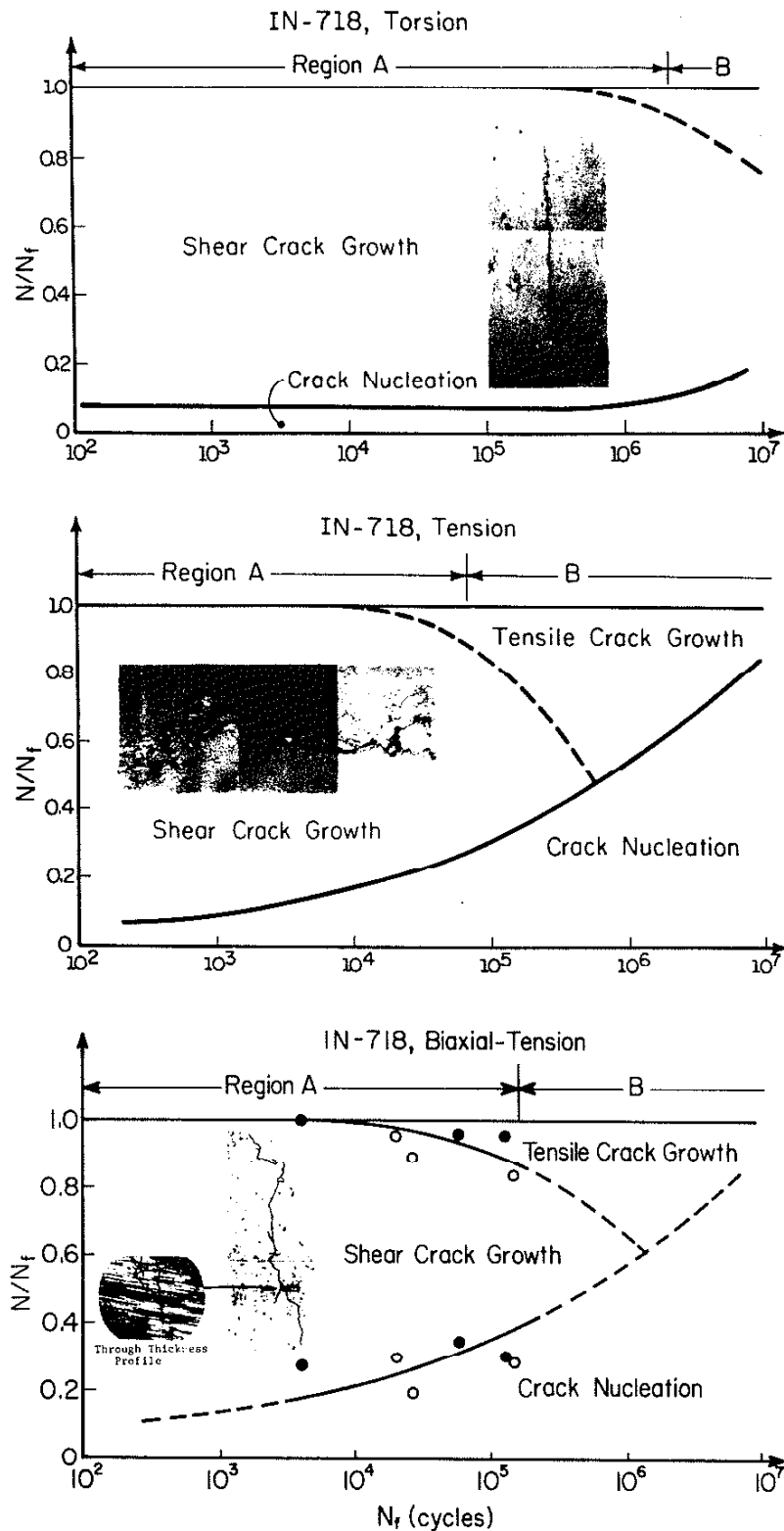


Figure 49. Fatigue damage maps with cracking behavior for torsion, tension, and biaxial-tension loadings.

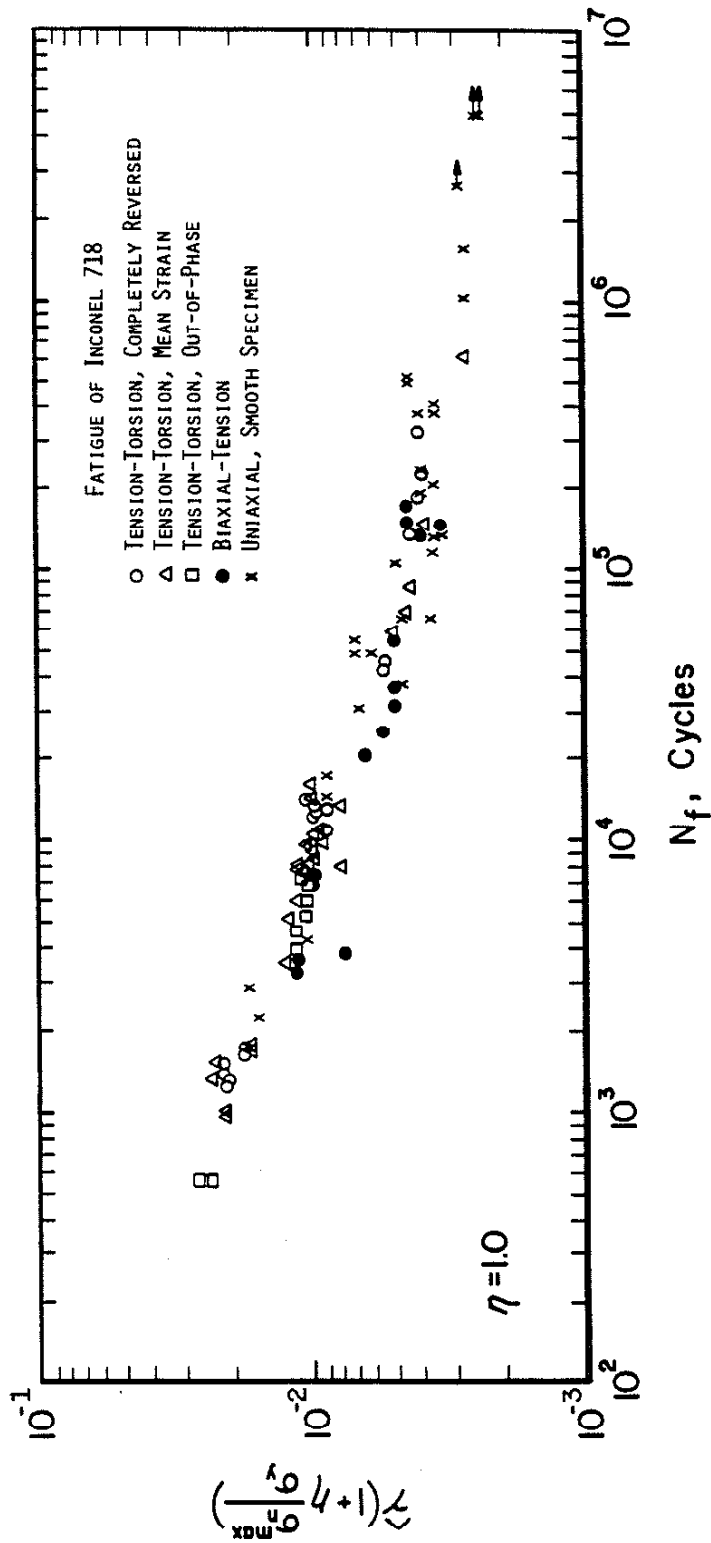


Figure 50. Correlation of Inconel 718 tests from all stress quadrants using Fatemi and Socie's theory.



#### REFERENCES

1. Socie, D. F., Waill, L. E., and Dittmer, D. F., "Biaxial Fatigue of Inconel 718 Including Mean Stress Effects," Multiaxial Fatigue, ASTM STP 853, K. J. Miller and M. W. Brown, Eds., American Society for Testing and Materials, 1985, pp. 463-481.
2. Waill, L. E., Crack Observations in Biaxial Fatigue, Department of Mechanical and Industrial Engineering, Design and Materials Division Report No. 108, University of Illinois at Urbana-Champaign, 1983.
3. Beer, T. A., "Crack Shapes During Biaxial Fatigue," Materials Engineering Mechanical Behavior, Report No. 106, College of Engineering, University of Illinois, Urbana, IL, 1984.
4. Socie, D. F., and Shield, T. W., "Mean Stress Effects in Biaxial Fatigue of Inconel 718," Journal of Engineering Materials and Technology, Vol. 106, 1984, pp. 227-232.
5. Koch, J. L., "Proportional and Non-Proportional Biaxial Fatigue of Inconel 718," M.S. Thesis, Department of Mechanical and Industrial Engineering, University of Illinois at Urbana-Champaign, Urbana, IL, 1985.
6. Bannantine, J. A., and Socie, D. F., "Observations of Cracking Behavior in Tension and Torsion Low Cycle Fatigue," ASTM Symposium on Low Cycle Fatigue-Directions for the Future, STP 942, 1987.
7. Socie, D. F., Kurath, P., and Koch, J. L., "A Multiaxial LCF Parameter," presented at Second International Conference on Biaxial/Multiaxial Fatigue, 1985, Sheffield, England.
8. Kandil, F. A., Brown, M. W., and Miller, K. J., "Biaxial Low-Cycle Fatigue of 316 Stainless Steel at Elevated Temperatures," Vol. 280, The Metals Society, London, 1982, pp. 203-210.
9. Krempl, E., The Influence of State of Stress on Low-Cycle Fatigue of Structural Materials: A Literature Survey and Interpretive Report, ASTM STP 549, American Society for Testing and Materials, 1974, 46 pp.
10. Bunshah, R. F. (ed.), "Measurement of Mechanical Properties, Part 1," Techniques of Metals Research, Vol. 5, Interscience Publishers, 1971, pp. 126-197.
11. Garud, Y. S., "Multiaxial Fatigue: A Survey of the State of the Art," Journal of Testing and Evaluation, Vol. 9, No. 3, 1981, pp. 165-178.
12. Zamrik, S. Y., "Multiaxial Fatigue Low Cycle Fatigue Testing," Nonlinear Constitutive Relations for High Temperature Application-1984, NASA Conference Publication 2369, National Aeronautics and Space Administration, 1985, pp. 221-236.

13. Brown, M. W., and Miller, K. J., "A Theory for Fatigue Failure under Multiaxial Stress-Strain Conditions," Proceedings of the Institute of Mechanical Engineers, London, England, Vol. 187, No. 65, 1973, pp. 745-755.
14. McDiarmid, D. L., "Failure Criteria and Cumulative Damage in Fatigue under Multiaxial Stress Conditions," Ph.D. Thesis, The City University, London, England, 1972, 325 pp.
15. Blass, J. J., and Findley, W. N., "The Influence of the Intermediate Principal Stress on Fatigue under Triaxial Stresses," Material Research and Standards, Vol. 7, No. 6, 1967, pp. 254-261.
16. Bundy, R. W. and Marin, J., "Fatigue Strength of 14S-T4 Aluminum Alloy Subjected to Biaxial Stresses," Proceedings of ASTM, Vol. 54, 1954, pp. 755-768.
17. Pascoe, K. J., and de Villiers, J.W.R., "Low Cycle Fatigue of Steels under Biaxial Straining," Journal of Strain Analysis, Vol. 2, No. 2, 1967, pp. 117-126.
18. Havard, D. G., "Fatigue and Deformation of Normalized Mild Steel Subject to Cyclic Biaxial Loading," Ph.D. Thesis, Civil Engineering Department, University of Waterloo, Waterloo, Canada, 1970, 200 pp.
19. Havard, D. G., and Topper, T. H., "Biaxial Fatigue of 1018 Mild Steel at Low Endurance," Proceedings of the First International Conference on Pressure Vessel Technology, ASME, Part II, 1969, pp. 1267-1277.
20. Havard, D. G., Williams, D. P., and Topper, T. H., "Biaxial Fatigue of Mild Steel: Data Synthesis and Interpretation," Ontario Hydro Research Quarterly, Second Quarter, 1975, pp. 11-18.
21. Andrews, J.M.H., "Biaxial High Strain Fatigue of an Aluminum Alloy," Ph.D. Thesis, University of Bristol, Bristol, England, 1972, 130 pp.
22. Ellison, E. G., and Andrews, J.M.H., "Biaxial Cyclic High Strain Fatigue of Aluminum Alloy RR58," Journal of Strain Analysis, Vol. 8, No. 3, 1973, pp. 209-219.
23. Lohr, R. D., and Ellison, E. G., "Biaxial High Strain Fatigue Testing of 1Cr-Mo-V Steel," Fatigue of Engineering Materials and Structures, Vol. 3, 1980, pp. 19-37.
24. Lohr, R. D., and Ellison, E. G., "A Simple Theory for Low Cycle Multiaxial Fatigue," Fatigue of Engineering Materials and Structures, Vol. 3, 1980, 1-17.
25. Lefebvre, D., Chebl, C., and Khazzari, E., "Multiaxial High Strain Fatigue of A-516 Grade 70 Steel," Fatigue 84, Proceedings of the 2nd International Conference on Fatigue and Fatigue Thresholds, Vol. 3, 1984, pp. 1695-1704.

26. Charvat, I.M.H., and Garrett, G. G., "The Development of a Closed Loop Servo-Hydraulic Test System for Direct Stress Monotonic and Cyclic Crack Propagation Studies under Biaxial Loading," Journal of Testing and Evaluation, Vol. 8, No. 1, 1980, pp. 9-17.
27. Hoshide, T., Tanaka, K., and Yamada, A., "Stress-Ratio Effect of Fatigue Crack Propagation in a Biaxial Stress Field," Fatigue of Engineering Materials and Structures, Vol. 4, No. 4, 1981, pp. 355-366.
28. Brown, M. W., and Miller, K. J., "Mode I Fatigue Crack Growth under Biaxial Stress at Room and Elevated Temperature," Multiaxial Fatigue, ASTM STP 853, K. J. Miller and M. W. Brown, Eds., American Society for Testing and Materials, 1985, pp. 35-152.
29. Fatemi, A., and Socie, D. F., "A Critical Plane Approach to Multiaxial Fatigue Damage Including Out-of-Phase Loading," submitted to Journal of Fatigue and Fracture of Engineering Materials and Structures, 1986.
30. Halford, G. R., and Morrow, J., "Low Cycle Fatigue in Torsion," Proceedings of ASTM, Vol. 62, 1962, pp. 695-707.
31. Leese, G. E., and Morrow, J., "Low Cycle Fatigue Properties of a 1045 Steel in Torsion," Multiaxial Fatigue, ASTM STP 853, K. J. Miller and M. W. Brown, Eds., American Society for Testing and Materials, 1985, pp. 482-489.
32. Ugural, A. C., and Fenster, S. K., Advanced Strength and Applied Elasticity, New York: Elsevier, 1981.
33. Parray, J.S.C., "Fatigue of Thick Cylinders: Further Practical Information," Proceedings of the IME, Vol. 180, Part I, No. 16, pp. 387-416, 1965-66.
34. Chakrabarty, J., Theory of Plasticity, New York: McGraw-Hill Book Co., 1987.
35. Commer, J., unpublished data.
36. Socie, D. F., "Fatigue Damage Maps," Fatigue 87, Third International Conference on Fatigue and Fatigue Thresholds, 1987, Charlottesville, VA.

## APPENDIX A OVERVIEW OF TEST SYSTEM

The following is an overview of the test system hardware used in the research described in this thesis, including the load frame, pressure vessel, and specimen mandril.

Figure A1 shows a schematic drawing of the load frame. The test system was designed with a tubular specimen of specific dimensions in mind, allowing the load frame to have a fixed crosshead. This fixed crosshead design resulted in load frame rigidity sufficient to resist the pressure induced loading caused by the hydraulic fluid pressing against the push rod, as well as the axial and torsional reactions caused by loading the specimen. Rotary and axial actuators were mounted under the base plate; the rotary actuator was decoupled from the axial actuator with hydrostatic linear bearings.

Figure A2 shows a sectioned view of the pressure vessel and its contents. Access to the specimen was gained by raising the top half of the pressure vessel while the bottom half remained bolted to the base plate. Two hydraulic slave cylinders (not shown) were used to raise and lower the upper half of the pressure vessel. Instead of bolting the two halves of the pressure vessel together during testing, the design employed the differential area at the parting seal region between the upper and lower halves to create the required clamping force. As a result, the specimen could be accessed in a few minutes for observations during a test.

Within the pressure vessel, a pressure compensated load cell placed in the working fluid easily separated the pressure induced axial loads reacting against the actuator from axial loads placed on the specimen.

Internal pressure was supplied from the top of the load frame through the mandril. Figure A3 is a schematic drawing of the sectioned mandril and

specimen. The primary function of the mandril was to decouple internal pressure induced stresses from axial stresses by allowing the specimen to "float" on the mandril; resulting pressure induced axial loads were transmitted through the mandril and not the specimen. Specimens could be pulled off the end of the mandril with resistance only from the drag of the seals. This degree of freedom was used to decouple the axial loading from the internal pressure loading.

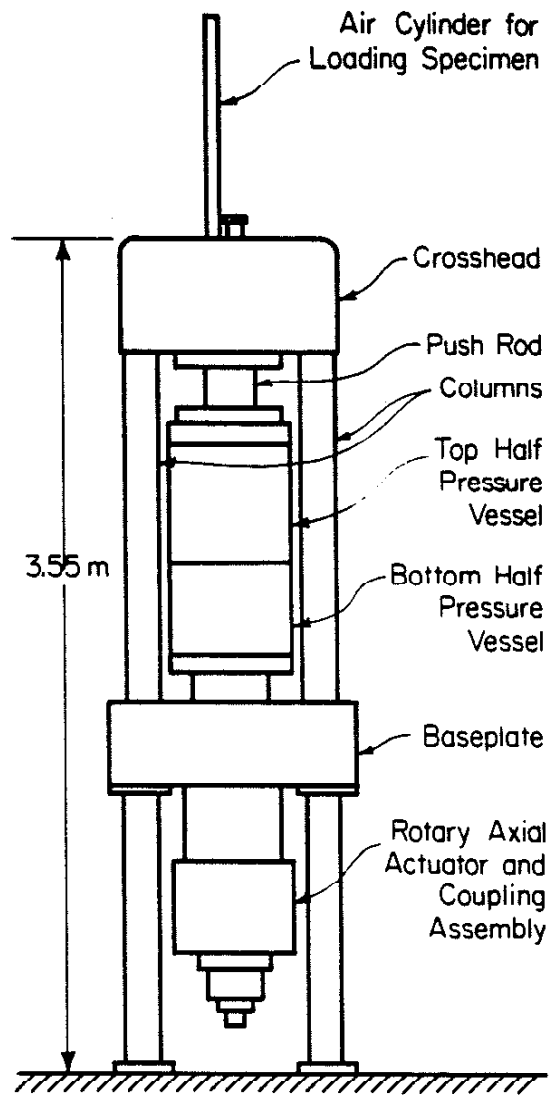


Figure A1. Schematic drawing of the load frame.

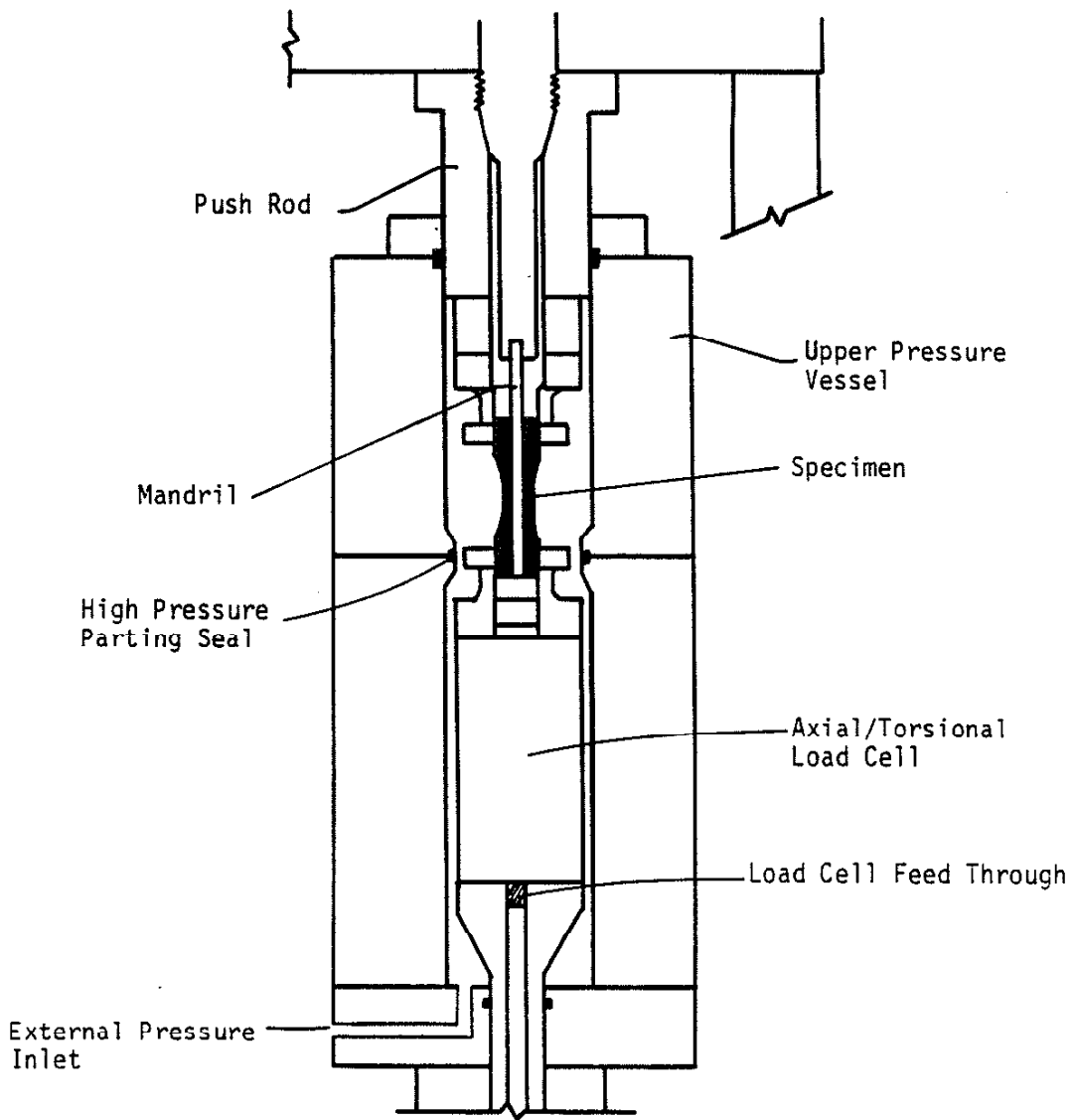


Figure A2. Sectioned view of the pressure vessel and its contents.

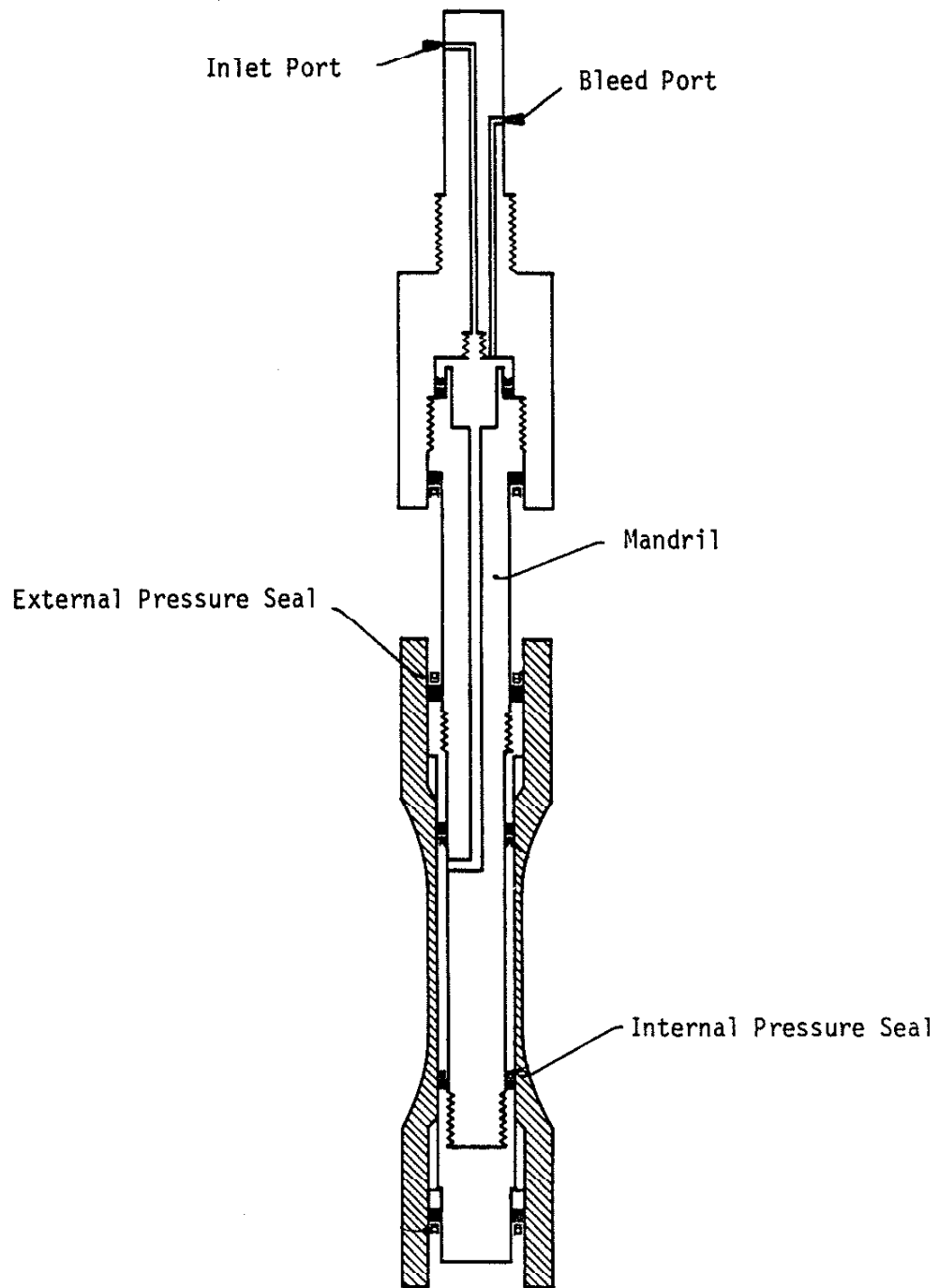


Figure A3. Schematic drawing of sectioned mandril and specimen.



## APPENDIX B TEST CONTROL CONDITIONS

Fatigue tests involving the use of internal and external pressure are complex and require extensive practical experience to surmount the difficulties attendant on any attempt to achieve a particular state of stress or strain. The following material is included in an attempt to share some of the benefits of this practical experience with the reader.

Test INDM01 was controlled from strain gages bonded to the center of the double reduced specimen for the first 200 cycles, then control was switched to load and pressure to prevent the failure of a strain gage from ruining the test. Figure B1 shows a schematic of the control system required to perform the strain control portion of this test. Axial strain control was straightforward and simply required the axial strain gage to replace the axial extensometer. Tangential strain control required that the strain gage replace the diametral extensometer and that the external pressure system be driven with the inverse of the internal pressure response. To start the test, both internal and external pressure were increased simultaneously until the appropriate hydrostatic pressure was reached. For an increase in tangential strain from this hydrostatic pressure level, the internal pressure would increase while the external pressure would decrease. This was accomplished by driving the external pressure system, in pressure control, with the inverse of the internal pressure response. This scheme was used for all strain control tests requiring external pressure.

INDM05 was an elastic test in which axial load and internal pressure were controlled. Internal and external pressure were set to an appropriate hydrostatic pressure, where internal pressure was subsequently cycled to achieve

the completely reversed loading. The control scheme is identical to Figure 5 except that external pressure was held constant.

INDM03 was an elastic test controlled as INDM05 was controlled, only at a lower hydrostatic pressure.

INDM07 was equal-biaxially strained to 0.0044 using internal pressure and axial loading, then unloaded and cycled elastically in load and pressure control while maintaining strain levels. In effect, this was a strain controlled test performed in load control.

INDM08 was an elastic load and pressure controlled test, as illustrated in Figure 5, except that in this test only internal pressure was used.

INDM06 used an identical control scheme as INDM08, as did IN01 and IN02.

The biaxial mean stress tests used only internal pressure and axial load or strain for control modes.

INA4, INA17, INA5, and INA13 were mixed mode tests with the same control scheme depicted in Figure 5; the axial systems in these tests, however, were in strain control mode.

INA12 and INA23 were controlled using the control scheme in Figure 5 without external pressure.

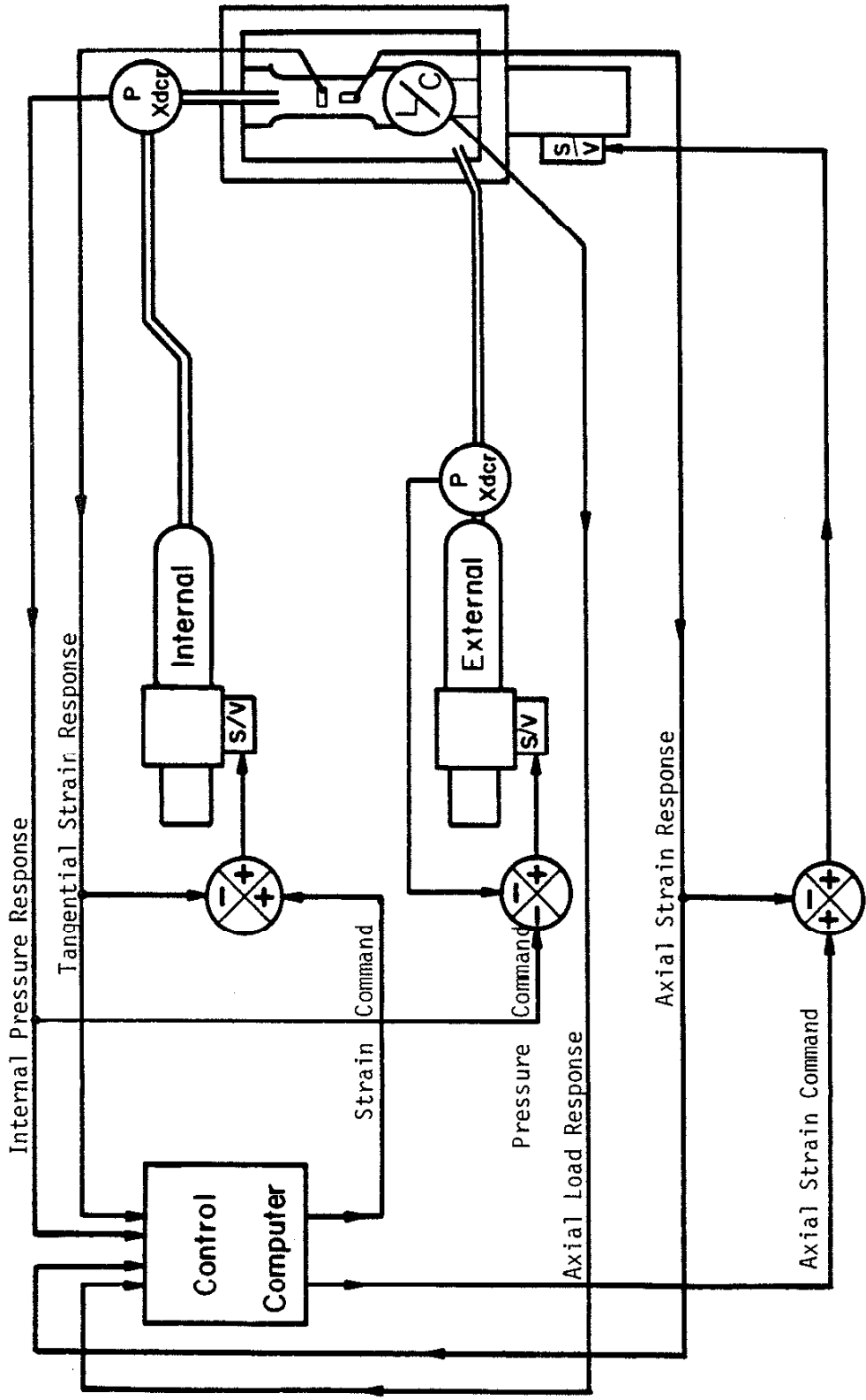


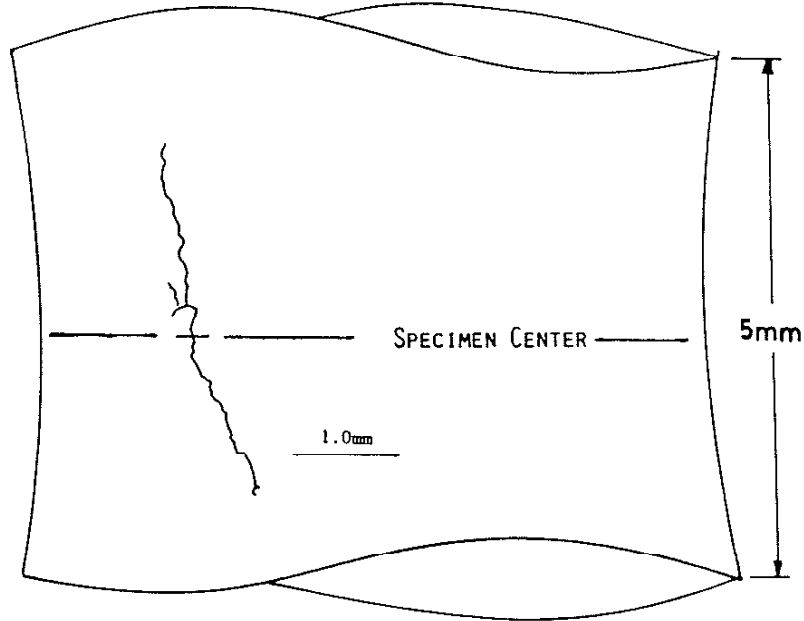
Figure B1. Schematic of control system for strain controlled tests.

## APPENDIX C SURFACE CRACK MEASUREMENTS

This appendix includes details on the location of surface cracks as well as their length for various cycles during the test. All failure cracks initiated in the thinnest region within the double reduced gage section of the specimen. Crack lengths were measured as the longest straight line segment between any two active crack tips. Specimen INDM01 failed before any crack growth data could be recorded.

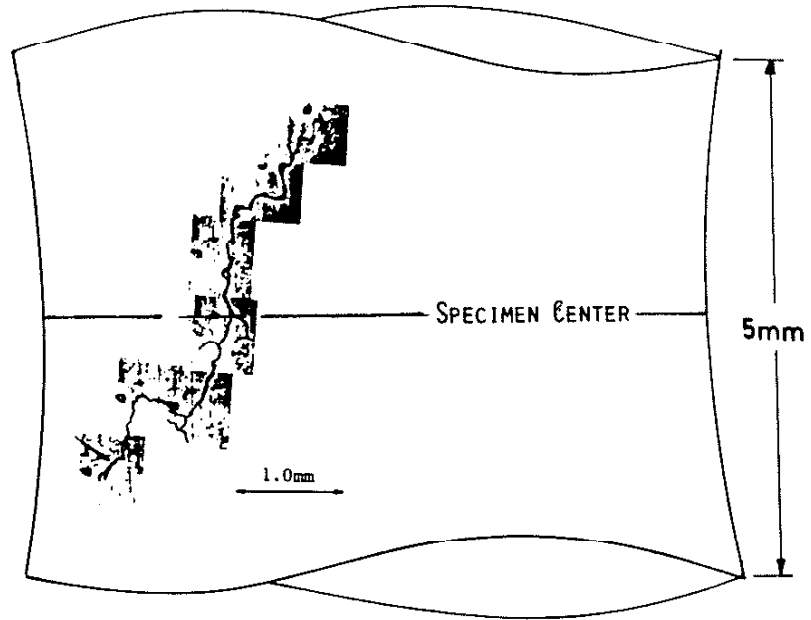
INDM03

(Non-failure crack, this was the first crack to initiate.)



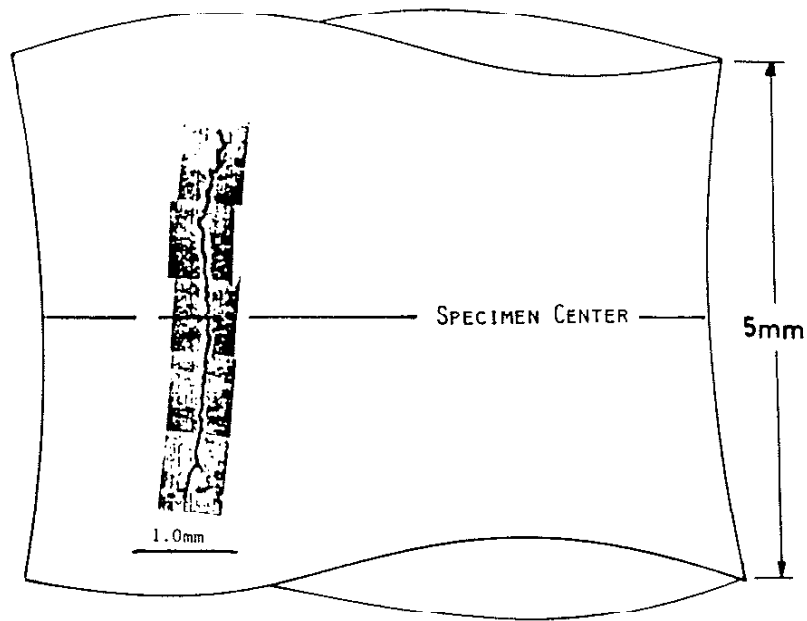
N(cycles)	Segment		
	(1) a(mm)	(2) a(mm)	(3) a(mm)
38000	0.06	N/A	N/A
48000	0.15	-	-
58000	0.24	-	-
63000	0.29	-	-
68000	0.35	-	-
72000	0.38	0.15	-
76000	0.41	0.15	-
80000	0.47	0.18	-
85000	0.52	0.18	-
90000	0.55	0.18	0.31
95000	0.57	0.18	0.32
Linking Occurred	-----		
100000		0.82	0.33
105000		N/A	0.41
Linking Occurred	-----		
110000		1.6	
120000		2.0	
125000		2.9	
126628		3.6	

INDM05



N(cycles)	a(mm)
20221	0.044
25000	0.155
31000	0.217
46000	0.670
51000	1.010
55414	1.370
58084	4.430

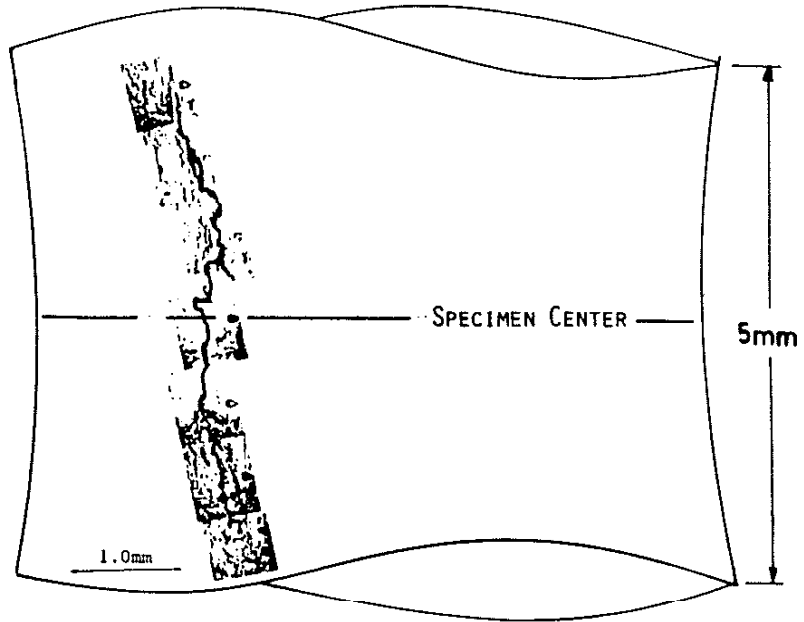
INDM06



N(cycles)	a(mm)
27916	0.031
40000	0.088
75000	0.155
100000	0.242
124000	0.514

Note: This is not the failure crack. The failure crack was not present on the outer surface at cycle number 124000.

INDM07

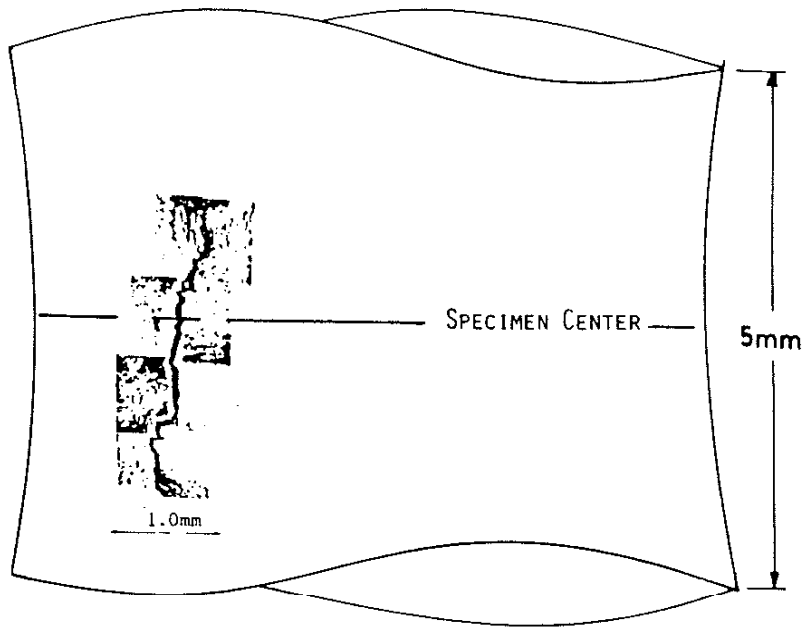


N(cycles)	a(mm)
6000	0.031
8000	0.162
10000	0.204
13000	0.279
15522	0.333
19000	0.915

Note: This is not the failure crack. The failure crack was not present on the outer surface at cycle number 19000.



INDM08



N(cycles)	a(mm)
2150	0.030
13346	0.403
20000	0.676

Note: This is not the failure crack. The failure crack was not present on the outer surface at cycle number 20000.

## VITA

Daniel Lowell Morrow was born on October 7, 1952 to JoDean and Sally Coonrod Morrow in Ft. Belvoir, Virginia. He spent his childhood in Urbana and Champaign, Illinois, and is currently a resident of Champaign. He attended Southern Illinois University at Carbondale and earned a B.S, M.S., and Ph.D. at the University of Illinois at Urbana-Champaign. As an undergraduate, he was named to the Deans List at SIU's College of Engineering and Technology and at the UIUC's College of Engineering. In 1982, he was the MTS Graduate Fellow in the UIUC Department of Mechanical and Industrial Engineering and has held various appointments within the Department. In 1984, he was invited to Guest, Keen, and Nettleton, Wolverhampton, England in the capacity of visiting research scientist. He is a member of the Society of Automotive Engineers Fatigue Design and Evaluation Committee and has engaged in industrial consulting throughout his academic career. In 1975, he married Kathryn Roberts; he has two children, Carl Daniel and Anne Eleanor.